LOCAL STRUCTURE AND DYNAMICS OF EXCITON-COUPLED CYANINE DIMERS LABELED IN DNA

by

LONI MICHELLE KRINGLE

A DISSERTATION

Presented to the Department of Chemistry and Biochemistry
and the Graduate School of the University of Oregon
in partial fulfillment of the requirements
for the degree of
Doctor of Philosophy

June 2018

DISSERTATION APPROVAL PAGE

Student: Loni Michelle Kringle

Title: Local Structure and Dynamics of Exciton-Coupled Cyanine Dimers Labeled in DNA

This dissertation has been accepted and approved in partial fulfillment of the requirements for the Doctor of Philosophy degree in the Department of Chemistry and Biochemistry by:

Jeffrey Cina	Chairperson
Andrew H. Marcus	Advisor
Peter von Hippel	Core Member
Michael Raymer	Institutional Representative

and

Sara D. Hodges	Interim Vice Provost and Dean of the Graduate School

Original approval signatures are on file with the University of Oregon Graduate School.

Degree awarded June 2018

DISSERTATION ABSTRACT

Loni Michelle Kringle

Doctor of Philosophy

Department of Chemistry and Biochemistry

June 2018

Title: Local Structure and Dynamics of Exciton-Coupled Cyanine Dimers Labeled in DNA

Understanding the properties of electronically interacting molecular chromophores, which involve internally coupled electronic-vibrational motions, is important to the spectroscopy of many biological systems. Here we apply linear absorption, circular dichroism, and two-dimensional fluorescence spectroscopy to study the local structure and excited state dynamics of excitonically coupled cyanine dimers that are rigidly positioned within the sugar-phosphate backbones of the DNA. Dimer probes were positioned within the double-stranded DNA duplex and at the single-strand/double-stranded DNA junction to examine the positional dependence of the structural variation and fluctuations. We interpret spectroscopic measurements in terms of the Holstein vibronic dimer model, from which we obtain information about the local conformation of the dimer probe locally within their respective DNA environments. We show that the exciton-coupling strength of the dimer-DNA construct can be systematically varied with temperature below the double-stranded – single-strand DNA denaturation transition. Using time-resolve 2DFS measurements we observed long lived vibronic coherences in the system. The properties of the cyanine DNA construct we determine suggest that it may be employed as a useful model system to test fundamental concepts of protein DNA

interactions and the role of electronic-vibrational coherence in electronic energy migration within exciton-coupled biomolecular arrays.

This dissertation contains previously published and unpublished co-authored material.

CURRICULUM VITAE

NAME OF AUTHOR: Loni Michelle Kringle

GRADUATE AND UNDERGRADUATE SCHOOLS ATTENDED:

University of Oregon, Eugene
Wartburg College, Waverly, Iowa

DEGREES AWARDED:

Doctor of Philosophy, Chemistry, 2018, University of Oregon
Bachelor of Arts, Chemistry, 2012, Wartburg College
Bachelor of Arts, Physics, 2012, Wartburg College

AREAS OF SPECIAL INTEREST:

Coherent Multidimensional Optical Spectroscopy
Local conformation and Excited State Dynamics of Cyanine Dyes
Modeling of Electronic-Vibrational (Vibronic) Coupling

PROFESSIONAL EXPERIENCE:

Graduate Research Assistant, Department of Chemistry and Biochemistry, University of Oregon, Eugene, 2016-2018

Graduate Teaching Assistant, Department of Chemistry and Biochemistry, University of Oregon, Eugene, 2012-2016

Chemistry Teaching Lab Assistant, Department of Chemistry, Biochemistry, and Engineering, Wartburg College, 2010-2012

Physics Teaching Lab Assistant, Department of Math, Computer Science, and Physics, Wartburg College, 2010-2012

Undergraduate Research Assistant, Department of Chemistry, Biochemistry, and Engineering, Wartburg College, 2010

GRANTS, AWARDS, AND HONORS:

Award of Excellence – Chemistry, American Association for the Advancement of Sciences Pacific Division Annual Meeting, 2017

Rosaria Haugland Chemistry Graduate Research Fellowship, University of Oregon, Eugene, 2015

Honorable Mention Graduate Research Fellowship, National Science Foundation, 2014

Outstanding Senior, Physics Departmental Award, Wartburg College, Waverly, 2012

R. J. McElroy Student Research Fellowship, Wartburg College, Waverly, 2011

Professor A. W. Swenson Chemistry Scholarship, Wartburg College, Waverly, 2010

PUBLICATIONS:

L. Kringle, N. P. K. Sawaya, J. Widom, C. Adams, M. G. Raymer, A. Aspuru-Guzik, and A. H. Marcus, "Temperature-dependent conformations of exciton-coupled Cy3 dimers in double-stranded DNA," *J. Chem. Phys.* **148**, 085101 (2018).

K. J. Karki, L. Kringle, A. H. Marcus, and T. Pullerits, "Phase-synchronous detection of coherent and incoherent nonlinear signals," *J. Optics* **18**, 015504 (2015).

P. G. Blower, E. Shamay, L. Kringle, S. T. Ota, G. L. Richmond, "Surface behavior of malonic acid adsorption at the air/water interface," *J. Phys. Chem. A* **117**, 2529 (2013).

ACKNOWLEDGMENTS

I have been fortunate to have been supported by so many wonderful people during this work. I am grateful for everyone who has helped me, in big and small ways.

I would first like want to thank my advisor, Professor Andy H. Marcus, and my committee members, Professors Pete H. von Hippel, Jeff Cina, Mike Raymer, and until his retirement, John Hardwick. Your wisdom and guidance have been instrumental to my success. I would like to thank Dr. Larry Scatena and Clifford Dax for their assistance in fixing the laser system and electronics, and keeping my experiments running. An enormous thank you goes to my lab mates, past and present, especially Dr. Julia Widom, who taught me how to run the laser system, and Huiying Ji, whose positivity keeps our office balanced.

I would like to thank my incredible mentors Professors Christine DeVries and Cathy Wong. I never would have gotten to this point without your encouragement. You both have helped me through difficult times and provided perspective from the other side without judgement. I hope to be half as amazing as you someday.

I want to thank the members and executive committees of the University of Oregon Women in Graduate Sciences (WGS) and the University of Oregon Student Chapter of the Optical Society (OSA), as well as the staff at the Eugene Science Center, Randy Sullivan, and the other outreach programs I have been a part of. You have provided me with a community of science educators and communicators and have given me the opportunity to share my science with the public and engage the next generation of scientists.

I am grateful to all my friends, whose support has kept me moving forward. We have celebrated our accomplishments and most holidays together, creating a little Eugene family. To my hiking buddies, thank you for adventuring with me to the tops of mountains, the bottom of the Grand Canyon, along the PCT, and into the Oregon wilderness to watch the moon eclipse the sun. And to my soccer team mates, Specific Heat and Team Hot Rod, you provided an outlet to the stress of graduate school, we won some and lost more but we were in it together.

I want to thank my family for supporting me, even when you don't understand what I am saying. To my grandparents, Carl and Phyllis, thank you for taking me on my first trip to the Science Museum of Minnesota. To Tanya, you are the best sister and I am eternally grateful to you. And to my parents, Dale and Donna, you have encouraged me to succeed and follow my dreams wherever they lead.

Finally, this work would not have been possible without the financial support of the Rosaria Haugland Graduate Research Fellowship, the John Templeton Foundation, the National Science Foundation, and the National Institute of Health.

To My Family

TABLE OF CONTENTS

Chapter Page

Chapter Page

LIST OF FIGURES

Figure Page

Figure Page

Figure Page

LIST OF TABLES

Table Page

Table Page

CHAPTER I

INTRODUCTION

Many centrally important biological processes require local regions of DNA to spontaneously open, allowing proteins to access the single-stranded nucleotide base sequences or secondary structure motifs. This DNA 'breathing' likely results in a broad distribution of functionally relevant, positionally dependent conformations.[1–4] Therefore, characterization of the nature and extent of conformational disorder within DNA is central to the molecular mechanisms of binding and the function of protein-DNA complexes involved in processes of replication, repair, and transcription.

The study of nucleic acids and amino acids using spectroscopic techniques is complicated by several factors, most central here is that most biological molecules absorb UV light and emit little or no fluorescence. This results in the overlapping and merging of spectral features and an inability to sensitively examine regions of interest. To overcome this, fluorescent probes are used to site specifically label the biological molecules and allow for examination of local structure and dynamics at key positions.[1–3,5,6]

This work focuses on the local structure of the cyanine dyes, Cy3 and Cy5, when incorporated into the sugar-phosphate backbone through phosphoramidite insertion methods as shown in Figure 1.1.[7,8] These fluorescent probes absorb and emit visible light and are commonly used in molecular biological studies.[4,7–13] When 'internally' labeled into the DNA, they do not appreciably perturb the native structure as measured through absorption and circular dichroism studies[4,12,13] and do not 'interfere' with the protein

interaction at the replication fork.[12] Additionally, on the single molecule level, these dyes have been able to discern the structural fluctuations of DNA.[4]

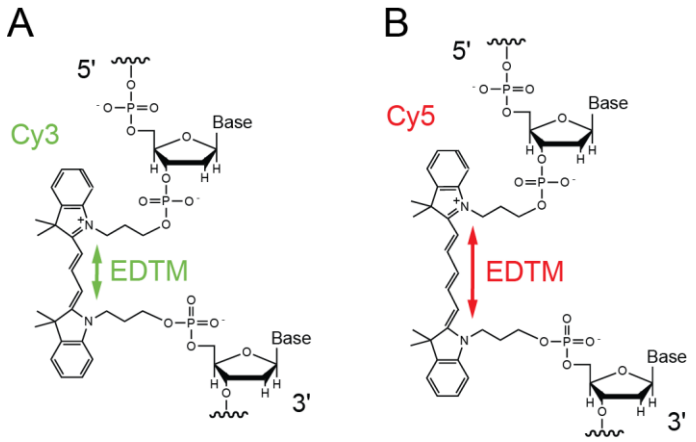

Figure 1.1: The structural formula of the internally labeled **(A)** Cy3 and **(B)** Cy5 chromophores are shown with their insertion linkages to the 3' and 5' segments of the sugar-phosphate backbone of ssDNA. A green (red) double-headed arrow indicates the orientation of the electric dipole transition moment (EDTM), which lies parallel to the plane of the trimethine bridge.

In this work, I used absorption, circular dichroism, and two-dimensional fluorescence spectroscopy to examine the local conformation adopted by a cyanine dimer labeled within the double-stranded duplex or at the double-strand – single-strand DNA fork junction. Three conformational parameters are used to describe the local structure including the inter-chromophore twist angle ϕ_{AB}, the inter-chromophore tilt angle δ_{AB}, and the inter-chromophore separation R_{AB}, shown in Figure 1.2. When the ensemble average conformation is combined with the spectral inhomogeneity, a picture of the structural variation at the fork junction and the positional dependent 'breathing' emerges.

To account for the electronic vibrational coupling of the chromophore and the excitonic coupling of the system the simple Holstein model was used to mathematically represent the molecular system. This simple model used only a single effective vibrational

mode, however it was able to accurately represent the experimental spectra at conditions below the denaturation temperature of the DNA.

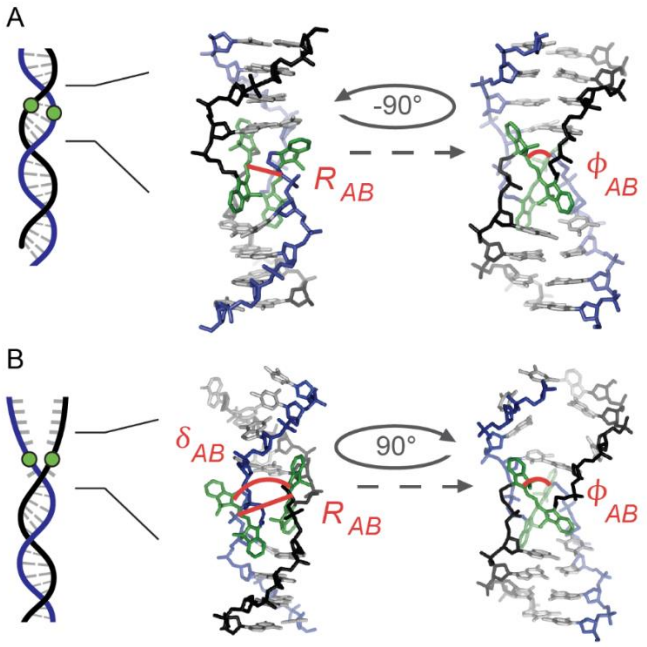

Figure 1.2: Model structure of the internally labeled $(Cy3)_2$ dimer in DNA. **(A)** A dsDNA segment and **(B)** ssDNA-dsDNA junction formed from two complementary DNA strands, which each contains an internally labeled Cy3 chromophore, serves as a scaffold to hold the $(Cy3)_2$ dimer in place. The sugar-phosphate backbones of the conjugate strands are shown in black and blue, the bases in gray, and the Cy3 chromophores in green. Additional space-filling renderings of the structure are presented in Figure A1. The structural parameters that define the local conformation of the $(Cy3)_2$ dimer are the inter-chromophore separation vector $\boldsymbol{R}_{AB}$ and the twist angle ϕ_{AB}.

The temperature sensitivity of the Cy3 dimer structure when labeled DNA, combined with the insensitivity of the intra-molecular parameters to temperature indicate that the system could serve as an experimental model system to explore the role of electronic-vibrational (vibronic) coherence on the electronic energy transport. Signatures of coherence have been observed in photosynthetic antenna complexes and the origins of these oscillations has been a topic of much debate.[14–24] The 'tunability' of the cyanine

dimer – DNA system allows for the separation of the vibronic and excitonic components to test the mechanisms put forth.

Dissertation Outline and Acknowledgements of the Contributions by Others

Chapter II presents the theory and mathematical model used to calculate the spectra of the exciton-coupled cyanine dimers, and contains published material co-authored with N. P. D. Sawaya, J. Widom, C. Adams, M. G. Raymer, A. Aspuru-Guzik, and A. H. Marcus.[25] Additionally, this chapter contains unpublished material co-authored with A. H. Marcus. The well-known Holstein Hamiltonian was used to model the dimer system, and determine the structural parameters (separation distance, twist angle, and tilt angle) leading to the observed absorption, circular dichroism, and two-dimensional fluorescence spectra. The derivation of the Holstein Hamiltonian and application to the cyanine dye system was done by M. G. Raymer and A. H. Marcus. N. P. D. Sawaya wrote the initial computational code used to model the absorption and CD from the Holstein model. The remaining co-authors provided editorial assistance.

Chapter III presents the experimental considerations used throughout the dissertation, and contains unpublished co-authored material with L. Scatena and A. Tamimi and published material with N. P. D. Sawaya, J. Widom, C. Adams, M. G. Raymer, A. Aspuru-Guzik, and A. H. Marcus.[25] The sequences and sample considerations of the cyanine dye-DNA constructs and the spectroscopic methods used to examine these probes are described, and the mathematical optimization procedure is outlined. In this work, L. Scatena guided the construction of the noncollinear optical parametric amplifier and A. Tamimi built the folded double pass prism compressor system. A. H. Marcus collaborated

in conceiving and planning the experimental techniques used, the remaining co-authors provided editorial assistance.

Chapter IV presents the studies of the conformations adopted by cyanine-labeled DNA within the duplex region of the DNA construct. This chapter contains published co-authored work with N. P. D. Sawaya, J. Widom, C. Adams, M. G. Raymer, A. Aspuru-Guzik, and A. H. Marcus.[25] This chapter also contains unpublished co-authored work with J. Widom, C. Adams, and A. H. Marcus. The double linkage insertion of the cyanine dimers within the duplex region of DNA restricts the conformational accessibility of the dyes and the degrees of freedom can be reduced, where the tilt angle is no longer considered. Under this approximation the relative structural configuration of the dimer can be determined from absorption and circular dichroism. J. Widom and C. Adams collected the absorption and CD spectra. N. P. D. developed the model to describe the molecular system. A. H. Marcus collaborated in conceiving and planning the experiments, and the remaining co-authors provided editorial assistance.

Chapter V presents studies of the conformations adopted by cyanine dyes when labeled at or near fork junctions of the DNA construct. This chapter contains unpublished co-authored work with D. Jose, J. Widom, D. Heussman, A. Tamimi, C. Adams, P. H. von Hippel, and A. H. Marcus. The increased structural flexibility and fluctuations that occur at fork junctions of DNA was considered by including the tilt angle parameter. A number of degenerate conformations resulted from the optimizations to the linear spectra and the nonlinear spectra was used to reduce the structural ambiguity. D. Jose, J. Widom, and C. Adams collected the absorption and circular dichroism spectra, and D. Heussman and A. Tamimi collected the two-dimensional fluorescence spectra of the fork junction constructs.

A. H. Marcus and P. H. von Hippel collaborated in conceiving and planning the experiments.

Chapter VI presents the examination of the ultrafast dynamics of the duplex labeled cyanine-dye system and contains unpublished co-authored work with A. H. Marcus. The population time dependent 2DFS measurements exhibit oscillatory behavior of the spectral features indicative of coherences within the system. The characterization and initial explanation for the observed behavior is described within the chapter. A. H. Marcus collaborated in conceiving and planning the experiments.

CHAPTER II

THEORETICAL AND MATHEMATICAL MODEL CONSIDERATIONS

Overview

This chapter presents the theory and mathematical models used to determine the conformations of excitonically coupled cyanine dyes when labeled within DNA. This chapter will also describe the models used to calculate the absorption, circular dichroism, and two-dimensional fluorescence spectra. This section contains material that has been published as L. Kringle, N. P. D. Sawaya, J. Widom, C. Adams, M. G. Raymer, A. Aspuru-Guzik, and A. H. Marcus, "Temperature-dependent conformations of exciton-coupled Cy3 dimers in double-stranded DNA," *J. Chem. Phys.* **148**, 085101 (2018). In the excerpt used here A. H. Marcus, M. G. Raymer, and I formed the description of the molecular Hamiltonian with the assistance and insight of N. P. D. Sawaya and A. Asupru-Guzik. The additional co-authors provided editorial assistance.

Introduction

The determination of the local conformations of molecules requires the selection of an appropriate experimental technique and mathematical model to interpret the experimental data. In this work, we used the complementary techniques of absorption, circular dichroism (CD), and two-dimensional fluorescence spectroscopy (2DFS) to examine the local conformations of cyanine dyes labeled within DNA. Absorption and CD are commonly used techniques that have been used extensively in the study of cyanine dyes.[1–7] Absorption examines the ground to excited state transitions of the system, while

CD is the differential absorption of right and left handed circularly polarized light, with the latter providing insight into the chirality of the system. 2DFS is a nonlinear spectroscopic technique, in which multiple laser pulses interact with the sample and the ensuing correlated interactions result in the separation of spectral features that would otherwise be merged in linear spectroscopic techniques (such as absorption and CD). The examination of the separate and coupled transitions provide insight into the conformation of the chromophore, analogous to 2D nuclear magnetic resonance (NMR) spectroscopy.

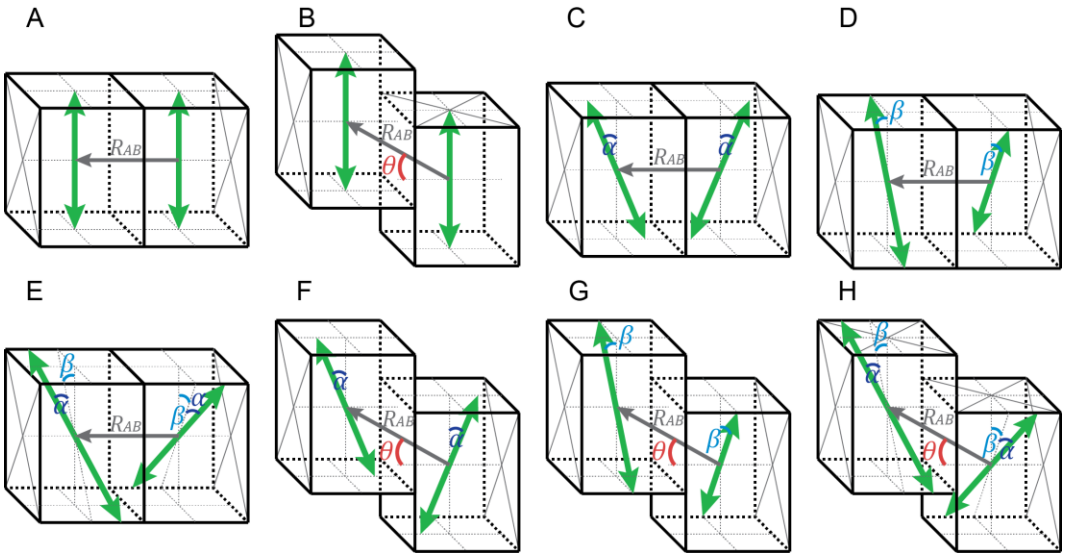

Figure 2.1: Illustration of possible dimer conformations. **(A)** Parallel transition dipoles (H-type dimer). **(B)** Co-planar inclined transition dimers with slip angle θ, where $\theta = 0°$ corresponds to (A) and $\theta = 90°$ is the in-line transition dipoles (J-type dimer). **(C)** Oblique transition dipoles with tilt angle $\delta = 2\alpha$. **(D)** Non-planar transition dipoles with twist angle $\phi = 2\beta$ (X-type dimer). Transition dipole conformations with a combination of **(E)** twist and tilt, **(F)** tilt and slip, **(G)** twist and twist, **(H)** twist, tilt and slip.

For the cyanine dye systems studied here, the intermediate-to-strong excitonic coupling of the dimer results in spectral shifts in the absorption spectrum of the dimer relative to that of the monomer.[8–11] Previous studies have used the spectral shifts to describe the orientation of the transition dipoles to a first approximation, where a red shift indicates an end-to-end configuration (J-type) or a blue shift indicates a face-to-face configuration

(H-type).[1–5,9,12] Additional configurations have been described by Kasha including oblique transition dipoles, co-planar inclined transition dipoles, and non-planar transition dipoles.[9] The combination of these possible geometries, such as those represented in Figure 2.1, make conformational discernment based purely on the direction of the spectral shifts ambiguous at best.

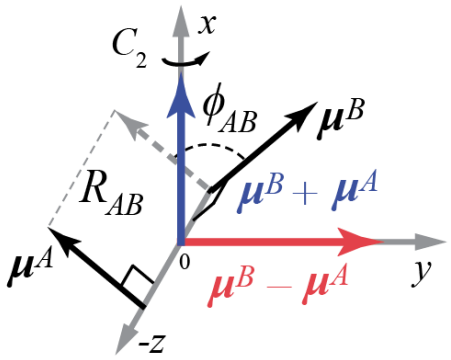

Figure 2.2: Cartesian coordinate system for the AB dimer. Monomer EDTMs, $\boldsymbol{\mu}^A$ and $\boldsymbol{\mu}^B$, are separated by the distance R_{AB}, twist angle ϕ_{AB}. The symmetric exciton $\boldsymbol{\mu}^A + \boldsymbol{\mu}^B$ (shown in blue) and the anti-symmetric exciton $\boldsymbol{\mu}^A - \boldsymbol{\mu}^B$ (shown in red) are each oriented parallel to the x- and y-axis, respectively. The x-axis is an axis of C_2 symmetry, as indicated. (the y and z axes are similarly C_2 symmetry elements.) Note that the point dipole-dipole coupling strength $J \propto \cos\phi_{AB}$ [see Eq. 2.6 below] undergoes a sign inversion at ϕ_{AB} = 90°.

We implemented the well-known Holstein Hamiltonian, which has been previously applied to model the electronic-vibrational (vibronic) character of an electronically interacting cyanine dimer.[13,14] We refer to the monomer sites as *A* and *B*, and specify the conformation by the inter-chromophore separation R_{AB}, twist angle ϕ_{AB}, tilt angle δ_{AB}, and slip angle θ_{AB}. In the following discussion, we refer to the coordinate system shown in Figure 2.2, this coordinate system is drawn with $\delta_{AB} = 0$ and $\theta_{AB} = 0$, such as the case when considering constructs in which the cyanine dyes are positioned deep within the duplex region of the dsDNA. Because each cyanine chromophore is rigidly attached at two

insertion site positions within the DNA single strands, the conformational space available to the cyanine dimer of the fully annealed DNA duplex is restricted. Simple van der Waals models suggested that the $(Cy3)_2$ dimer adopts a chiral conformation with approximately D_2 symmetry (see Figure A.1 of Appendix A).

Monomer Hamiltonian and Absorption Spectrum

We consider the EDTM (electric dipole transition moment) of each cyanine chromophore to be aligned parallel to the long axis of its trimethine chain (see Figure 1.1 in Chapter I).[15,16] The monomer EDTM is defined as the matrix element $\boldsymbol{\mu}_{eg}^{M} = \langle e|\hat{\boldsymbol{\mu}}^{M}|g\rangle_M$, where the operator $\hat{\boldsymbol{\mu}}^{M} = |g\rangle_M \mu_{ge}\langle e| + |e\rangle_M \mu_{eg}\langle g|$ couples the ground electronic state $|g\rangle_M$ to the excited electronic state $|e\rangle_M$ with transition energy $\varepsilon_M = \varepsilon_{eg}$. Each monomer M $(= A, B)$ has its two-level electronic transition coupled to a single harmonic mode with frequency ω_0 and generalized coordinate q_M. The identity operator for a monomer is given by the tensor product of electronic and vibrational state contributions: $\hat{I}_M = \hat{I}_M^{elec} \otimes \hat{I}_M^{vib}$, where $\hat{I}_M^{elec} = |g\rangle_M\langle g| + |e\rangle_M\langle e|$, $\hat{I}_M^{vib} = \sum_{n_g} |n_g\rangle_M\langle n_g|$, and where n_g is the population number of vibrational excitations (phonons) in the ground electronic state. The identity operator for the composite *AB* system is thus $\hat{I}_A \otimes \hat{I}_B$. In our numerical calculations described in Chapter III we obtained convergent results using a maximum of six vibrational excitations per monomer, consistent with the findings of others.[14,17]

In the composite space of the *AB* dimer, the Hamiltonian for each monomer is given by[18]

$$\hat{H}_M = \left\{\frac{1}{2}[\hat{p}_M^2/m + m\omega_0^2\hat{q}_M^2]|g\rangle_M\langle g| + \left[\varepsilon_{eg} + \frac{1}{2}(\hat{p}_M^2/m + m\omega_0^2(\hat{q}_M - d)^2)\right]|e\rangle_M\langle e|\right\} \otimes \hat{I}_{M'\neq M} \tag{2.1}$$

where $\hat{q}_M$ and $\hat{p}_M$ are coordinate and momentum operators, respectively, for the monomer's internal vibration and m is its reduced mass. Here we have taken the energy of the electronic ground state to be zero, and d is the Franck-Condon displacement projected onto the vibrational coordinate $\hat{q}_M$ (see Figure 2.3 A).

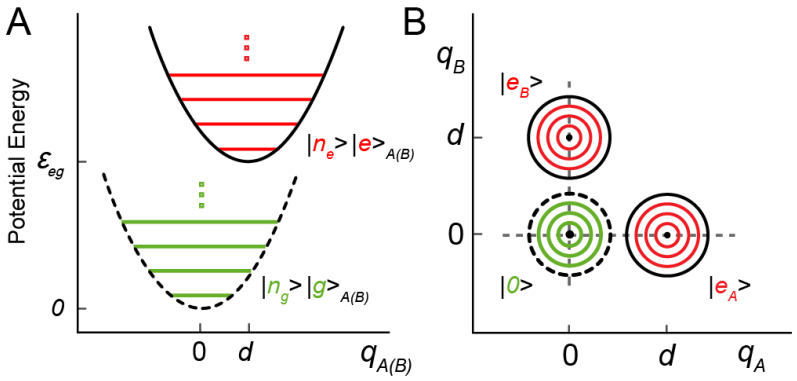

Figure 2.3: (A) Electronic-vibrational (vibronic) potential energy diagram for the monomer ground and excited electronic state levels, which are coupled to a single harmonic vibrational mode. **(B)** Contour diagram for the vibronic potential energy of the AB dimer in the three electronic states considered in the model.

The intensities of the absorptive transitions are determined by the square matrix elements $\left|\langle e|\langle n_e|\hat{\boldsymbol{\mu}}^M|g\rangle|n_g = 0\rangle_{A(B)}\right|^2 = \left|\boldsymbol{\mu}_{eg}^M\right|^2|\langle n_e|0\rangle|^2$, where we have taken the initial state of the molecule to be both electronically and vibrationally unexcited. We use the Condon approximation, which assumes that the EDTM is unaffected by the vibrational mode. It follows that the monomer absorption spectrum $\sigma_{H-abs}^M(\varepsilon)$ is the sum of homogeneous lineshapes associated with the individual vibronic transitions,[19] given by

$$\sigma_{H-abs}^M(\varepsilon) = \left|\boldsymbol{\mu}_{eg}^M\right|^2 \sum_{\boldsymbol{n_e}}^{\infty} |\langle n_e|0\rangle|^2 \, L_H\left(\varepsilon - \varepsilon_{eg} - n_e\hbar\omega_0\right) \tag{2.2}$$

In Eq. (2.2), we take the homogeneous lineshapes to be Lorentzian $L_H(\varepsilon) = \frac{1}{2}\Gamma_H \Big/ \left[\varepsilon^2 + \left(\frac{1}{2}\Gamma_H\right)^2\right]$ with full-width-at-half-maximum (FWHM) equal to Γ_H. The Franck-Condon overlap factors have the form $|\langle n_e|0\rangle|^2 = e^{-\lambda^2}\lambda^{2n_e}/n_e!$, where $\lambda^2 = d^2\omega_0/2\hbar$ is the number of vibrational quanta absorbed by the system upon electronic excitation. λ^2 is called the Huang-Rhys parameter, and in the context of the Holstein model, it is a direct measure of the electronic-vibrational coupling strength.[20]

Although each monomer is chemically identical, our model includes the presence of static inhomogeneity of the transition energy ε_{eg} due to variation of the local environment.[19,21,22] We thus assign the probability that a given monomer has transition energy ε_{eg} according to the Gaussian distribution $G_{I,mon}(\varepsilon_{eg}) = exp\left[-\left(\varepsilon_{eg} - \overline{\varepsilon}_{eg}\right)^2/2{\sigma_{I,mon}}^2\right]$, which is centered at the average transition energy $\overline{\varepsilon}_{eg}$. We account for the presence of both homogeneous and inhomogeneous broadening contributions to the total line shape by using the Voigt convolution integral[22]

$$\sigma_{abs}^{M}(\varepsilon) = \int_{-\infty}^{\infty} \sigma_{H-abs}^{M}(\varepsilon - \varepsilon')\, G_{I,mon}(\varepsilon') d\varepsilon' \tag{2.3}$$

Dimer Hamiltonian

In the collective electronic-vibrational (vibronic) basis of the *AB* dimer, we define the ground electronic state $|0\rangle = u_{n_g}^{A}(q_A)\,|g\rangle_A \otimes u_{n_g}^{B}(q_B)\,|g\rangle_B = u_{n_g n_g}(q_A, q_B)|gg\rangle$. Here we use the streamlined notation for the electronic states $|gg\rangle = |g\rangle_A|g\rangle_B$, and for the vibrational states $u_{n_g n_g}(q_A, q_B) = u_{n_g}^{A}(q_A) \otimes u_{n_g}^{B}(q_B)$. The latter emphasizes the nuclear coordinate dependence of the vibrational wave function corresponding to the product state

$|n_g n_g\rangle = |n_g\rangle_A \otimes |n_g\rangle_B$. In the absence of a resonant electronic interaction, the singly-electronically-excited states are given by $|e_A\rangle = u_{n_e n_g}(q_A, q_B)|eg\rangle$ in which monomer *A* is electronically excited and monomer *B* is in the ground state, and $|e_B\rangle = u_{n_g n_e}(q_A, q_B)|ge\rangle$ in which the *A* and *B* indices are interchanged. The model potential energy surfaces corresponding to the ground and singly-electronic-excited vibronic states are illustrated in Figure 2.3 B.

When electronic interactions between monomers are included, the Hamiltonian of the *AB* dimer is

$$\hat{H}_{dim} = \hat{H}_A \hat{I}_B + \hat{H}_B \hat{I}_A + J\{|eg\rangle\langle ge| + |ge\rangle\langle eg|\}\, \hat{I}_A^{vib} \otimes \hat{I}_B^{vib} \tag{2.4}$$

where the expressions for the monomer Hamiltonian $\hat{H}_M$ are given by Eq. (2.1). In Eq. (2.4), the last term describes the resonant coupling between the electronic coordinates of the two monomers. Neglecting orbital overlap, the value of *J* is determined by the Coulomb interaction between the transition charge densities

$$J = \frac{1}{4\pi\epsilon\epsilon_0} \int_{-\infty}^{\infty} d\boldsymbol{r}_A \int_{-\infty}^{\infty} d\boldsymbol{r}_B \frac{\rho_A^{ge}(\boldsymbol{r}_A)\rho_B^{eg}(\boldsymbol{r}_B)}{|\boldsymbol{r}_A - \boldsymbol{r}_B|} \tag{2.5}$$

where we have defined the matrix elements $\rho_A^{ge}(\boldsymbol{r}_A) = \langle g|_A \rho(\hat{\boldsymbol{r}}_A)|e\rangle_A$ and $\rho_B^{eg}(\boldsymbol{r}_B) = \langle e|_B \rho(\hat{\boldsymbol{r}}_B)|g\rangle_B$.

In the current work, we approximate the resonant electronic coupling using the point dipole expression

$$J = \frac{\left|\mu_{eg}^0\right|^2}{4\pi\epsilon\epsilon_0}\left[\frac{\left(\boldsymbol{d}_{eg}^A \cdot \boldsymbol{d}_{ge}^B\right)}{|\boldsymbol{R}_{AB}|^3} - 3\frac{\left(\boldsymbol{d}_{eg}^A \cdot \boldsymbol{R}_{AB}\right)\left(\boldsymbol{R}_{AB} \cdot \boldsymbol{d}_{ge}^B\right)}{|\boldsymbol{R}_{AB}|^5}\right] \tag{2.6}$$

Here, we have defined $\left|\mu_{eg}^{0}\right|^2$ as the square magnitude of the monomer EDTM, and $\boldsymbol{d}_{eg}^{M}$ $[M = A, B]$ are the unit vectors that specify each monomer direction. The point dipole approximation is justified when the inter-monomer distance is greater than two characteristic length scales: (*i*) the molecular size, and (*ii*) the transition dipole radius $\left|\mu_{eg}^{0}\right|/e$, where the fundamental charge unit e = 1.60 × 10^{-19} C.[20] Our estimate of the molecular size is based on the output of an energy minimization calculation using the Spartan program (Wavefunction, Inc.), which suggests that the long-axis dimension of the Cy3 chromophore is ~ 14 Å and the Cy5 chromophore is ~ 16.5 Å. To estimate the transition dipole radius, we first determined the magnitude of the monomer EDTM (≈ 12.8 D for Cy3 and 13.0 D for Cy5, with 1 D = 3.336 ×10^{-30} C m) by numerical integration of the absorption lineshape.[23] We thus obtained a value for the transition dipole radius of ~ 2.7 Å for both Cy3 and Cy5. As we discuss further below, our results indicate that the smallest inter-chromophore separation under the various conditions that we studied is ~ 6 Å for Cy3 and ~3 Å for Cy5. While this separation is small in comparison to the molecular dimension, it remains greater than the transition dipole radius. Based on this assessment alone, it is unclear how much error is introduced by the point dipole approximation. For our current purposes, we apply the point dipole approximation in order to investigate its ability to qualitatively model the resonant coupling strength and our temperature-dependent linear absorption and CD spectra.

In the presence of resonant electronic coupling, the eigenenergies and eigenstates are obtained by diagonalization of the Hamiltonian given by Eq. (2.4). Because of the C_2 symmetry of the chiral cyanine dimer, the singly-electronic-excited states must be either symmetric (sign invariant, $+$) or anti-symmetric (sign inversion, $-$) under C_2 rotation.

Spano and co-workers, who studied the redistribution of oscillator strengths within the vibronic bands of a C_2 symmetric dimer as a function of the resonant exchange coupling, have analyzed this problem in detail.[24] They showed that the symmetric and anti-symmetric eigenstates of the coupled *AB* dimer can be written

$$\left|e_{\pm}^{(\alpha)}\right\rangle = \sum_{n_e=0,1,\ldots} \sum_{n_g=0,1,\ldots} c_{\pm,n_e n_g}^{(\alpha)}(q_A, q_B)[|e_A\rangle \pm |e_B\rangle] \tag{2.7}$$

In Eq. (2.7), $c_{\pm,n_e n_g}^{(\alpha)}$ are complex-valued coefficients that depend on the nuclear coordinates, and $\alpha = 0, 1, 2, \ldots$ in order of increasing state energy. Note that the electronic states $|e_A\rangle$ and $|e_B\rangle$ also depend on the nuclear coordinates. We designate the transition energies of states $\left|e_{\pm}^{(\alpha)}\right\rangle$ as $\varepsilon_{\pm,\alpha}$. Moreover, n_e specifies the vibrational occupancy of the electronically excited monomer site, while n_g specifies that of the electronically unexcited site. It is useful to organize the singly excited states into two different categories. So-called 'one-particle states' are those with variable n_e (= 0, 1, …) vibrational quanta in the shifted potential of the vibronically excited monomer, and n_g = 0 quanta in the un-shifted potential of the electronically unexcited monomer. 'Two-particle states,' on the other hand, are those with variable n_e in the vibronically excited monomer, and $n_g \geq 1$ in the un-shifted potential of the electronically unexcited monomer.[24] The eigenstates given by Eq. (2.7) can thus be re-written as

$$\begin{aligned}\left|e_{\pm}^{(\alpha)}\right\rangle = &\sum_{n_e=0,1,\ldots} c_{\pm,n_e 0}^{(\alpha)}\left[u_{n_e 0}|eg\rangle \pm u_{0 n_e}|ge\rangle\right] \\ &+ \sum_{n_e=0,1,\ldots} \sum_{n_g=1,2,\ldots} c_{\pm,n_e n_g}^{(\alpha)}\left[u_{n_e n_g}|eg\rangle \pm u_{n_g n_e}|ge\rangle\right]\end{aligned} \tag{2.8}$$

where the first and second terms of Eq. (2.8) represent one- and two-particle contributions, respectively. For a given symmetry, the energy eigenstates are superpositions of pure-state contributions; these contributions are of like symmetry, and contain varying levels of vibrational energy.

Dimer Absorption and CD Spectra

We determine the intensities of ground state accessible vibronic transitions of the *AB* dimer using the expression

$$I_{\pm}^{(\alpha)} = \left\langle 0|\, \boldsymbol{\mu}^{tot}|e_{\pm}^{(\alpha)}\right\rangle \left\langle e_{\pm}^{(\alpha)}|\boldsymbol{\mu}^{tot}|0\right\rangle \tag{2.9}$$

where the collective EDTM is given by $\boldsymbol{\mu}^{tot} = \boldsymbol{\mu}_{eg}^{A} + \boldsymbol{\mu}_{eg}^{B}$. The absorption spectrum of the *AB* dimer may thus be decomposed into symmetric and anti-symmetric transition manifolds, which are polarized along the directions of the molecular frame *x*- and *y*-axes, respectively (see Figure 2.2 for coordinate system definitions).

$$\sigma_{H-abs}^{dim}(\varepsilon) = \sigma_{H-abs,+}^{dim}(\varepsilon) + \sigma_{H-abs,-}^{dim}(\varepsilon) \tag{2.10}$$

with

$$\sigma_{H-abs,\pm}^{dim}(\varepsilon) = \sum_{\alpha} \left|\left\langle 0|\, \boldsymbol{\mu}^{tot}|e_{\pm}^{(\alpha)}\right\rangle\right|^{2} L_H\left(\varepsilon - \varepsilon_{\pm,\alpha}\right) \tag{2.11}$$

The CD spectrum is similarly decomposed into polarized components

$$CD_{H}^{dim}(\varepsilon) = \sum_{\alpha} RS_{H+}^{(\alpha)}\; L_H\left(\varepsilon - \varepsilon_{+,\alpha}\right) + \sum_{\alpha} RS_{H-}^{(\alpha)}\; L_H\left(\varepsilon - \varepsilon_{-,\alpha}\right) \tag{2.12}$$

where the rotational strengths for the symmetric and anti-symmetric transitions are given by

$$RS_{H\pm}^{(\alpha)} = \frac{\varepsilon_{eg}}{4\hbar c\left|\mu_{eg}^{0}\right|^{2}} \left\langle 0|\, \boldsymbol{\mu}^{A}|e_{\pm}^{(\alpha)}\right\rangle \times \left\langle e_{\pm}^{(\alpha)}|\boldsymbol{\mu}^{B}|0\right\rangle \cdot \boldsymbol{R}_{AB} \tag{2.13}$$

For both the absorption and CD of the *AB* dimer, we take into account the effects of inhomogeneous broadening using a pseudo-Voigt profile[25] that approximates the convolution given by Eq. (2.3), except using the Gaussian distribution $G_{I,dim}(\varepsilon_{eg})$ specific to the dimer.

Spano and co-workers performed a systematic analysis of the effects of varying exciton interaction strength on the polarized components $(+/-)$ of the absorption and CD spectra of a chiral C_2 symmetric dimer.[24] They used a perturbation theoretical approach to derive expressions for the oscillator strengths of the first two vibronic lineshapes in the weak exciton-coupling regime (i.e. for $|J_{\pm}| \ll \lambda^2\hbar\omega_0$, where $J_{\pm} = \pm J$). In the weak-coupling regime, only single-particle contributions to the eigenstates described by Eq. (2.8) need be considered, so that each $\nu_t - 0$ vibronic band of the monomer spectrum is split into just one upper $(+)$ and one lower $(-)$ energy component. In this regime, the Davydov splitting for each vibronic band of the *AB* dimer is approximately equal to $2Je^{-\lambda^2}\lambda^{2\nu_t}/\nu_t!$. The ratio of the $0-0$ to $1-0$ line strengths is given by

$$\frac{I_{\pm}^{(0-0)}}{I_{\pm}^{(1-0)}} = \frac{1}{\lambda^2}\left[\frac{1 - G(0;\lambda^2)e^{-\lambda^2}J_{\pm}/\hbar\omega_0}{1 - G(1;\lambda^2)e^{-\lambda^2}J_{\pm}/\hbar\omega_0}\right]^2 \tag{2.14}$$

where the effect of the electronic-vibrational coupling is described by the function

$$G(\nu_t;\lambda^2) = \sum_{\substack{u=0,1,\ldots \\ (u\neq\nu_t)}} \frac{\lambda^{2u}}{u!\,(u-\nu_t)} \tag{2.15}$$

In Eq. (2.15), the index ν_t (= 0,1,…) designates the vibronic band of the absorptive transition. As we shall show in Chapters IV, Eq. (2.14) captures the essential behavior of the polarized components of the absorption and CD for the cyanine dye DNA constructs.

From our analysis of the Cy3 monomer spectra (discussed further in Chapter IV) over the pre-melting range 15 – 60 °C, we see that the intramolecular parameters are approximately independent of temperature. We thus obtain the average values: λ^2 = 0.55, $\hbar\omega_0$ = 1,115 cm^{-1}, and ε_{eg} = 18,276 cm^{-1}. Substituting these values into Eqs. (2.14) and (2.15), we obtain $G(\nu_t = 0; 0.55)e^{-0.55}$ = +0.367, $G(\nu_t = 1; 0.55)e^{-0.55}$ = – 0.481, and

$$\frac{I_{\pm}^{(0-0)}}{I_{\pm}^{(1-0)}} = \frac{1}{\lambda^2}\left[\frac{1 - 0.367J_{\pm}/\hbar\omega_0}{1 + 0.481J_{\pm}/\hbar\omega_0}\right]^2 \tag{2.16a}$$

Likewise, for the Cy5 monomer we obtained average values of λ^2 = 0.27, $\hbar\omega_0$ = 1,207 cm^{-1}, and ε_{eg} = 15,496 cm^{-1}. Therefore obtaining $(\nu_t = 0; 0.27)e^{-0.27}$ = +0.221, $G(\nu_t = 1; 0.27)e^{-0.27}$ = – 0.734, and

$$\frac{I_{\pm}^{(0-0)}}{I_{\pm}^{(1-0)}} = \frac{1}{\lambda^2}\left[\frac{1 - 0.221J_{\pm}/\hbar\omega_0}{1 + 0.734J_{\pm}/\hbar\omega_0}\right]^2 \tag{2.16b}$$

From Eqs. (2.16a) and (2.16b), we see that the expected effect of increasing exciton interaction J is to decrease the ratio of the symmetrically polarized components $I_{+}^{(0-0)}/I_{+}^{(1-0)}$, and to increase the ratio of the anti-symmetrically polarized components $I_{-}^{(0-0)}/I_{-}^{(1-0)}$. Thus, the upper energy symmetric excitons, which are polarized in the direction of $\boldsymbol{\mu}_{eg}^{A} + \boldsymbol{\mu}_{eg}^{B}$ (the *x*-axis), tend to be more heavily weighted by single-particle contributions with higher vibrational quantum number ($n_e \geq 1$) than do the lower energy excitons, which are polarized in the direction of $\boldsymbol{\mu}_{eg}^{A} - \boldsymbol{\mu}_{eg}^{B}$ (the *y*-axis). We expect this effect to become more pronounced with increasing resonant coupling interaction.

Numerical Calculations

To perform numerical calculations for the Holstein model of the *AB* dimer, it is convenient to transform Eq. (2.4) to the energy basis using excitation creation / annihilation operators.[20] We adopt the bosonic operators $\hat{b}_M^\dagger = \sqrt{1/2}\left[\sqrt{m\omega_0/\hbar}\,\hat{q}_M - i\,\hat{p}_M/\sqrt{m\omega_0\hbar}\right]$ and $\hat{b}_M = \sqrt{1/2}\left[\sqrt{m\omega_0/\hbar}\,\hat{q}_M + i\,\hat{p}_M/\sqrt{m\omega_0\hbar}\right]$ for the creation and annihilation of vibrational quanta, respectively, within the harmonic potential surfaces associated with the ground electronic states. These operators obey the boson commutation relation $\left[\hat{b}_{M'}, \hat{b}_M^\dagger\right] = \delta_{M'M}$, where $\delta_{M'M}$ is the Kronecker delta function and $M', M \in \{A, B\}$. We further define the operators $\hat{c}_M^\dagger$ and $\hat{c}_M$ to represent the creation and annihilation of electronic quanta, respectively, within the two-level monomer $M = A, B$. Because a single two-electronic-level molecule cannot be excited twice, these operators obey the fermion commutation relation $\left[\hat{c}_{M'}, \hat{c}_M^\dagger\right] = \delta_{M'M}\left(1 - 2\hat{c}_M^\dagger\hat{c}_M\right)$. Using the above definitions and the expression for the Huang-Rhys parameter $\lambda^2 = d^2\omega_0/2\hbar$, the monomer Hamiltonian [Eq. (2.1)] can be recast as

$$\widehat{H}_M = \left\{\varepsilon_{eg}\hat{c}_M^\dagger\hat{c}_M + \hbar\omega_0\hat{b}_M^\dagger\hat{b}_M\hat{I}_M^{elec} + \hbar\omega_0\hat{c}_M^\dagger\hat{c}_M\left[\lambda\left(\hat{b}_M^\dagger + \hat{b}_M\right) + \lambda^2\right]\right\}\hat{I}_{M'\neq M} \qquad (2.17)$$

where, as before, the monomer index $M = A, B$. In Eq. (2.17), the first term on the right-hand side describes the electronic energy of the system, the second term describes the vibrational energies, and the final term describes the coupling between electronic and vibrational states within each monomer. The Hamiltonian for the coupled *AB* system [Eq. (2.4)] can be rewritten as

$$\widehat{H}_{dim} = \widehat{H}_A\hat{I}_B + \widehat{H}_B\hat{I}_A + J\left(\hat{c}_A^\dagger\hat{c}_B + \hat{c}_A\hat{c}_B^\dagger\right)\hat{I}_A^{vib} \otimes \hat{I}_B^{vib} \qquad (2.18)$$

where the expressions for the monomer Hamiltonian $\widehat{H}_{A(B)}$ are given by Eq. (2.17).

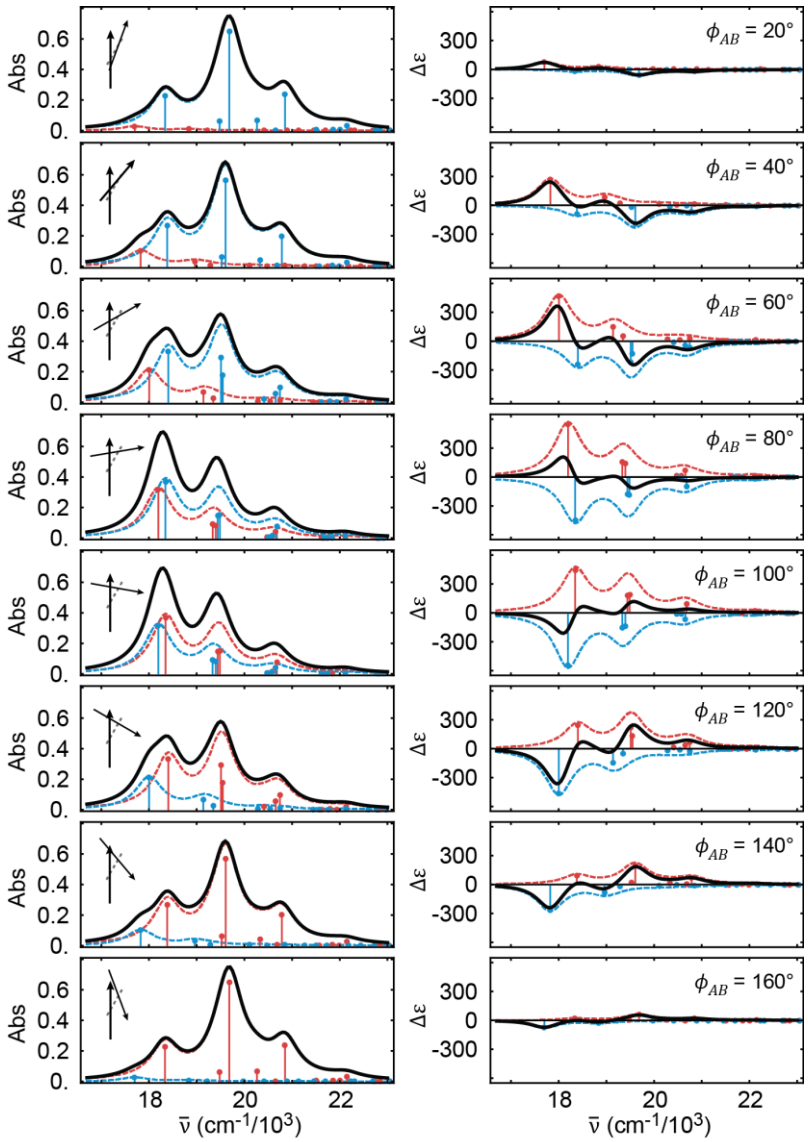

Figure 2.4: The conformational dependence of the absorption and CD spectra as a function of the twist angle ϕ_{AB}. The solid black line is the total absorption or CD signal, the dashed blue (red) are the symmetric (anti-symmetric) components of the total lineshape. The tilt angle and separation distance were fixed, $\delta_{AB} = 0°$ and $R_{AB} = 10\text{Å}$.

From the above equations we can calculate the absorption and CD spectra and examine the conformational sensitivity of these linear spectroscopic techniques. Figure 2.4 presents absorption and CD calculations for various twist angles between two chromophores (in this case Cy3) while the separation distance and tilt angle remain fixed

($R_{AB} = 10$ Å and $\delta_{AB} = 0°$). We see that, in the case of near parallel conformations, the total absorption spectrum is dominated by the transitions in the first vibrational mode and when near perpendicular there is almost equal distribution the symmetric and antisymmetric states.[24,26] In the CD signal, we see the sign inversion of the CD signal when the twist angle exceeds 90° and the coupling constant J becomes negative, likewise beyond 90° the symmetric and anti-symmetric states juxtapose.

Figure 2.4 demonstrates that, under certain conditions, the relative molecular conformation can be determined from the absorption and CD spectra, specifically in cases where one of the conformational parameters can be fixed. such is the case for the tilt angle when considering cyanine dimers labeled within duplex DNA. However, when the constraints are relaxed, such as at DNA fork junctions, and all three conformational parameters are involved in the determination of the structure, fitting just the absorption and CD can lead to multiple degenerate conformations. Under these conditions a more robust spectroscopic tool is necessary to determine the most likely conformation of the system. One such tool is two-dimensional fluorescence spectroscopy (2DFS).

Theoretical Background and Calculation of Two-Dimensional Fluorescence Spectra

Two-dimensional fluorescence spectroscopy (2DFS) has been described in detail elsewhere[23,26–30] and the experimental methodology will be discussed in Chapter III. Briefly, 2DFS utilizes a train of four collinear laser pulses. The relative phase of the first two pulses (Ω_{21}) and that of the second two pulses (Ω_{43}) are continuously swept at distinct frequencies. These pulses excite a molecular system, and the ensuing fluorescence is phase-selectively detected as a function of the time delay between the first two pulses (t_{21}) and

that of the second two pulses (t_{43}), as shown in Figure 2.5 A. The phase selective fluorescence detection method is used to extract the fourth-order population signals, which vary in time at the sum and difference modulation frequencies ($\Omega_{43} + \Omega_{21}$ and $\Omega_{43} - \Omega_{21}$) associated with the non-rephasing (NRP) and rephasing (RP) signal respectively. The two-dimensional Fourier transform of the signal with respect to t_{21} and t_{43} provides a two-dimensional spectrum, represented schematically in Figure 2.5 B. The delay between pulses two and three (t_{32}) is fixed for a given experiment, but subsequent measurements can be taken at varying t_{32} delays. This latter delay is referred to as the population time, and it represents the duration over which the system evolves between the two successive measurements of coherence frequencies.

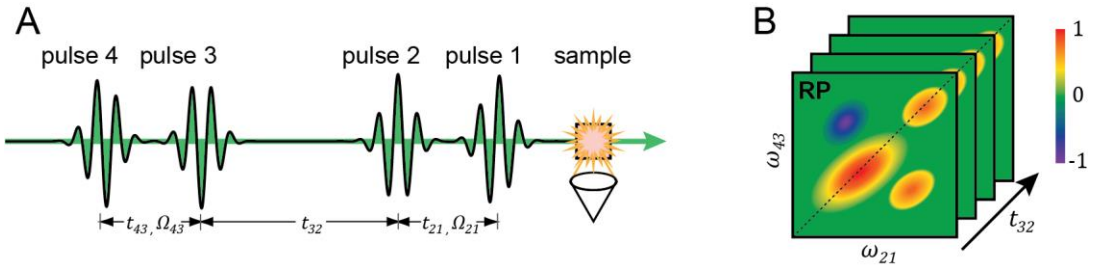

Figure 2.5: (A) The 2DFS pulse sequence indicating the time delays between pulses and the modulation frequencies, modified from Widom et al.[27] **(B)** Illustration of the 2DFS spectra, the data is collected in the time domain and a double Fourier transform with respect to t_{21} and t_{43} results in a spectrum as a function of the frequencies ω_{21} and ω_{43}. Measurements can be taken at successive population (t_{32}) time steps to examine excited state dynamics.

Double-sided Feynman diagrams can be used to represent contributions to the time-dependent density operator in terms of the light-matter interactions that lead to the measured non-rephasing and rephasing signals. These diagrams are presented in Figure 2.6. Here $|0\rangle$ represents the ground electronic state with no vibrational excitations, $|v\rangle$ represents the ground electronic state with $v_A + v_B = v$ vibrational quanta, $|e\rangle$ and $|e'\rangle$ represent any two distinct states within the singly excited manifold, and $|f\rangle$ represents any

one state in the doubly excited manifold. Time runs vertically from bottom to top. In each diagram, the green and blue arrows represent the field-matter electric dipole transition moment interactions, and the dashed red arrow indicates the measured action signal proportional to the final excited state population, which is in this case fluorescence.[19,23]

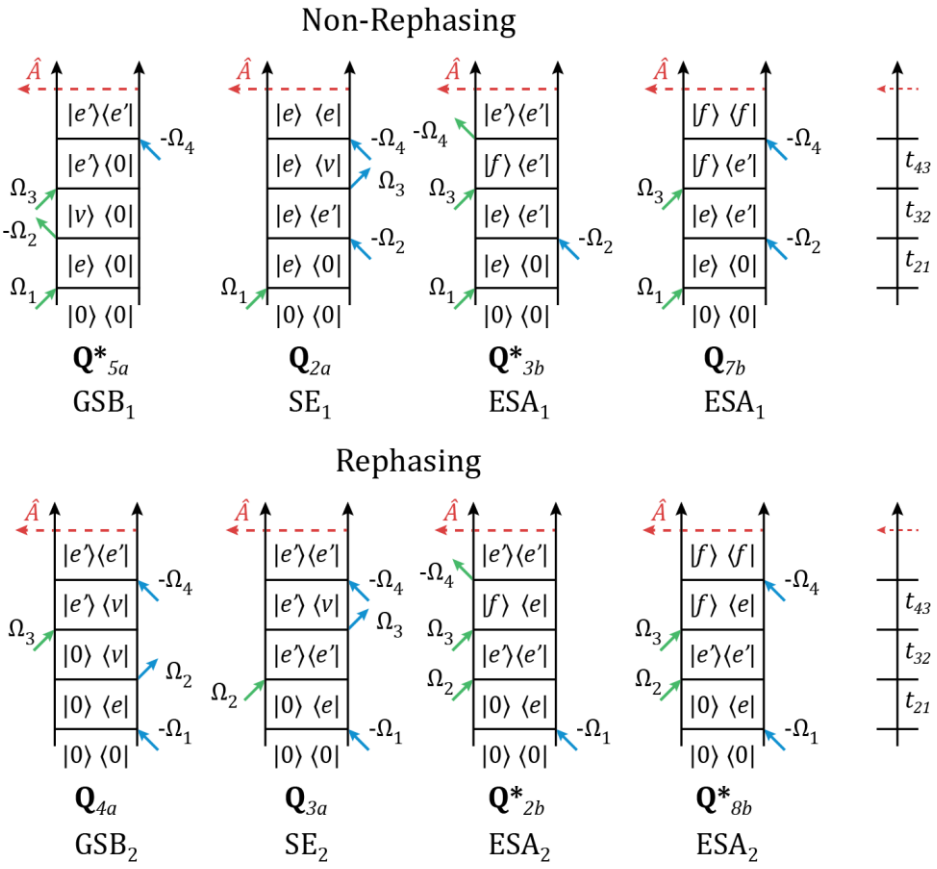

Figure 2.6: Double sided Feynman diagrams representing the light-matter interactions that lead to the measured non-rephasing and rephasing signals. The collective dipole moment allows transitions from the ground state to the singly excited state manifold and from the latter to the final doubly excited state.

The resulting non-rephasing and rephasing 2DFS signals are, respectively, $S_{NRP}(t_{21}, t_{32}, t_{43}) \propto -(Q^*_{5a} + Q_{2a} + Q^*_{3b} - \Gamma_{2d} Q_{7b})$ and $S_{RP}(t_{21}, t_{32}, t_{43}) \propto -(Q_{4a} + Q_{3a} + Q^*_{2b} - \Gamma_{2D} Q^*_{8b})$, where the parameter Γ_{2D} accounts for the different quantum yields between doubly and singly excited state manifolds.

By assuming the rotating wave approximation in the impulsive limit[19] the expressions for the 2DFS rephasing signal can be written as[23]

$$Q_{4a} = \sum_{v,e,e\prime} [\mu_{0e}\mu_{ev}\mu_{e\prime 0}\mu_{ve\prime}]_{\mathbf{e}_1\mathbf{e}_2\mathbf{e}_3\mathbf{e}_4} e^{i\omega_{e0}t_{21}} e^{-i\omega_{0v}t_{32}} e^{-i\omega_{e\prime v}t_{43}} \tag{2.19}$$

$$Q_{3a} = \sum_{v,e,e\prime} [\mu_{0e}\mu_{e\prime 0}\mu_{ev}\mu_{ve\prime}]_{\mathbf{e}_1\mathbf{e}_2\mathbf{e}_3\mathbf{e}_4} e^{i\omega_{e0}t_{21}} e^{-i\omega_{e\prime e}t_{32}} e^{-i\omega_{e\prime v}t_{43}} \tag{2.20}$$

$$Q_{2b}^{*} = Q_{8b}^{*} = \sum_{e,e\prime,f} [\mu_{0e}\mu_{e\prime 0}\mu_{fe\prime}\mu_{ef}]_{\mathbf{e}_1\mathbf{e}_2\mathbf{e}_3\mathbf{e}_4} e^{i\omega_{e0}t_{21}} e^{-i\omega_{e\prime e}t_{32}} e^{-i\omega_{fe}t_{43}} \tag{2.21}$$

and the expressions for the non-rephasing signal are

$$Q_{5a}^{*} = \sum_{v,e,e\prime} [\mu_{e0}\mu_{ve}\mu_{e\prime v}\mu_{0e\prime}]_{\mathbf{e}_1\mathbf{e}_2\mathbf{e}_3\mathbf{e}_4} e^{-i\omega_{e0}t_{21}} e^{-i\omega_{v0}t_{32}} e^{-i\omega_{e\prime 0}t_{43}} \tag{2.22}$$

$$Q_{2a} = \sum_{v,e,e\prime} [\mu_{e0}\mu_{0e\prime}\mu_{e\prime v}\mu_{ve}]_{\mathbf{e}_1\mathbf{e}_2\mathbf{e}_3\mathbf{e}_4} e^{-i\omega_{e0}t_{21}} e^{-i\omega_{ee\prime}t_{32}} e^{-i\omega_{e\prime v}t_{43}} \tag{2.23}$$

$$Q_{3b}^{*} = Q_{7b} = \sum_{e,e\prime,f} [\mu_{e0}\mu_{0e\prime}\mu_{fe}\mu_{e\prime f}]_{\mathbf{e}_1\mathbf{e}_2\mathbf{e}_3\mathbf{e}_4} e^{-i\omega_{e0}t_{21}} e^{-i\omega_{ee\prime}t_{32}} e^{-i\omega_{fe\prime}t_{43}} \tag{2.24}$$

where $[\mu_{ab}\mu_{cd}\mu_{jk}\mu_{lm}]_{\mathbf{e}_1\mathbf{e}_2\mathbf{e}_3\mathbf{e}_4}$ denotes the three-dimensional orientational average product $\langle(\boldsymbol{\mu}_{ab}\cdot\mathbf{e}_1)(\boldsymbol{\mu}_{cd}\cdot\mathbf{e}_2)(\boldsymbol{\mu}_{jk}\cdot\mathbf{e}_3)(\boldsymbol{\mu}_{lm}\cdot\mathbf{e}_4)\rangle$, where $\mathbf{e}_i$ is the polarization of the i[th] pulse,[23,31,32] in the current experiments all laser pulses have the same polarization.

To account for spectral broadening in the 2DFS lineshape, the homogeneous broadening is included using a Lorentzian function with a FWHM given by Γ_H, the same homogeneous width used in the calculation of the absorption and CD spectra. The inhomogeneous broadening is included phenomenologically by convolving the response

functions with a Gaussian distribution, as was done by Grégoire et al,[33] where the convolution integral for the rephasing signal (setting $t_{32} = 0$) is

$$\int_{-\infty}^{\infty} d\omega_{ij}\, e^{-\frac{\left(\omega_{ij}-\omega_{ij}^{(0)}\right)^2}{2\sigma_I^2}}\, e^{-\Gamma_H(t_{21}+t_{43})}\, e^{-i\left(\omega_{ij}t_{43}-\omega_{ij}t_{21}\right)} \tag{2.25}$$

For the NRP signal, the inhomogeneous broadening is accounted for using the convolution integral

$$\int_{-\infty}^{\infty} d\omega_{ij}\, e^{-\frac{\left(\omega_{ij}-\omega_{ij}^{(0)}\right)^2}{2\sigma_I^2}}\, e^{-\Gamma_H(t_{21}+t_{43})}\, e^{-i\left(\omega_{ij}t_{43}+\omega_{ij}t_{21}\right)} \tag{2.26}$$

In Eqs. (2.25) and (2.26), σ_I is the standard deviation of the inhomogeneously broadened lineshape, and $\omega_{ij}^{(0)}$ is the reference transition frequency.

Using the convolution theorem[34,35] the expressions for the rephasing and non-rephasing signals (for the case $t_{32} = 0$) become

$$Q_{4a} = \sum_{v,e,e\prime} [\mu_{0e}\mu_{ev}\mu_{0e\prime}\mu_{ve\prime}]_{\mathbf{e_1e_2e_3e_4}}\, e^{-\Gamma_H(t_{21}+t_{43})-\frac{1}{2}\sigma_I^2(t_{21}-t_{43})^2+i(\omega_{e\prime v}t_{43}-\omega_{e0}t_{21})} \tag{2.27}$$

$$Q_{3a} = \sum_{v,e,e\prime} [\mu_{0e}\mu_{e\prime 0}\mu_{ev}\mu_{ve\prime}]_{\mathbf{e_1e_2e_3e_4}}\, e^{-\Gamma_H(t_{21}+t_{43})-\frac{1}{2}\sigma_I^2(t_{21}-t_{43})^2+i(\omega_{e\prime v}t_{43}-\omega_{e0}t_{21})} \tag{2.28}$$

$$\begin{aligned} Q_{2b}^* &= Q_{8b}^* \\ &= \sum_{e,e\prime,f} \left[\mu_{0e}\mu_{e\prime 0}\mu_{fe\prime}\mu_{ef}\right]_{\mathbf{e_1e_2e_3e_4}}\, e^{-\Gamma_H(t_{21}+t_{43})-\frac{1}{2}\sigma_I^2(t_{21}-t_{43})^2+i\left(\omega_{fe}t_{43}-\omega_{e0}t_{21}\right)} \end{aligned} \tag{2.29}$$

$$Q_{5a}^* = \sum_{v,e,e\prime} [\mu_{e0}\mu_{ve}\mu_{e\prime v}\mu_{0e\prime}]_{\mathbf{e_1e_2e_3e_4}}\, e^{-\Gamma_H(t_{21}+t_{43})-\frac{1}{2}\sigma_I^2(t_{21}+t_{43})^2+i(\omega_{e\prime 0}t_{43}+\omega_{e0}t_{21})} \tag{2.30}$$

$$Q_{2a} = \sum_{v,e,e\prime} [\mu_{e0}\mu_{0e\prime}\mu_{e\prime v}\mu_{ve}]_{\mathbf{e_1e_2e_3e_4}}\, e^{-\Gamma_H(t_{21}+t_{43})-\frac{1}{2}\sigma_I^2(t_{21}+t_{43})^2+i(\omega_{e\prime v}t_{43}+\omega_{e0}t_{21})} \tag{2.31}$$

$$Q_{3b}^{*} = Q_{7b}$$
$$= \sum_{e,e\prime,f} \left[\mu_{e0}\mu_{0e\prime}\mu_{fe\prime}\mu_{e\prime f}\right]_{\mathbf{e_1 e_2 e_3 e_4}} e^{-\Gamma_H(t_{21}+t_{43})-\frac{1}{2}\sigma_I^2(t_{21}+t_{43})^2+i\left(\omega_{fe}t_{43}+\omega_{e0}t_{21}\right)} \tag{2.32}$$

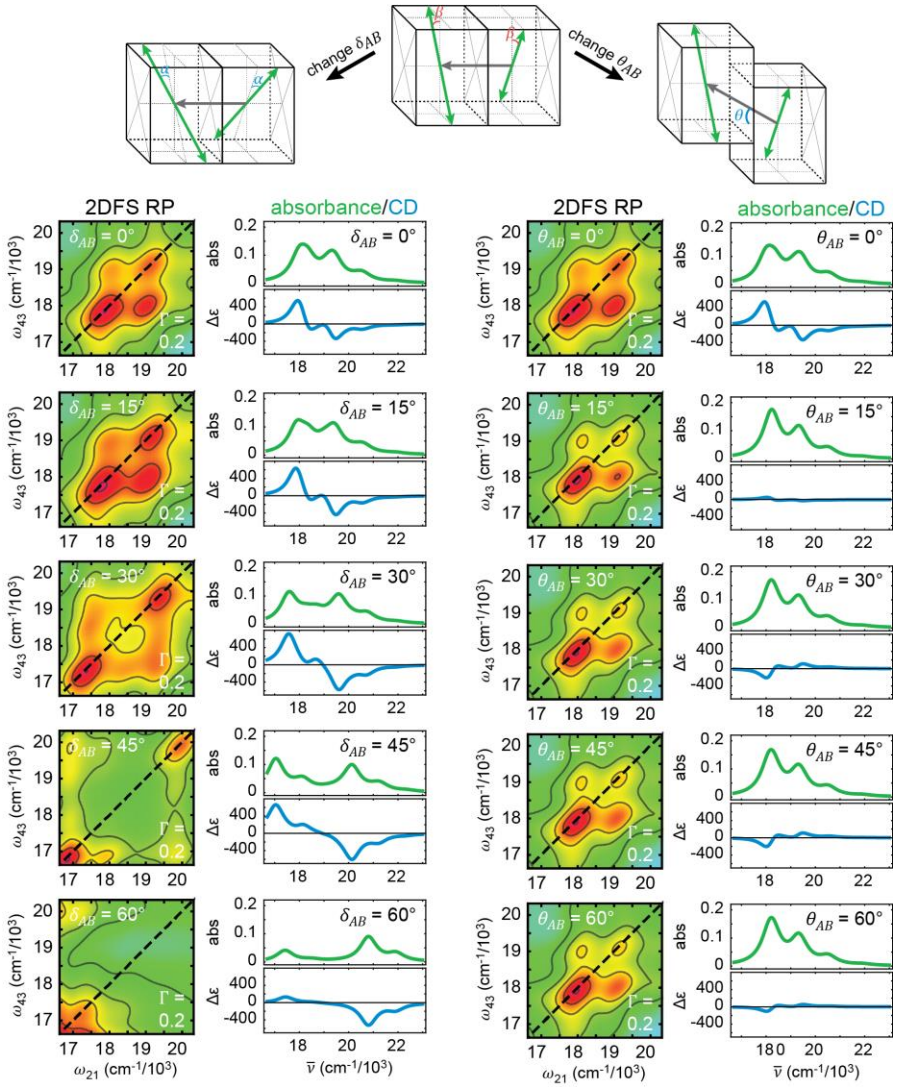

Figure 2.7: Conformational dependence of the 2DFS, absorbance, and CD spectra. The real part of the RP signal and the absorbance and CD spectra are shown for varying conformations. On the left, the tilt angle, δ_{AB} (2α) is varied from 0 to 60°. Changes in the tilt angle result in significant changes to the 2D spectra and the linear spectra. On the right, the slip angle, θ_{AB} is varied from 0 to 60°.

Figure 2.7 presents the RP spectra calculated from Eqs. (2.27) – (2.29), in addition to the absorbance and CD spectra, for varying degrees of inter-chromophore tilt or slip.

The inter-chromophore twist and separation were held constant at $\phi_{AB} = 85°$ and $R_{AB} = 6$ Å.

Corrections to Account for the Finite Laser Bandwidth

To account for the finite bandwidth of the laser, we include a correction based on the spectral overlap between the laser and the inhomogeneously broadened transitions as was done previously.[26] To account for the non-Gaussian laser spectrum, we modeled the laser spectrum as a super Gaussian

$$g(\omega) = e^{-\left(\frac{(\omega-\omega_L)^2}{2\sigma_L^2}\right)^{b_L}} \tag{2.33}$$

where ω_L is the center frequency of the laser spectrum, σ_L is the standard deviation of the laser spectrum, and b_L is a parameter with modifies the profile of the Gaussian such that $b_L = \infty$ reproduces the flat top function.

The inhomogeneously broadened spectral features are represented by the function

$$a_{ij}(\omega) = e^{-\frac{(\omega-\omega_{ij})^2}{2\sigma_I^2}} \tag{2.34}$$

where ω_{ij} is the transition center frequency, σ_I is the inhomogeneous standard deviation.

For a given transition, we determined the simulated 2DFS spectrum from the spectral overlap function $g(\omega)a_{ij}(\omega)$. We thus adjusted the transition center frequency by finding the first moment

$$\omega_{ij} \to \widetilde{\omega}_{ij} = \frac{\int_{-\infty}^{\infty} d\omega\ \omega e^{-\frac{(\omega-\omega_{ij})^2}{2\sigma_I^2}} e^{-\left(\frac{(\omega-\omega_L)^2}{2\sigma_L^2}\right)^{b_L}}}{\int_{-\infty}^{\infty} d\omega\ e^{-\frac{(\omega-\omega_{ij})^2}{2\sigma_I^2}} e^{-\left(\frac{(\omega-\omega_L)^2}{2\sigma_L^2}\right)^{b_L}}} \tag{2.35}$$

and we adjusted the weight of the transition, which was determined by the laser amplitude according to

$$\alpha(\omega) \rightarrow \tilde{\alpha}(\omega) = e^{-\frac{\left(\omega-\omega_{ij}\right)^2}{2\sigma_I^2}} e^{-\left(\frac{(\omega-\omega_L)^2}{2\sigma_L^2}\right)^{b_L}} \tag{2.36}$$

These corrections are only valid in the case where the transitions are independent of one another, such as the case of the dimer. In the case of the monomer, the transitions are all shifted equally due to the overlap of the laser and the 'dominant' feature, such that the vibrational mode frequency remains constant.

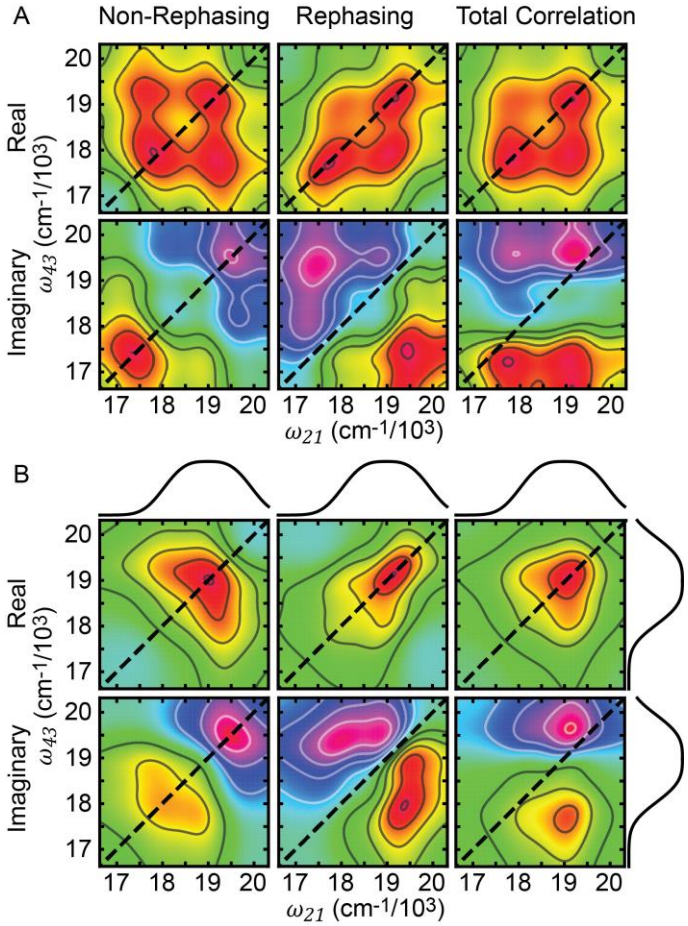

Figure 2.8: Comparison of the calculated 2D spectra without and with the correction for the limited bandwidth of the laser. **(A)** Using a white light continuum to excite the system. **(B)** The super-Gausian laser profile is shown above and to the right of the 2D plots (ω_L = 18989.5 cm^{-1} ≈ 526 nm, σ_L = 544 cm^{-1}, and b_L = 1.55). Incorporation of the laser selectively excites spectral features.

Figure 2.8 compares the calculated 2DFS spectra given by Eqs. (2.27) – (2.32) when a white light excitation is used versus when the limited bandwidth is implemented using the corrections given by Eq. (2.35) and Eq. (2.36).

Summary and Bridge to Chapter III

In this chapter we described the Holstein Hamiltonian model used to describe the vibronic character of the excitonically coupled cyanine dimer systems. We also examined the calculations necessary to interpret absorption, CD, and 2DFS spectra. These complementary techniques provide a robust framework for the determination of the local conformation of excitonically coupled chromophores. In Chapter VI the experimental details of these techniques will be described.

CHAPTER III

EXPERIMENTAL CONSIDERATIONS

Overview

This chapter provides an overview of the experimental considerations including sample conditions, spectroscopic techniques, and the mathematical optimization procedure used in this study of excitonically coupled molecular systems. This section contains co-authored work. L. Scatena advised and aided in the construction of the noncollinear optical parametric amplifier and A. Tamimi constructed the double pass fused silica prism pair pre-dispersion compensation setup. This chapter also contains material that has been published as L. Kringle, N. P. D. Sawaya, J. Widom, C. Adams, M. G. Raymer, A. Aspuru-Guzik, and A. H. Marcus, "Temperature-dependent conformations of exciton-coupled Cy3 dimers in double-stranded DNA," *J. Chem. Phys*. **148**, 085101 (2018). In the section used here, I designed and performed the multiparameter optimizations using a computational code derived from that written by N. P. D. Sawaya. A. H. Marcus collaborated in planning the experimental techniques required and the remaining co-authors provided editorial assistance.

Introduction

The previous chapter discussed the theory behind the spectroscopic techniques employed throughout this work and the mathematical model used to describe the excitonically coupled molecular system. The experiments involve the use of three complementary techniques, absorption, circular dichroism (CD) and two-dimensional

fluorescence spectroscopy (2DFS) to examine the local structure and excited state dynamics of cyanine dye labeled DNA. These experiments provide insight into the intra-molecular parameters of the cyanine dyes and the structural parameters resulting in excitonic coupling of the system. A computational optimization procedure is used to determine the average conformation of the ensemble by fitting all three types of spectra to the model described in Chapter II. What follows in this chapter is a discussion of the experimental considerations for the study of the cyanine dye labeled DNA constructs. A description of the constructs including probe position will first be discussed. A description of the absorption and CD experiments including experimental conditions will follow. Finally, a description of the laser system necessary for the 2DFS measurements including the details of the homebuilt noncollinear optical parametric amplifier.

Sample Preparation

Constructs were chosen in which the cyanine probe was positioned deep within the duplex region of DNA and near the single-stranded (ss) – double-stranded (ds) fork junctions. These probe positions were chosen to examine the regions of interest for biological functions through characterization of the positional dependence of the local structure and fluctuations of the DNA duplex and fork junction.[1,2] Both cyanine dyes Cy3 and Cy5 were used throughout this dissertation, the molecular structure and linkages to the DNA backbone can be seen in Figure 1.1.

The sequences and nomenclature of the internally labeled cyanine dye – DNA constructs used in this work are shown in Table 3.1 and 3.2. The double stranded constructs were formed by combining complementary oligonucleotide single stranded DNA

constructs to form the monomer and dimer labeled constructs. The constructs were created to reproduce the structure at DNA replication fork junctions, where each construct (aside from Dds and Uds) contains a pair of noncomplementary strands and a base-paired duplex region, where the duplex region is marked by the horizontal line between the two strands.

The first set of constructs (Table 3.1), with >50 nucleotides per ssDNA strand, examined both Cy3 and Cy5 when labeled deep in the duplex of DNA or at fork junctions with long ssDNA tails. The prefix 'D' or 'F' is used to indicate whether the probes are located within the double stranded duplex region or at the fork junction, respectively. The corresponding monomer constructs have a thymine base opposing the Cy3 or Cy5 dye. The constructs were purchased from Integrated DNA Technologies (IDT, Coralville, IA) and used as received.

Table 3.1: Base sequences and naming convention of the Cy3 and Cy5 dimer DNA constructs, where **X** indicates the position of the cyanine dye. The horizontal line indicates the regions of complementary base pairing.

Name	Nucleotide Base Sequence
$D(X)_2$ Duplex Dimer	3'-GTC AGT ATT ATA CGC T**X**C GCT AAT ATA TAC GTT TTT TTT TTT TTT TTT TTT TTT TTT T-5' 5'-CAG TCA TAA TAT GCG A**X**G CGA TTA TAT ATG CTT TTA CCA CTT TCA CTC ACG TGC TTA C-3'
D(X) Duplex Monomer	3'-GTC AGT ATT ATA CGC T**X**C GCT AAT ATA TAC GTT TTT TTT TTT TTT TTT TTT TTT TTT T-5' 5'-CAG TCA TAA TAT GCG ATG CGA TTA TAT ATG CTT TTA CCA CTT TCA CTC ACG TGC TTA C-3'
$F(X)_2$ Fork Dimer	3'-GAG GGA GCA CAG CAG AGG TCA GTA TTA TAC GCT **X**CG CTG GTA TAC CAC GTT T (x29)-5' 5'-CTC CCT CGT GTC GTC TCC AGT CAT AAT ATG CGA **X**AT GCT TTT ACC ACT TTC ACT CAG GTG CTT A-3'
F(X) Fork Monomer	3'-GAG GGA GCA CAG CAG AGG TCA GTA TTA TAC GCT **X**CG CTG GTA TAC CAC GTT T (x29)-5' 5'-CTC CCT CGT GTC GTC TCC AGT CAT AAT ATG CGA TAT GCT TTT ACC ACT TTC ACT CAG GTG CTT A-3'

The second set of DNA constructs (Table 3.2), with <30 nucleotides per ssDNA strand, examined the effect of probe position relative to the fork junction on the conformation of the Cy3 chromophores. The naming scheme for these constructs was adopted from the previously established convention.[1,2] Positive numbers correspond to probe positions within the duplex region of the DNA where the numerical value designates

the number of base pairs from the fork junction, and negative numbers indicate the probe position within the noncomplementary single stranded region as shown in Figure 3.1. The prefix ‘D’ or ‘M’ is used to indicate the dimer versus monomer constructs respectively. The monomer constructs of this family of samples do not have a thymine base opposing the dyes. The constructs were purchased from Fidelity Systems (Gaithersburg, MD) and used as received.

Table 3.2: Base sequences and naming convention of the Cy3 dimer DNA constructs used to examine the structural variation near the fork junction. The horizontal line indicates the regions of complementary base pairing

Name	Nucleotide Base Sequence
Dds	3′-GAT TAT ACG CTC GCT **Cy3**AA TAT ACC ACG-5′ 5′-CTA ATA TGC GAG CGA **Cy3**TT ATA TGG TGC-3′
Mds	3′-GAT TAT ACG CTC GCT **Cy3**AA TAT ACC ACG-5′ 5′-CTA ATA TGC GAG CGA TT ATA TGG TGC-3′
Uds	3′-GAT TAT ACG CTC GCT AA TAT ACC ACG-5′ 5′-CTA ATA TGC GAG CGA TT ATA TGG TGC-3′
D3	3′-GAT TAT ACG CTC GCT **Cy3**AA TAT ACC ACG-5′ 5′-CTA ATA TGC GAG CGA **Cy3**TT AGC ACA GTA-3′
M3	3′-GAT TAT ACG CTC GCT **Cy3**AA TAT ACC ACG-5′ 5′-CTA ATA TGC GAG CGA TT AGC ACA GTA-3′
D2	3′-GAT TAT ACG CTC GCT **Cy3**AA TAT ACC ACG-5′ 5′-CTA ATA TGC GAG CGA **Cy3**TT TGC ACA GTA-3′
M2	3′-GAT TAT ACG CTC GCT **Cy3**AA TAT ACC ACG-5′ 5′-CTA ATA TGC GAG CGA TT TGC ACA GTA-3′
D1	3′-GAT TAT ACG CTC GCT **Cy3**AA TAT ACC ACG-5′ 5′-CTA ATA TGC GAG CGA **Cy3**TA TGC ACA GTA-3′
M1	3′-GAT TAT ACG CTC GCT **Cy3**AA TAT ACC ACG-5′ 5′-CTA ATA TGC GAG CGA TA TGC ACA GTA-3′
D-1	3′-GAT TAT ACG CTC GCT **Cy3**AA TAT ACC ACG-5′ 5′-CTA ATA TGC GAG CGA **Cy3**AA TGC ACA GTA-3′
M-1	3′-GAT TAT ACG CTC GCT **Cy3**AA TAT ACC ACG-5′ 5′-CTA ATA TGC GAG CGA AA TGC ACA GTA-3′
D-2	3′-GAT TAT ACG CTC GCT **Cy3**AA TAT ACC ACG-5′ 5′-CTA ATA TGC GAG CGT **Cy3**AA TGC ACA GTA-3′
M-2	3′-GAT TAT ACG CTC GCT **Cy3**AA TAT ACC ACG-5′ 5′-CTA ATA TGC GAG CGT AA TGC ACA GTA-3′

We prepared solutions using standard Tris or HEPES buffers. The Tris buffer contained 10 mM Tris, 100 mM NaCl, and 6 mM $MgCl_2$, while the HEPES buffer

contained 20 mM HEPES pH 7.5, 100 mM NaOAc, 10 mM $Mg(OAc)_2$, and 0.1 mM EDTA. Experiments used DNA construct concentrations of 400 nM – 1 μM DNA. Prior to the experiments, the sample solutions were annealed by heating to 95°C for 3 minutes before they were allowed to slowly cool overnight.

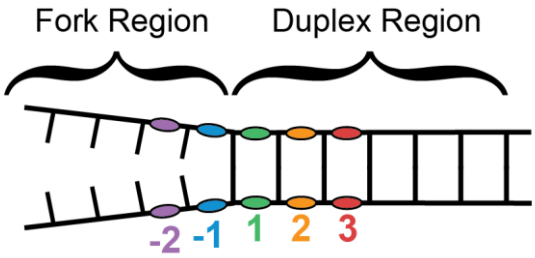

Figure 3.1: Schematic representation of the probe position labeling scheme used to describe the samples in which the Cy3 position varied relative to the fork.

Linear Spectroscopic Methods

Linear absorption measurements were carried out for each sample using a Cary 3E UV-Vis spectrophotometer, and CD measurements were performed using a Jasco model J-720 or model J-815 CD spectrophotometer. The instruments were equipped with a computer-controlled temperature stage, which held the solutions in a 1 cm quartz cuvette. Absorption and CD spectra were measured over the range 200 – 700 nm to simultaneously examine the spectral region of the native bases (~275 nm) in addition to that of the Cy3 probe(s) (~540 nm) or Cy5 probe(s) (~645 nm).

Nonlinear Spectroscopic Methods

An introduction to two-dimensional fluorescence spectroscopy (2DFS) was given in Chapter II and additional details of the experimental setup have been previously described.[3–8] Figure 3.2 diagrams the laser system, and I will briefly describe the essential

aspects here. A regenerative amplifier Ti:Sapphire system (Coherent RegA 9000) is used to generate laser pulses with a repetition rate of 140 kHz. The center frequency of the laser pulses is modified using a homebuilt noncollinear-optical parametric amplifier, and a prism pair compressor is used for pre-dispersion compensation. The laser pulses are split between two Mach Zehnder Interferometers (MZI) where the relative phases of the pulses (Ω_{21} and Ω_{43}) are modulated with acousto-optic Bragg cells. Computer controlled delay stages within the MZIs are used to vary the time delay between the pulses (t_{21} and t_{43}). Pulses three and four are reflected off a third delay stage which sets the population time, t_{32}. The pulses are recombined and excite the sample, which is continuously circulated through the cuvette using a peristaltic pump to eliminate optical saturation effects. The emission is detected through a long pass filter chosen to reject scattered laser light. Lock-in amplifiers select out the fluorescence signal at the sum and difference of the modulated frequencies, using optical references generated from the monochromators.

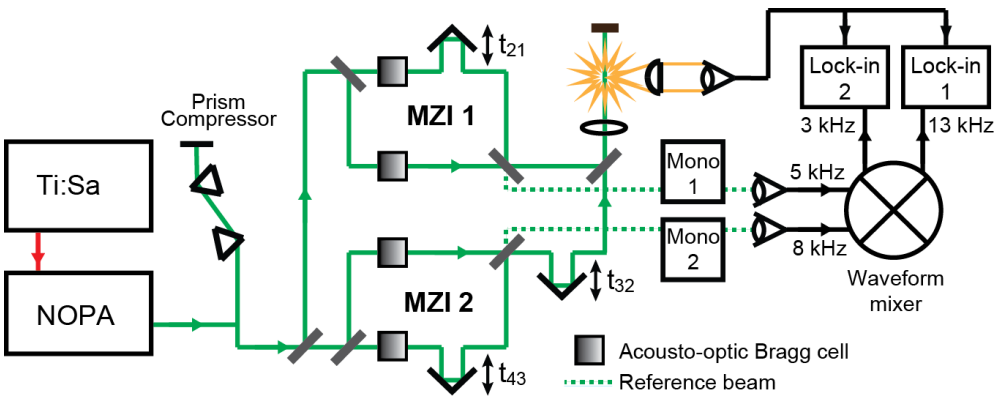

Figure 3.2: Schematic of the 2DFS laser system. Acousto-optic Bragg cells are used to control the phase difference frequencies between pulses 1 and 2 (5 kHz) and pulses 3 and 4 (8 kHz). Optical references are used to generate the sum and difference (13 kHz and 3 kHz) references for the lock-in detection.

The sum and difference signals correspond to the non-rephasing (NRP) and rephasing spectra (RP), with real and imaginary contributions given by the signal that is in

phase or in quadrature relative to the reference. The in-phase component is maximized at $t_{21} = t_{43} = 0$. The total correlation spectrum is obtained from adding the NRP and RP spectra. Thus, for in a single 2DFS measurement six 2D spectra are collected.

High-Repetition Rate Noncollinear Optical Parametric Amplifier

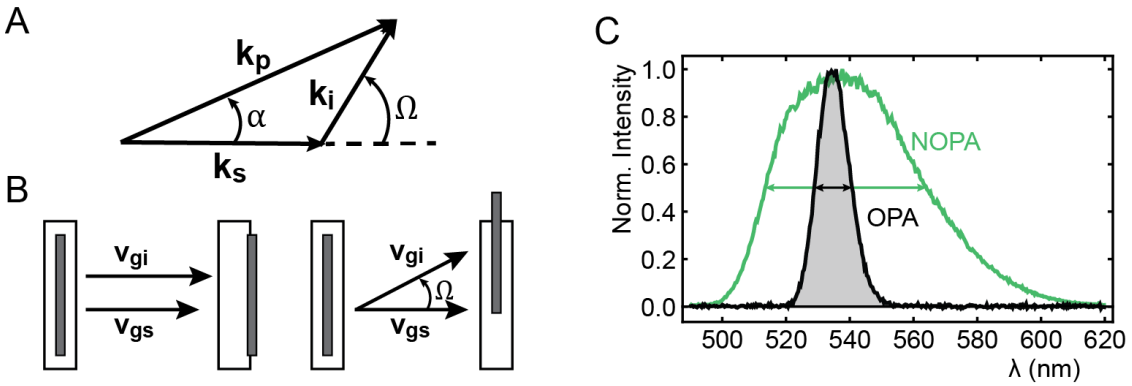

Figure 3.3: (A) Diagram of the noncollinear interaction geometry. Where $\mathbf{k}_s$, $\mathbf{k}_p$, and $\mathbf{k}_i$ are the wave vectors of the signal, pump and idler respectively. The angle between the signal and pump is given by α and between the signal and idler is Ω. **(B)** Illustration depicting the signal and idler pulses in the collinear and noncollinear interactions. On the left, the walk off due to the GVM quickly separate signal and idler. On the right, the pulses remain effectively overlapped in the noncollinear geometry.[9] **(C)** Comparison between the laser spectra obtained with the commercial OPA (black line) and the homebuilt NOPA (green line).

To generate the broadband laser pulses capable of exciting multiple vibrational modes of the cyanine dyes simultaneously, we built a high-repetition rate noncollinear optical parametric amplifier (NOPA). Optical parametric amplifiers work by transferring energy from a high-power fixed frequency pump beam to a low power seed beam in a nonlinear crystal.[9] The group velocity mismatch (GVM) of the signal and idler beams is the limiting factor in the bandwidth generated by the optical parametric amplifier. In the traditional, linear version of the optical parametric amplifier, the signal and idler quickly separate temporally which, in turn reduces the bandwidth. By using a noncollinear

geometry, in which the signal and pump beam are at ang angle α and the signal and idler are at an angle Ω, as shown in Figure 3.3 A, the pulses remain effectively overlapped within the nonlinear crystal such that greater bandwidth can be achieved, this is shown pictorially in Figure 3.3B. The result is a greater spectral bandwidth shown in Figure 3.3C.

Our NOPA design was modeled after that published by Manzoni, Polli, and Cerullo,[10] and is presented in Figure 3.4. The 800 nm, ~8 μJ beam enters the NOPA and is split into two paths, to generate the pump and the seed. The pump is generated by second harmonic generation using a BBO crystal (Type I, θ = 30°). The seed path is reflected off a micrometer translation stage and then focused into a sapphire crystal (2 mm thickness) to produce the white light continuum that is used as a seed. Reflective optics are used to focus the white light into the nonlinear BBO crystal (Type I, θ = 29°). The pump and the seed beams are set to a crossing angle of 3.7° internally within the crystal (6.4° measured externally). Amplification occurs when the pump and seed overlap spatially and temporally. Because the white light seed is chirped the center wavelength of the amplified signal can be tuned using the translation stage in the path of the white light generation. With this setup, we generated pulses with bandwidths up to 50 nm, centered at 540 nm, as shown in Fig. 3.3C. In comparison to the 12 nm pulses generated from the commercial linear geometry optical parametric amplifiers (Coherent, Inc.).

Due to the high repetition rate laser used, the home-built NOPA was sensitive to self-focusing, self-phase modulation, and crystal burning. To reduce the effects of self-focusing, the nonlinear BBO crystal was placed slightly after the focus of the pump beam. Likewise, to reduce the self-phase modulation the second harmonic generation BBO crystal was walked off from the focus and a larger beam waist was used. Additionally, we placed

the sapphire crystal on an XY optics positioner mount, so the crystal could be translated away from burn spots.

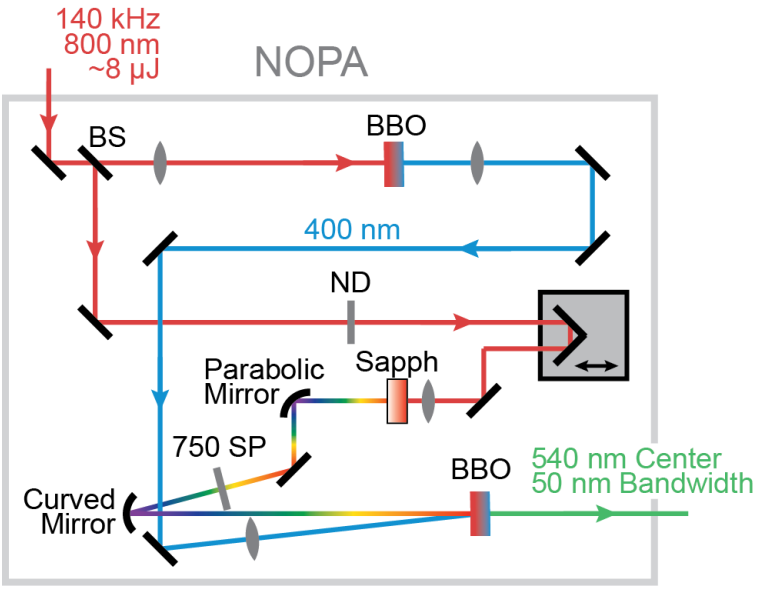

Figure 3.4: Schematic of the homebuilt NOPA. The 800 nm (red) laser pulses are split and used to generate the 400 nm (blue) pump and white light (rainbow) seed beams. The pump and seed are recombined using a noncolinear geometry in the BBO, generating the broadband, center frequency tunable laser pulses.

Pulses were compressed using a double-pass glass SF10 prism pair (for bandwidths less than 20 nm) or a fused silica prism pair (for bandwidths greater than 20 nm) to compensate for dispersive media in the optical path preceding the sample, as previously described.[3] To reduce the table space needed for the fused silica prism pair (~1.5 m inner prism path length), a doubly folded double prism pair setup was constructed as described by Muller et al.[11] Pulse widths were characterized by placing a beta-barium borate (BBO) frequency doubling crystal at the sample position, where a phase-modulated train of pulse-pairs was incident. The frequency-doubled signal output was detected using a lock-in amplifier, which was referenced to the ac carrier signal used to modulate the relative phase of the pulses. We thus minimized the pulse width $\Delta\tau_L$ by performing a pulse-pulse

autocorrelation. Assuming Gaussian pulse shapes the corresponding time-bandwidth products [$\Delta\tau_L(\Delta\lambda_L c/\lambda_L^2)$] are ~0.53 and ~0.92 respectively, <20% and ~50% transform limited.

Multi-Parameter Optimization Procedure

In order to characterize the absorption and CD spectra of the monomer and dimer DNA constructs [given by Eqs. (2.2), (2.11) and (2.12)], it was necessary to obtain an estimate of the homogeneous line width. The effects of pure dephasing – i.e. coupling to the phonon bath that rapidly modulates the monomer transition energy – dominate the homogeneous line width.[12] Since pure dephasing exhibits only a weak temperature-dependence, the homogeneous line width is not expected to change significantly over the range of temperatures we investigated (15 – 85 °C). We therefore used 2DFS measurements to determine the FWHM Lorentzian line width, Γ_H = 186 cm^{-1}, of both monomer and dimer-labeled DNA samples at room temperature, and we assumed this value to be constant for our analysis of the absorption and circular dichroism spectra.

We see from Eqs. (2.1) – (2.3) that absorption spectra of the monomer may be characterized using four independent parameters: (i) the monomer electronic transition energy ε_{eg}, (ii) the Huang-Rhys electronic-vibrational coupling parameter λ^2, (iii) the single-mode vibrational frequency ω_0, and (iv) the spectral inhomogeneity parameter of the monomer specified by the Gaussian standard deviation $\sigma_{I,mon}$. It is also necessary to specify the magnitude of the monomer EDTM ($|\mu_{eg}^0|$ = 12.8 D and $|\mu_{eg}^0|$ = 13.0 D for Cy3 and Cy5 respectively) [see Eq. (2.2)], which we determined by integrating the experimental absorption lineshape as in past work.[5] To characterize fully the absorption and CD spectra

of the coupled dimer [see Eqs. (2.4), (2.11), (2.12)], we must additionally specify: v) the inter-chromophore separation R_{AB}, (vi) the inter-chromophore twist angle ϕ_{AB}, (vii) the inter-chromophore tilt angle δ_{AB}, and (viii) the spectral inhomogeneity parameter $\sigma_{I,dim}$ associated with the dimer. The inter-chromophore slip angle θ_{AB} was neglected in this work. The values of the structural parameters R_{AB}, ϕ_{AB}, and δ_{AB} determine the resonant coupling strength J according to Eq. (2.6).

In order to obtain the most favorable comparison between simulated and experimental absorption and CD spectra, we implemented an automated multi-variable regression analysis to efficiently explore the space of input parameters (i) – (viii). The procedure is similar to one we have used in past studies,[5,6,13] in which a random search algorithm generates an initial set of input parameters, and commercial software (KNITRO)[14] is used to refine the corresponding solutions. For each set of input trial parameters, we calculate a linear least-squares target function χ^2, which guides the selection of parameter values for subsequent iterations. The optimized solutions correspond to minimization of the target function.

We initially applied the above optimization procedure to the duplex labeled Cy3 monomer absorption spectrum taken at 15°C by minimizing the target function $\chi^2_{abs,mon}(\varepsilon_{eg}, \lambda^2, \omega_0, \sigma_{I,mon})$. We next applied the optimization procedure to the monomer data sets taken at each temperature for all constructs. We thus determined optimized values of the parameters (i) – (iv) as a function of temperature and probe position, which are discussed in Chapters IV and V.

We performed joint optimizations on the D(Cy3)$_2$ dimer absorption and CD spectra. For each temperature, we used the optimized values of the monomer parameters (i) – (iii)

as inputs to the dimer calculations. From our convergence tests using the 15°C data, we concluded that occupation of at least six vibrational levels, in both the monomer ground and excited electronic-state manifolds, were needed to obtain converged simulations. Due to the perceived physical constraints of the duplex system we assumed the tilt angle to be zero and we thus determined the three remaining trial function parameters [(v), (vii), and (viii)] by minimizing the target function:

$$\chi^2_{tot,lin}(R_{AB}, \phi_{AB}, \sigma_{I,dim}) = \chi^2_{abs,dim}(R_{AB}, \phi_{AB}, \sigma_{I,dim}) + \chi^2_{CD,dim}(R_{AB}, \phi_{AB}, \sigma_{I,dim}) \quad (3.1)$$

Error bars associated with the optimized parameters were determined by a 1% deviation of the target function from its minimized value.

We compared optimizations using the Voigt profile, where the homogeneous width is given by Lorentzian function and the inhomogeneous width was modeled as a Gaussian, with a fit in which both the homogeneous and inhomogeneous broadening were represented by Gaussian functions. The optimized parameters were comparable for the two methods as shown in Figure 3.5. While the Gaussian fit more closely matched the tails of the spectra, the Voigt profile was chosen as the separation of the transitions within the low energy feature were distinguishable. Further discussion of the optimized parameters and the comparison between experimental and calculated results will be provided in the following chapters.

For constructs in which the inter-chromophore tilt could not be assumed to be zero the target function becomes

$$\chi^2_{tot,lin}(R_{AB}, \phi_{AB}, \delta_{AB}, \sigma_{I,dim}) = \chi^2_{abs,dim}(R_{AB}, \phi_{AB}, \delta_{AB}, \sigma_{I,dim}) + \chi^2_{CD,dim}(R_{AB}, \phi_{AB}, \delta_{AB}, \sigma_{I,dim}) \quad (3.2)$$

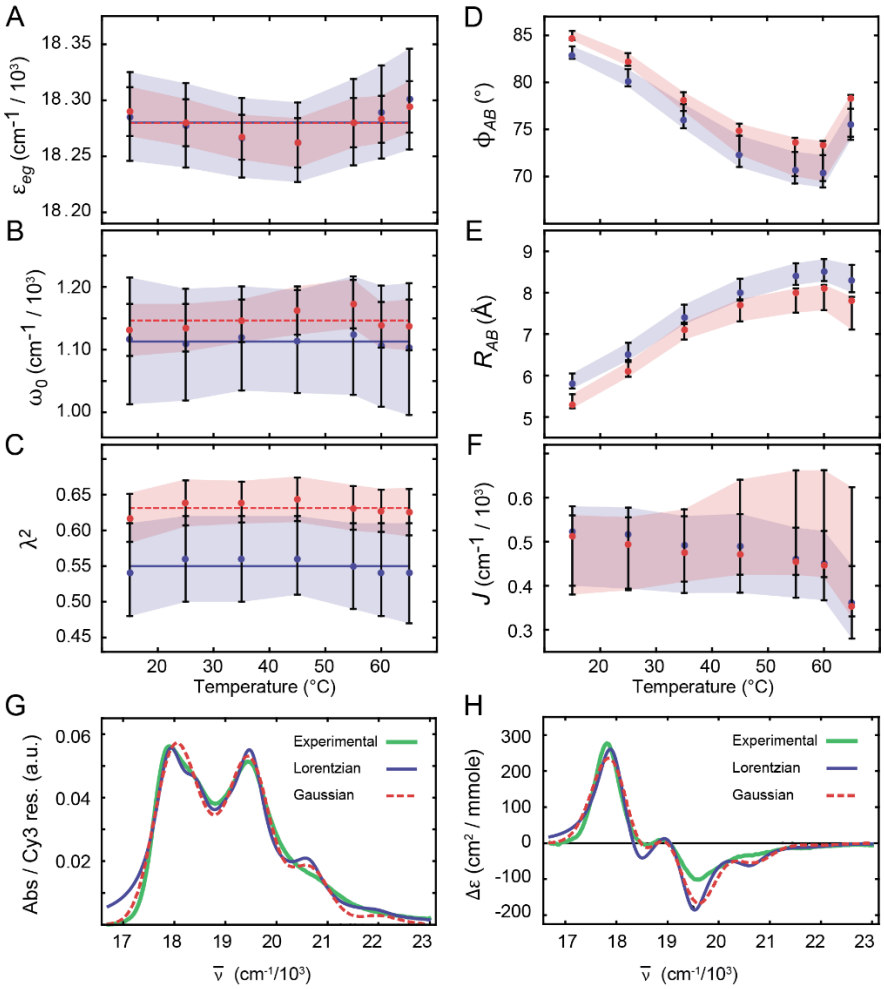

Figure 3.5: Comparison between optimized parameters based on the Lorentzian (blue) and Gaussian (red) models for the homogeneous lineshape. The intra-molecular parameters are **(A)** the electronic transition energy ε_{eg}, **(B)** the vibrational mode frequency ω_0, and **(C)** the Huang-Rhys electronic-vibrational coupling parameter λ^2. The inter-molecular conformational parameters are **(D)** the inter-chromophore twist angle ϕ_{AB}, **(E)** the inter-chromophore separation R_{AB}, and **(F)** the resonant coupling strength J, the inter-chromophore tilt angle δ_{AB} = 0°, and the inter-chromophore slip angle θ_{AB} = 0°. Error bars correspond to a 1% deviation of the target function from its minimum value. Comparison between experimental and simulated lineshapes for the absorption **(G)** and CD **(H)** spectra of the D(Cy3)$_2$ dimer DNA construct at 15°C.

Occasionally the computational optimizations would result in multiple configurations equally capable of reflecting the spectra, rather than a single optimal structural configuration. The error bars for these degenerate conformations were determined in two ways. First, by the range of the optimized parameter, then the 1% deviation of the target function was determined for the upper and lower extrema of the range. This is demonstrated in Figure 3.6.

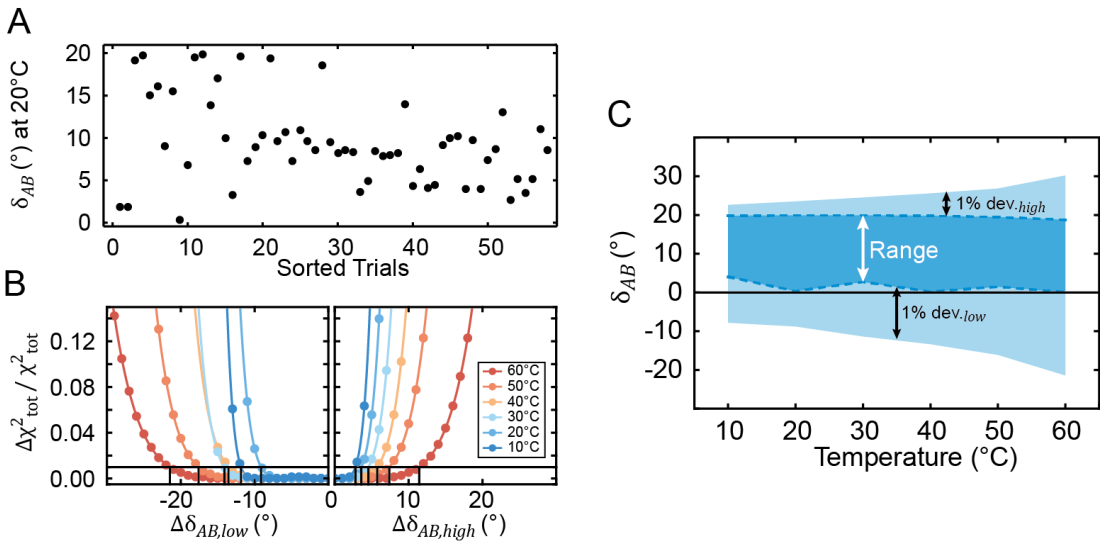

Figure 3.6: Determination of error bars for optimizations with degenerate conformations. **(A)** The structural parameter tilt angle output of the optimization is shown for a range of degenerate configurations (0-20°). **(B)** The relative deviation of the target function of temperatures used to determine the upper and lower error bars, which were taken from the lowest (left hand side) and the highest (right hand side) values of the structural parameters. **(C)** Composite error bar determination. The darker blue middle section indicates the range of possible degenerate values, and the lighter blue indicates the 1% deviation from the low or high end of that range.

When considering the 2DFS spectra in the optimization procedure, the real and imaginary rephasing and non-rephasing spectra were calculated according to Eqs 2.27-2.32 with corrections to account for the limited laser bandwidth given by Eqs. 2.35 and 2.36. The additional fit parameter Γ_{2D}, the relative quantum yield from doubly excited to

singly excited states was included. Furthermore, the parameter Γ_H became an optimized parameter rather than an input parameter. The target function for fitting the absorption, circular dichroism, and 2DFS spectra simultaneously is

$$\begin{aligned}\chi^2_{tot}(R_{AB}, \phi_{AB}, \delta_{AB}, \sigma_{I,dim}, \Gamma_H, \Gamma_{2D}) \\ = n\chi^2_{abs,dim}(R_{AB}, \phi_{AB}, \delta_{AB}, \sigma_{I,dim}) \\ + m\chi^2_{CD,dim}(R_{AB}, \phi_{AB}, \delta_{AB}, \sigma_{I,dim}) \\ + \chi^2_{2D,dim}(R_{AB}, \phi_{AB}, \delta_{AB}, \sigma_{I,dim}, \Gamma_H, \Gamma_{2D})\end{aligned} \tag{3.3}$$

where *n* and *m* are weighting factors used to make the contributions of $\chi^2_{abs,dim}$ and $\chi^2_{CD,dim}$ to the cost function the same order of magnitude to that of $\chi^2_{2D,dim}$.

In the calculation and optimization of the 2D spectra, a truncated form of the Hamiltonian was used. The eigenstates were determined by diagonalization of the Holstein Hamiltonian with six vibrational levels as determined from the absorption and circular dichroism measurements. However, the states accessible for the calculation of the 2D spectra were limited to the lower three vibrational levels. This reduced the computational cost of calculating the response functions as the Hamiltonian matrix goes as $4 \cdot n^2_{vib}$.

Summary and Bridge to Chapter IV

In this chapter, we described the experimental considerations used throughout this work including the complementary spectroscopic techniques used to study cyanine dyes labeled within DNA. The following chapters apply these techniques to determine the relative orientation of the cyanine dyes. In Chapter IV we will examine system in which the cyanine dyes Cy3 and Cy5 are located within the duplex region of DNA using absorption and circular dichroism.

CHAPTER IV

TEMPERATURE DEPENDENT CONFORMATIONS OF EXCITONICALLY COUPLED CYANINE DIMERS IN DOUBLE STRANDED DNA

Overview

This chapter presents studies of the conformations of the cyanine dyes, Cy3 and Cy5, when labeled within the duplex region of DNA fork constructs. We examined both dimers (referred to as $D(Cy3)_2$ and $D(Cy5)_2$ respectively) using temperature dependent absorption and circular dichroism (CD) experiments. The constrained nature of the duplex dimer system allowed us to assume physical constraints for the system, restricting the possible structural parameters. This section contains material that has been published as L. Kringle, N. P. D. Sawaya, J. Widom, C. Adams, M. G. Raymer, A. Aspuru-Guzik, and A. H. Marcus, "Temperature-dependent conformations of exciton-coupled Cy3 dimers in double-stranded DNA," *J. Chem. Phys*. **148**, 085101 (2018). In the excerpt used here, Sawaya developed the computational model, Widom, Adams, and I performed absorption and CD experiments, and I performed the two-dimensional fluorescence spectroscopy measurements and the computational optimizations. A. H. Marcus collaborated in conceiving and planning of the experiments, and the remaining co-authors provided editorial assistance.

Introduction

A long-standing problem in molecular spectroscopy is to understand the roles of nuclear vibrations in the electronic structure of interacting molecules.[1–13] Since the early

work of Förster, Kasha, Fulton and Gouterman,[2,14–16] it has been recognized that the absorption spectra of interacting molecules can appear strikingly different than that of the constituent monomers, particularly when the monomer spectrum exhibits a pronounced vibronic progression, which is due to the coupling between electronic and vibrational motion.[17–19] Such situations are important to the spectroscopic properties of molecular aggregates including biological and artificial light harvesting arrays.[7,13,20–22]

Time-resolved ultrafast experiments that probe the excited-state dynamics of photosynthetic antenna complexes suggest that quantum coherence might contribute to the energy transfer mechanism of these systems.[20–24] Recent studies show that spectroscopic signatures of quantum coherence can be understood by considering the role of vibrations; specifically, the presence of spatially delocalized electronic-vibrational states.[10–13,22,25] These and other experiments have stimulated new ideas for molecular design principles that utilize resonant intermolecular electronic (exciton) coupling in combination with intra-molecular electronic-vibrational (vibronic) coherences as a resource to achieve enhancements in energy transfer efficiency.[26,27] In order to test these principles experimentally, it is useful to develop molecular systems for which the exciton coupling strength can be varied while intramolecular parameters such as coupling between electronic and vibrational modes are maintained constant.

In the following work, we study the effects of varying exciton coupling strength on the vibronic transitions of a molecular dimer composed of two cyanine chromophores incorporated into the sugar-phosphate backbone of the double-stranded (ds) region of a DNA replication fork construct (see Figure. 1.1). Such fluorescently labeled DNA constructs may be used to study detailed mechanisms of protein-DNA interactions. Cy3

and Cy5 are commonly used fluorescent probes for biophysical studies of protein-DNA interactions,[28–35] which may be placed at site-specific positions within single-stranded (ss) DNA using phosphoramidite chemical insertion methods.[28,32] By annealing two complementary DNA strands, each labeled internally with a single cyanine chromophore, a DNA duplex can be formed with the resulting $D(Cy3)_2$ or $D(Cy5)_2$ dimer adopting a chiral conformation with approximately D_2 symmetry. The stability of the dimer depends on the strength of complementary hydrogen bonds between opposing nucleic acid base pairs, which can be adjusted by varying temperature and solvent conditions.[36] Previous absorption and circular dichroism (CD) studies of internally labeled cyanine dyes in dsDNA indicate that the local movements of the chromophores are restricted in the lowest energy, all trans, electronic ground state.[33,35] Furthermore, in typical aqueous solutions the spectroscopic lineshapes of these systems appear to be inhomogeneously broadened, which implies the existence of a wide range of local structural environments experienced by the fluorescent probes at any instant. The concept of DNA 'breathing' (i.e., local structural fluctuations)[36] allows for local disordered regions of the sugar-phosphate backbone to persist on time scales much longer than the excited state lifetime (< 1 ns).[28] Nevertheless, little is known about the conformations of such sub-states or the time scales of their inter-conversion.

We show that the temperature-dependent linear absorption and CD of the $D(Cy3)_2$ and $D(Cy5)_2$ dimer in dsDNA can be well characterized using the Holstein model,[37] which we apply to a model with two conformational parameters: the inter-chromophore separation R_{AB} and the twist angle ϕ_{AB}. The Holstein Hamiltonian describes each molecular site as a two-level electronic system coupled to a single harmonic

mode.[5,15,16,37,38] The presence of a resonant electronic interaction between the two molecular sites (characterized by the parameter J) leads to the formation of a manifold of excited states composed of delocalized symmetric and anti-symmetric superpositions of electronic-vibrational tensor product states. Such 'effective state models' have been well established to describe the electronic properties of molecular dimers in the strong and intermediate exciton-coupling regimes.[5,7,8,11,12,15,16,38] The combination of absorption and CD spectroscopy is particularly well suited to resolve these states since absorptive transitions to symmetric and anti-symmetric excited states are orthogonally polarized, and thus contribute to the CD spectrum with opposite sign.

Förster classified the interaction strength of an exciton-coupled molecular aggregate according to the degree of distortion exhibited by its absorption and photoluminescence spectra in comparison to those of the constituent monomers. He identified three different coupling regimes: strong, intermediate, and weak.[2] The strong coupling regime corresponds to a major redistribution of intensity between the various vibronic sub-bands of the aggregate absorption spectrum. In the intermediate coupling regime, the intensities of the vibronic bands of the aggregate are similar to those of the monomer, yet each vibronic feature is broadened due to these interactions. In the weak-coupling regime (often referred to as the Förster regime), the absorption spectrum of the coupled system is indistinguishable from that of a collection of uncoupled monomers. However, in a weakly coupled system, a local excitation may stochastically hop from one site to another.[2] In this work, we show that by adjusting the temperature over the range 15 – 60 °C, which spans the pre-melting regime of the $D(Cy3)_2$–dsDNA and $D(Cy5)_2$–dsDNA system, we may vary the *intermolecular* coupling strength J over the range 530 – 450 cm^{-1} while maintaining

intramolecular parameters approximately constant, such as the monomer transition energy ε_{eg}, the vibrational frequency ω_0, and the electron-vibrational coupling strength characterized by the Huang-Rhys parameter λ^2. In the following, we show that the structural parameters and degree of static disorder that characterizes the Hamiltonian of the system undergo systematic and physically meaningful changes as a function of temperature, which acts mainly to vary the inter-chromophore separation and twist angle through its destabilizing effects on local secondary structure of the DNA duplex. Because only the inter-chromophore properties of the D(Cy3)$_2$-dsDNA or D(Cy5)$_2$-dsDNA constructs are sensitive to temperature, the systems may be employed as useful experimental models to test fundamental concepts of protein-DNA interactions, and the role of electronic-vibrational coherence in electronic energy migration within exciton-coupled bio-molecular arrays.

Results

In this work we explored both internally labeled Cy3 and Cy5 DNA constructs, in which the sequence of the DNA remained constant, providing an examination of the structural packing of the two dyes in duplex DNA and intrinsic differences due to the intra-molecular properties of the dyes. The sequences and nomenclature of the internally labeled Cy3 or Cy5 constructs used in this work are shown in Table 3.1 of Chapter III. Because each chromophore is rigidly attached at two insertion site positions within the DNA single strands, the conformational space available to the cyanine dimer of the fully annealed DNA duplex is restricted. Therefore, in this work we specify the conformation by the interchromophore separation R_{AB} and twist angle ϕ_{AB}.

Absorption and CD Measurements

Absorbance and circular dichroism spectra were measured over a range of 200-700 nm to simultaneously examine the spectral region of the native bases (~275 nm) in addition to that of the Cy3 or Cy5 probe(s) (~540 nm and ~640 nm respectively). Spectra corresponding to the ultraviolet absorbance and CD of the nucleobases confirmed that the ds regions of the DNA constructs adopted the anticipated Watson-Crick right-handed B-form conformation,[39] and the absorption at 260 nm as a function of temperature was used to determine the melting temperature of 65°C for the DNA constructs, Figure. 4.1.

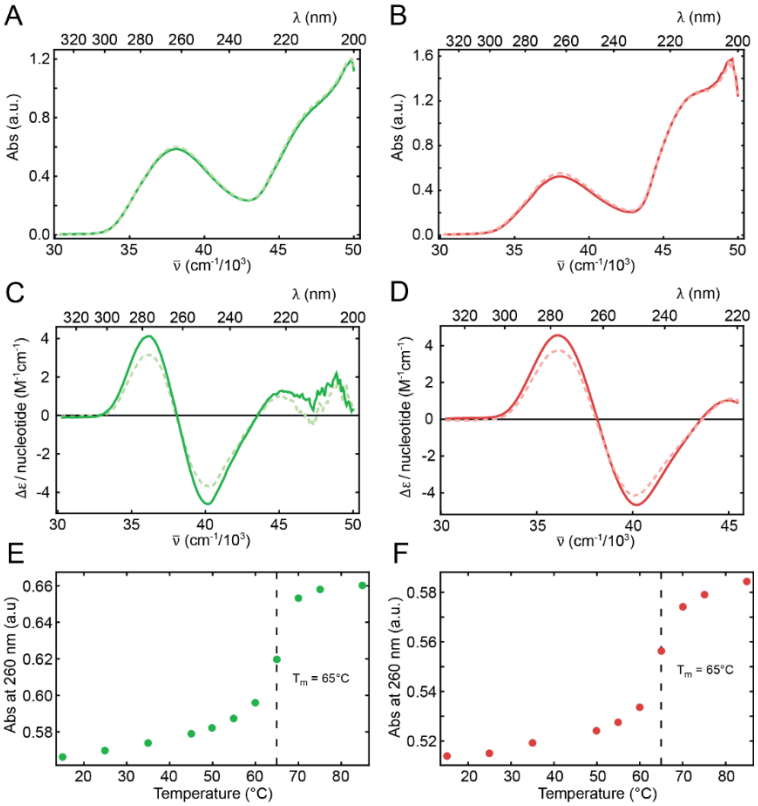

Figure 4.1: Absorption and CD spectra of the cyanine dye-DNA constructs over the nucleobase spectral range. Room temperature (25°C) **(A & B)** absorption and **(C & D)** CD of the **(A & C)** D(Cy3) monomer (dashed, light green) and D(Cy3)$_2$ dimer (solid green) and **(B & D)** D(Cy5) monomer (dashed, light red) and D(Cy5)$_2$ dimer (solid red). The spectra are shown as a function of wavenumber with the corresponding optical wavelength indicated on the top axis. **(E & F)** Absorption intensity as 260 nm as a function of temperature, showing the cooperative melting transition at T_m = 65°C for both the **(E)** D(Cy3)$_2$ dimer DNA construct and **(F)** D(Cy5)$_2$ dimer DNA construct.

Room temperature (25°C) absorption and CD spectra for the Cy3 and Cy5 monomer and dimer labeled DNA constructs are shown over the visible spectral range in Figure 4.2. The absorption spectrum of the D(Cy3) monomer DNA construct exhibits a progression of vibronic features with the first (0–0) peak centered at 549 nm (18,280 cm^{-1}). The vibronic progression is still present in the spectrum of the $D(Cy3)_2$ dimer DNA construct. However, individual vibronic features of the dimer are broadened relative to those of the monomer, and the ratio of the 0–0 to 1–0 vibronic peak intensities has decreased relative to that of the monomer [$I_{mon}^{(0-0)}/I_{mon}^{(1-0)}$ = 1.60]. While the monomer CD

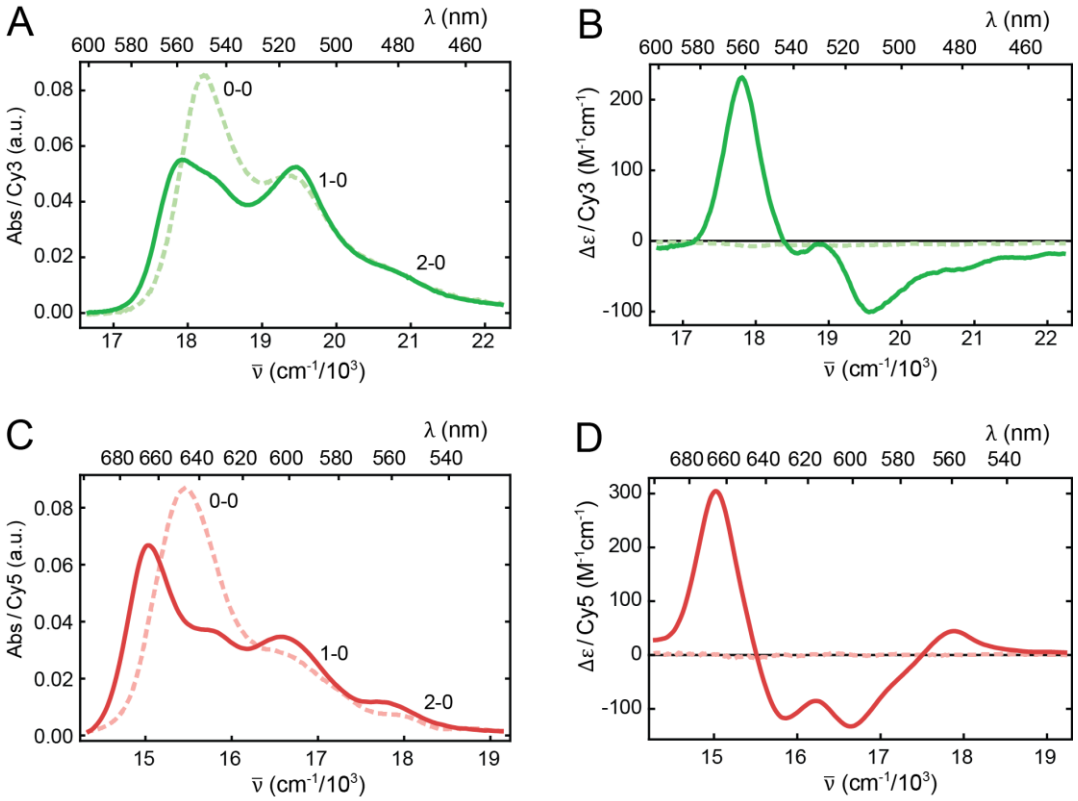

Figure 4.2: Absorption and CD spectra of the cyanine dye-DNA constructs. Room temperature (25°C) **(A & C)** absorption and (**B & D)** CD spectra for the **(A & B)** D(Cy3) monomer (dashed, light green) and $D(Cy3)_2$ dimer (solid green) and the **(C & D)** D(Cy5) monomer (dashed red) and $D(Cy5)_2$ dimer (solid red) labeled DNA constructs. Here Δε is the differential absorption of left and right circular polarized light. The spectra are shown as a function of wavenumber, with the corresponding optical wavelength displayed on the top axis. The vibronic features of the monomer absorption spectra are labeled n_e – 0, where n_e (= 0, 1, 2) indicates the vibrational occupancy of the electronically excited monomer.

signal is very weak (as expected), the dimer CD exhibits a progression of bisignate lineshapes (i.e. a change of sign within a given vibronic band), which is a signature of vibronic excitons in a chiral aggregate.[3,8,40] Likewise, the D(Cy5) monomer exhibits a vibronic progression with the 0-0 peak centered at 647 nm (15456 cm^{-1}). The ratio of the 0-0 to 1-0 vibronic peak intensities of the D(Cy5) monomer is nearly doubled relative to the D(Cy3) monomer [$I_{mon}^{(0-0)}/I_{mon}^{(1-0)}$ = 2.95]. The absorption spectrum of the $D(Cy5)_2$ dimer DNA construct exhibits a more pronounced splitting of the 0-0 feature with a greater intensity difference of those features. The CD exhibits a similar bisignate lineshape, with increased intensity of the negative transitions within the 1-0 feature relative to the $D(Cy3)_2$ dimer.

Temperature dependent measurements of the Cy3 and Cy5 DNA constructs were taken over a range of 15°C – 75°C. The monomer spectra of both D(Cy3) and D(Cy5) did not change with temperature beyond broadening of the features, the energies of the transitions and the relative intensities of the vibronic features did not change. However, the dimer spectra of the $D(Cy3)_2$ and $D(Cy5)_2$ DNA constructs did exhibit changes in the pre-DNA melting regime, indicating a local conformation change. The temperature dependent absorption and CD spectra of the $D(Cy3)_2$ and $D(Cy5)_2$ constructs are presented in Figure 4.3. The spectra behave similarly with increasing temperature. The low energy (0-0) feature of the absorbance decreases in intensity and blue shifts over a range of 15° - 55°C, while the higher energy (1-0) feature slightly increases in intensity. At the melting temperature (65°C) the 0-0 feature increases in intensity at the with the low energy feature now at the same energy as that of the monomer and above the melting temperature the absorbance mirrors that of the D(Cy3) or D(Cy5) monomer constructs. In the CD spectra, the features

decrease in intensity over the pre-melting regime, and is greatly reduced to the very weak signal seen for the monomer.

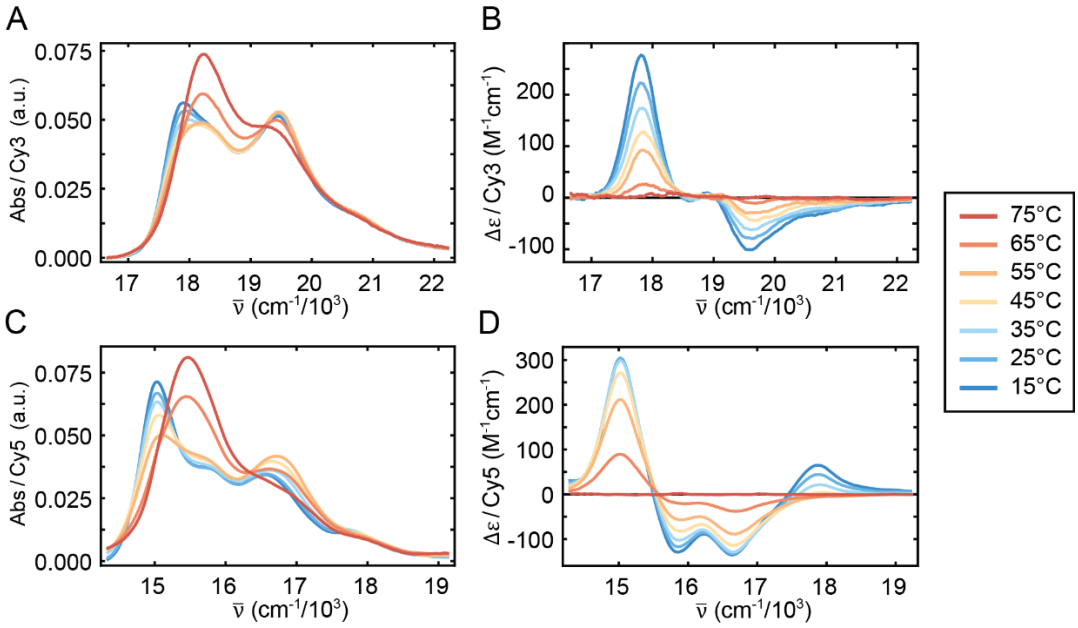

Figure 4.3: Temperature dependent absorption and CD of the cyanine dye-DNA constructs. **(A & C)** Absorption and **(B & D)** CD spectra of the **(A & B)** $D(Cy3)_2$ and **(C & D)** $D(Cy5)_2$ DNA constructs over the range of 15°C (blue) to 75° C (red) with increments of 10°C.

Estimation of the Homogeneous Linewidths

To obtain an estimate of the homogeneous line widths for the D(Cy3) monomer and $D(Cy3)_2$ dimer DNA constructs, we performed phase-modulated 2DFS experiments at room temperature. These measurements were carried out as previously described Chapter III. In Figure 4.4, we present 2DFS measurements of the D(Cy3) monomer and $D(Cy3)_2$ dimer labeled DNA samples at room temperature. For these measurements, we tuned the laser center wavelength across the low energy 0 – 0 and 1 – 0 sub-bands of the absorption spectra (515 – 550 nm). The rephasing 2DFS spectra exhibited quasi-elliptical 2D lineshapes, with representative examples shown in Figure 4.4. Rephasing 2DFS

measurements have the property that inhomogeneous line broadening does not contribute to the 2D spectrum along the anti-diagonal direction.[41] We thus determined the homogeneous line width from the anti-diagonal cross-sectional width. We compared fits of the diagonal and anti-diagonal cross-sections of the 2D spectra using both Lorentzian and Gaussian functions [see Figures 4.4 C, 4.4 D, 4.4 G and 4.4 H]. While the diagonal cross-sectional width of the 2D spectrum (FWHM, 505 cm^{-1}) closely matched that of the laser bandwidth (555 cm^{-1}), we found that the anti-diagonal cross-sectional width varied only slightly with laser center wavelength. We thus determined the average value of the Lorentzian FWHM Γ_H = 186 cm^{-1}, which corresponds to the total dephasing time $T_2 = (\pi c \Gamma_H)^{-1} \cong 57$ fs.

The total dephasing time is related to the population relaxation time (T_1) and the pure dephasing time (T_2') according to $(T_2)^{-1} = (2T_1)^{-1} + (T_2')^{-1}$.[42] For the Cy3 DNA constructs, the value of T_1 can be estimated using the room temperature fluorescence lifetime τ_f ~ 162 ps.[28] It is known that the fluorescence lifetime of Cy3 DNA constructs can vary with temperature due to the thermal activation of intramolecular photo-isomerization processes.[28,43–45] Nevertheless, such picosecond processes are orders of magnitude slower than those of pure dephasing, which dominate the homogeneous line width. As mentioned above, pure dephasing results from rapid fluctuations of the electronic transition energy due to interactions with the phonon bath. In proteins and disordered media, the pure dephasing time typically follows the relatively weak, power law temperature-dependence $T_2' \sim T^{1.3}$.[46,47] This suggests that the homogeneous line width is relatively insensitive to temperature. We therefore used the above determined value Γ_H = 186 cm^{-1} for our analyses of the linear absorption and CD spectra, as discussed below. In

addition, we assumed that the homogeneous lineshape of the Cy5 constructs would be similar in magnitude and therefore kept the value constant for both cyanine dye - DNA constructs.

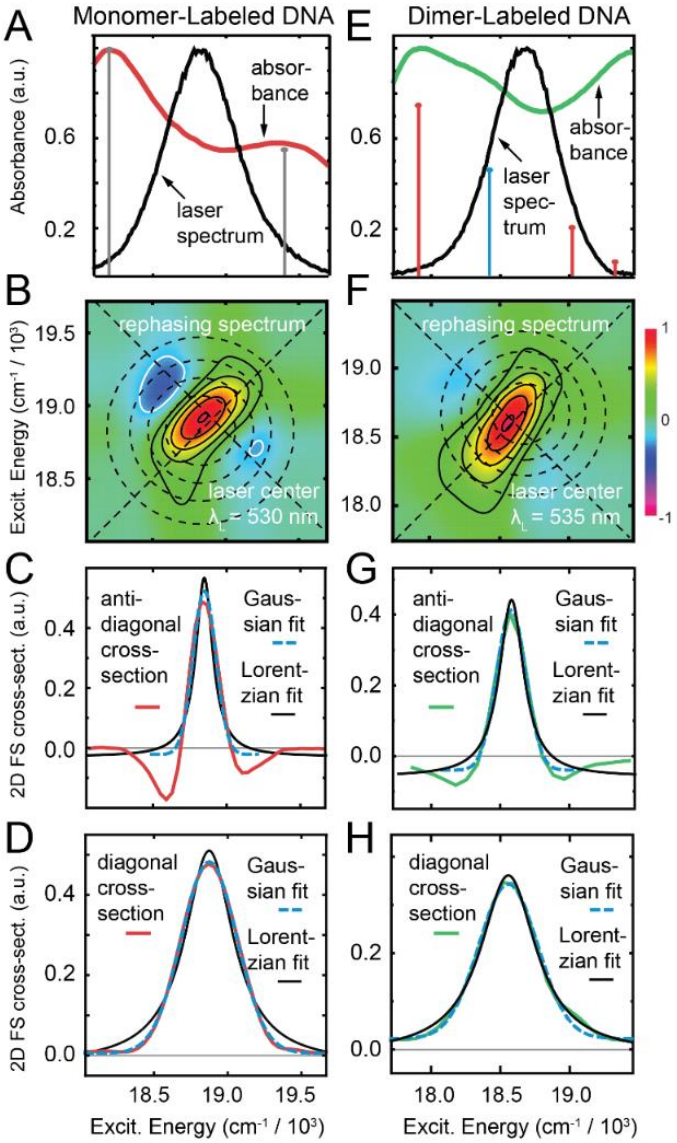

Figure 4.4: 2DFS rephasing spectra of the D(Cy3) monomer **(A - D)** and the D(Cy3)$_2$ dimer-labeled DNA constructs **(E - H)**. **(A & E)** Spectral overlap of the absorbance and laser excitation. **(B & F)** 2DFS rephasing spectra of the monomer and dimer construct. The concentric circles indicate the laser spectral overlap. The diagonal and anti-diagonal 2D cross-sections are marked with dashed lines. **(C & G)** Anti-diagonal lineshape of the monomer and dimer fit to Lorentzian and Gaussian functions, respectively. **(D & H)** Diagonal lineshape of the monomer and dimer fit to Lorentzian and Gaussian functions, respectively.

Conformational Determination Using the Holstein Hamiltonian

We studied the temperature-dependence of the absorption and CD spectra of both the monomer and dimer labeled cyanine dye DNA constructs. As described in the previous sections, we found that the monomer absorption spectrum did not vary significantly with temperature. This insensitivity with temperature is apparent when examining the values determined for the electronic transition energy, the effective vibrational mode, and the Huang-Rhys parameter, (see Figure 4.5, Table B.1, and B.2 of Appendix B). The mean values for the D(Cy3) monomer are $\bar{\varepsilon}_{eg} = 18{,}290$ cm^{-1}, $\bar{\omega}_0 = 1{,}105$ cm^{-1} $\overline{\lambda^2} = 0.55$, and the intra-molecular parameters for D(Cy5) are $\bar{\varepsilon}_{eg} = 15{,}501$ cm^{-1}, $\bar{\omega}_0 = 1{,}228$ cm^{-1} $\overline{\lambda^2} =$

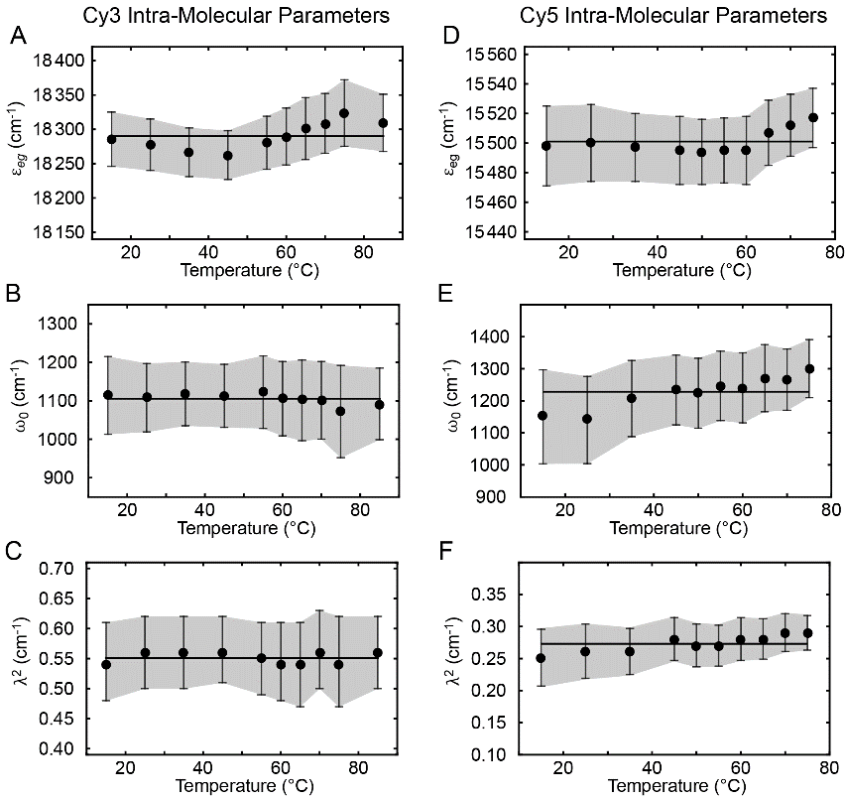

Figure 4.5: Temperature-dependent optimized intramolecular parameters from **(A - C)** D(Cy3) or **(D - F)** D(Cy5) monomer absorption. Error bars were calculated based on a 1% deviation of the target function from its optimized value. The dashed horizontal line indicates the mean value for each parameter. **(A & D)** electronic transition energy ε_{eg}; **(B & E)** the vibrational mode frequency ω_0; and **(C & F)** the Huang-Rhys electronic-vibrational coupling parameter λ^2.

0.27. The two constructs have similar effective vibrational modes, however the Huang-Rhys parameter of the D(Cy5)-dsDNA construct is approximately half that of the D(Cy3)-dsDNA construct as anticipated by the difference in relative intensities of the vibrational modes ($I_{mon}^{(0-0)}/I_{mon}^{(1-0)}$).[48]

Analysis of the D(Cy3)$_2$ Dimer DNA Construct

In Figure 4.6, we present absorption and CD spectra for the D(Cy3)$_2$ dimer at representative temperatures, overlaid with optimized simulations of the polarized symmetric $(+)$ and anti-symmetric $(-)$ components. The agreement between experiment and theory is very good over the full range of temperatures we investigated. In Table 4.1, we list as a function of temperature the output values of our optimization procedure, which include the resonant coupling strength J, the inter-chromophore twist angle ϕ_{AB}, the inter-chromophore separation R_{AB}, and the spectral inhomogeneity parameter $\sigma_{I,dim}$. For temperatures above the melting transition (at 65°C), the absorption spectrum of the dimer became indistinguishable from that of the monomer DNA construct, signifying the complete separation between the conjugated single DNA strands.

We first consider the absorption and CD spectrum of the D(Cy3)$_2$ dimer DNA construct at 15°C, which is the lowest temperature we investigated. We obtained optimized values for the structural parameters J = 529 cm^{-1}, ϕ_{AB} = 82.9°, R_{AB} = 5.8 Å, and $\sigma_{I,dim}$ = 292 cm^{-1}. The values for R_{AB} and ϕ_{AB} are consistent with the local conformation of the D(Cy3)$_2$ dimer depicted in Figure A.1, which shows the two Cy3 monomers positioned closely within the DNA duplex with nearly orthogonal relative orientation. The magnitude of the resonant coupling strength J is greater than the spectral inhomogeneity $\sigma_{I,dim}$ of the

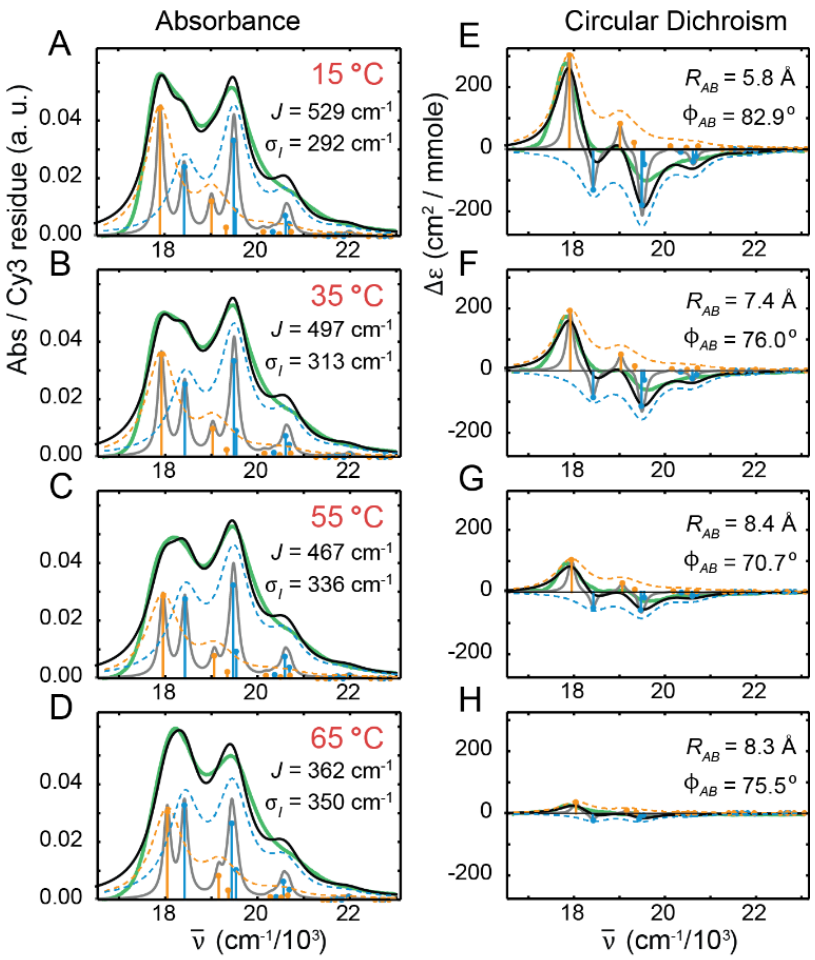

Figure 4.6: Comparison between experiment and calculated spectra of the D(Cy3)$_2$ dimer labeled DNA at representative temperatures. **(A - D)** absorption and **(E - H)** CD spectra for D(Cy3)$_2$ dimer labeled DNA constructs. Experimental spectra are shown in solid green, the model homogeneous lineshapes in solid gray, and the model total lineshapes (inhomogeneous-plus-homogeneous) in solid black. Symmetric and anti-symmetric transitions determined from the model are shown as blue and orange sticks, respectively. Symmetric and anti-symmetric contributions to the inhomogeneous lineshapes are shown as dashed blue and orange curves, respectively.

system, which is a necessary condition for the dimer to support delocalized excitons. Furthermore, because the coupling strength is comparable to the intramolecular vibrational relaxation energy (i.e. $J \sim \lambda^2 \hbar\omega_0$ = 602 cm^{-1}, where we have used λ^2 = 0.54 and $\hbar\omega_0$ = 1,116 cm^{-1}) the dimer must exist in the intermediate-to-strong exciton-coupling regime.

From these observations, we conclude that at 15 °C, the perturbation theory description of the exciton band structure [summarized by Eqs. (2.14) – (2.16a)] should not strictly hold.

Table 4.1. Optimized values of the structural parameters of the $D(Cy3)_2$ dimer DNA construct at various temperatures, obtained from the Holstein model fit to absorption and circular dichroism spectra. These calculations used the values we determined for the electric transition dipole moment (EDTM) $\left|\mu_{eg}^{0}\right|$ = 12.8 D, and for each temperature, the electronic transition energy ε_{eg}, the vibrational mode frequency ω_0, and the Huang-Rhys parameter λ^2 obtained from our analyses of the absorption spectra of the Cy3 monomer DNA construct (see Table B.1 of Appendix B). The parameters listed are the resonant coupling strength J, the inter-chromophore twist angle ϕ_{AB}, the inter-chromophore distance R_{AB}, and the standard deviation of the Gaussian inhomogeneous disorder function $\sigma_{I,dim}$. Structural parameters are presented at temperatures below the melting transition at 65 °C, for which the dimer model may reasonably be applied. Error bars were calculated based on a 1% deviation of the target function from its optimized value.

T (°C)	J (cm^{-1})	ϕ_{AB} (°)	R_{AB} (Å)	$\sigma_{I,dim}$ (cm^{-1})
15	529 +51/−129	82.9 +0.9/−0.4	5.8 +0.3/−0.1	292 +24/−6
25	514 +63/−120	80.1 +1.3/−0.5	6.5 +0.3/−0.1	302 +23/−6
35	497 +61/−114	76.0 +1.7/−0.8	7.4 +0.3/−0.2	313 +20/−7
45	483 +80/−99	72.3 +2.0/−1.3	8.0 +0.3/−0.2	325 +18/−8
55	467 +64/−94	70.7 +1.9/−1.4	8.4 +0.3/−0.2	336 +15/−9
60	449 +75/−82	70.4 +1.9/−1.6	8.5 +0.3/−0.2	345 +14/−10
65	362 +83/−82	75.5 +1.7/−1.6	8.3 +0.4/−0.3	350 +13/−12

From our simulated model fits to the absorption and CD spectra, we determined the experimental Davydov splitting of the 0 – 0 vibronic band. We define the Davydov splitting for the 0 – 0 band as the energy difference between the single upper energy (symmetric, +) exciton and the single lower energy (anti-symmetric, –) exciton within this band. Our analysis of the 15°C spectra reveal a pronounced splitting (DS_{0-0} = 532 cm^{-1}), with the lower energy anti-symmetric exciton exhibiting greater intensity than that of the upper energy symmetric exciton (see Figures 4.6 A and 4.6 E). We note that the pronounced bisignate splittings of individual vibronic bands of the CD spectrum can be understood

from the opposite sign contributions of the symmetric and anti-symmetric excitons [see Eqs. (2.12) and (2.13)].[8] This condition follows from the chiral D_2 symmetry of the coupled dimer, which leads to significant oscillator strength contributions from both symmetric and anti-symmetric excitons.

We determined the Davydov splitting of the 1–0 vibronic band (DS_{1-0} = 327 cm^{-1}) by considering only single-particle exciton contributions, which are expected to dominate the absorption and CD spectra in the limit of weak exciton coupling. In this limit, one upper energy symmetric state and one lower energy anti-symmetric state are much larger in magnitude than the remaining states within 1–0 vibronic band. This appears to be valid for the 15 °C sample, as well as for samples at higher temperatures (see below). We note that the above values for DS_{0-0} and DS_{1-0} are similar in magnitude to the theoretical prediction (616 cm^{-1} and 333 cm^{-1}, respectively) given by the factor $2Je^{-\lambda^2}\lambda^{2v_t}/v_t!$. Based on the simulated spectra, we determined the ratios of the vibronic band intensities $I_+^{(0-0)}/I_+^{(1-0)}$ = 0.62 for the symmetric exciton, and $I_-^{(0-0)}/I_-^{(1-0)}$ = 2.60 for the anti-symmetric exciton. We found that the symmetric (anti-symmetric) band intensity ratio decreased (increased) in the coupled dimer relative to that of the free monomer [$I_{mon}^{(0-0)}/I_{mon}^{(1-0)}$ = 1.60], as suggested by the perturbation theory.[8] However, these values are considerably smaller in magnitude than those predicted (0.84 and 4.31) by Eq. 2.16a. These findings further support that at 15 °C, the system resides in the intermediate-to-strong exciton-coupling regime. While structural disorder is significant, it does not mask the effects of the intermediate-to-strong exciton delocalization.

As the temperature was increased over the range 15 – 65 °C, the effects of exciton coupling on the D(Cy3)$_2$ dimer absorption and CD spectra became less pronounced (see

Figure 4.3). The Davydov splitting for both the 0–0 and 1–0 vibronic bands decreased continuously, as did the finite amplitudes of the CD signal. We note that the agreement between experimental and theoretical values of DS_{0-0} and DS_{1-0} is good over the full range of temperatures (see Table B.3). Moreover, the vibronic band intensity ratio $I_{+(-)}^{(0-0)}/I_{+(-)}^{(1-0)}$ of the symmetric (anti-symmetric) exciton appeared to increase (decrease) with increasing temperature. Comparison between experimental and theoretical values for $I_{+(-)}^{(0-0)}/I_{+(-)}^{(1-0)}$ (see Table B.5) appears to become more favorable at elevated temperatures, consistent with the system undergoing a transition to the weak exciton-coupling regime.

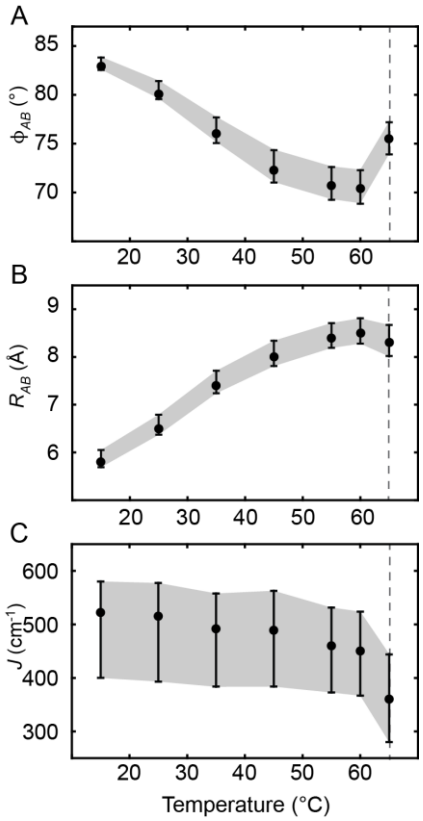

Figure 4.7: Temperature-dependent optimized parameters structural from $D(Cy3)_2$ dimer absorption and CD spectra. Error bars were calculated based on a 1% deviation of the target function from its optimized value. The dashed gray line at 65°C indicates the melting transition temperature T_m of the DNA constructs. **(A)** Inter-chromophore twist angle; **(B)** Inter-chromophore separation; and **(C)** Resonant electronic coupling parameter.

We see that the temperature-dependent properties of the D(Cy3)$_2$ dimer DNA construct are correlated to a systematic change in the resonant coupling strength J between the Cy3 monomer subunits. This is due to the temperature sensitivity of cooperative interactions between constituent nucleobases (e.g. base stacking interactions, Watson-Crick hydrogen bonding, etc.), which stabilize the right-handed helical structure of the DNA duplex. The temperature-dependent disruption of local DNA secondary structure is reflected by systematic changes in the conformation of the D(Cy3)$_2$ dimer, which is characterized by the structural parameters listed in Table 4.1 and plotted in Figure 4.7.

As shown in Figure 4.7, the structural parameters of the D(Cy3)$_2$ dimer vary continuously over the range of temperatures 15 – 60 °C. The inter-chromophore separation R_{AB} increases from 5.8 – 8.5 Å, the inter-chromophore twist angle ϕ_{AB} decreases from 82.9 – 70.4°, the resonant coupling J decreases from 529 – 449 cm^{-1}, and the spectral inhomogeneity parameter $\sigma_{I,dim}$ increases from 292 to 345 cm^{-1}, Table 4.1 The spectral inhomogeneity is a measure of the disorder of the local DNA environment experienced by the chromophores. In Figure 4.8, we compare the spectral inhomogeneity for both the D(Cy3) monomer and D(Cy3)$_2$ dimer DNA constructs as a function of temperature. The values of both the parameters $\sigma_{I,mon}$ and $\sigma_{I,dim}$ increase with temperature, which suggests the presence in both species of a broad distribution of thermally populated sub-states. It is interesting that the level of static disorder appears to be greater in the Cy3 monomer DNA construct in comparison to that of the D(Cy3)$_2$ dimer construct. This is likely a reflection of the less favorable packing conditions of the D(Cy3) monomer DNA construct, for which a single thymine base is positioned across form the Cy3 chromophore on the opposing DNA single-strand.

The DNA construct undergoes a denaturation, or 'melting' transition at 65 °C, as evidenced by an increased optical absorption of the nucleobases at 260 nm (see Figure 4.1). Immediately below the melting transition at 65 °C, the absorption spectrum develops an abrupt increase in the intensity of the 0–0 vibronic band and a concomitant decrease in the intensity of the 1–0 band, resulting in a spectrum nearly identical to that of the monomer DNA construct (compare Figure 4.6 A to 4.6 D). Thus, when the DNA strands dissociate at the melting transition, the electronic properties become those of the isolated monomers due to the complete disruption of the resonant coupling. At temperatures near and above 65 °C, the Holstein dimer model cannot accurately represent the electronic properties of the system because the electronic interaction is disrupted by the DNA strand separation. This leads to increased error associated with the optimized conformational parameters above 65 °C.

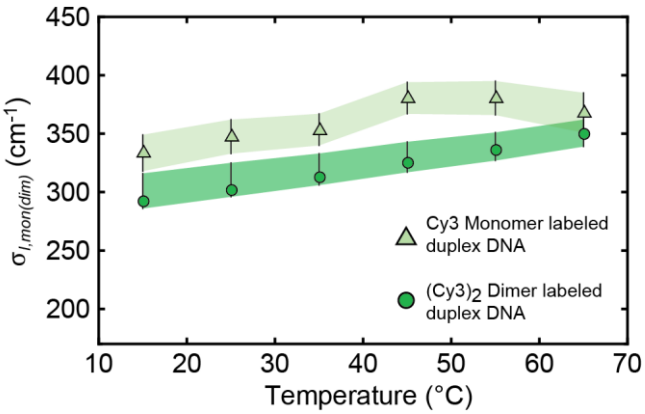

Figure 4.8: Comparison of the standard deviation of the inhomogeneous broadening Gaussian function for the D(Cy3) monomer (light green triangles) and $D(Cy3)_2$ dimer (green circles). Error bars are calculated from a 1% deviation of the target function.

Analysis of the $D(Cy5)_2$ Dimer DNA Construct

In Figure 4.9 we present the absorption and CD spectra for the $D(Cy5)_2$ dimer at the same representative temperatures as shown for the $D(Cy3)_2$ dimer construct in Figure

4.6, again overlaid with optimized simulations of the polarized symmetric (+) and anti-symmetric (−) components. The list of output values of the optimization procedure as a function of temperature for the D(Cy5)$_2$ dimer is presented in Table 4.2.

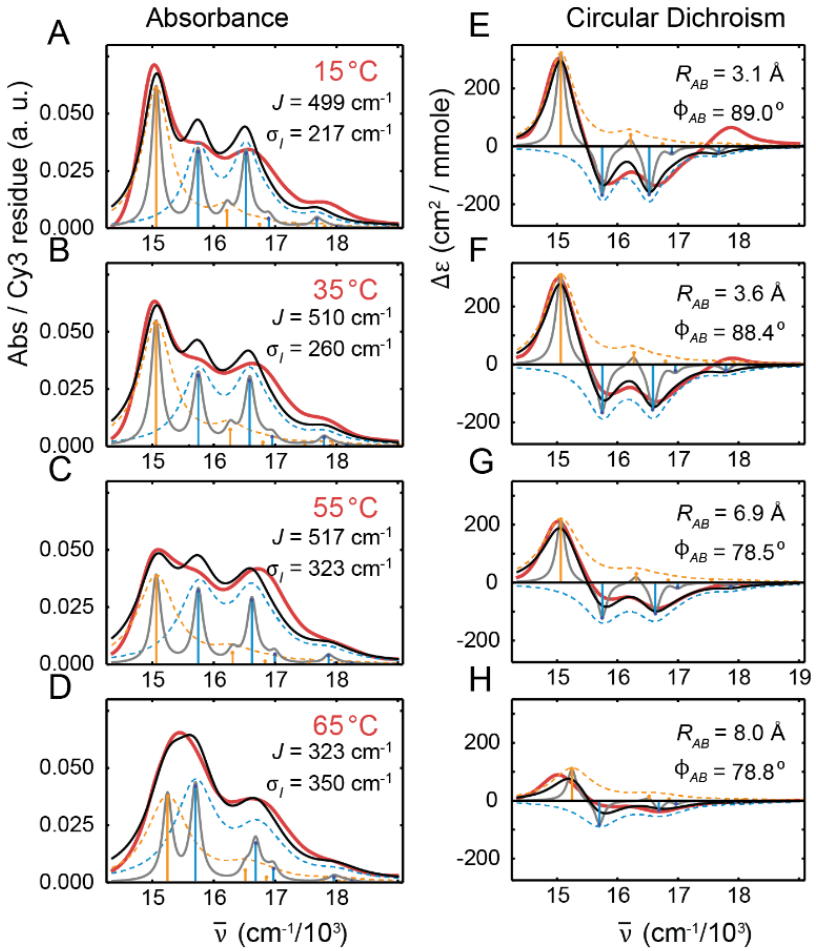

Figure 4.9: Comparison between experiment and calculated spectra of the D(Cy5)$_2$ dimer labeled DNA at representative temperatures. **(A-D)** absorption and **(E-H)** CD spectra for D(Cy5)$_2$ dimer labeled DNA constructs. Experimental spectra are shown in solid red, the model homogeneous lineshapes in solid gray, and the model total lineshapes (inhomogeneous-plus-homogeneous) in solid black. Symmetric and anti-symmetric transitions determined from the model are shown as blue and orange sticks, respectively. Symmetric and anti-symmetric contributions to the inhomogeneous lineshapes are shown as dashed blue and orange curves, respectively.

Upon examination of the D(Cy5)$_2$ construct at 15°C, We obtained optimized values for the structural parameters of the D(Cy5)$_2$ construct at 15°C, J = 499 cm^{-1}, ϕ_{AB} = 89.0°,

R_{AB} = 3.1 Å, and $\sigma_{I,dim}$ = 217 cm^{-1}. The magnitude of the resonant coupling is, again, greater than the spectral inhomogeneity $\sigma_{I,dim}$, and the coupling strength is comparable to the intramolecular vibrational relaxation energy, indicating the D(Cy5)$_2$ dimer also exists

in the intermediate-to-strong exciton coupling regime ($J \gtrsim \lambda^2\hbar\omega_0$ = 335 cm^{-1}, where we

have used λ^2 = 0.25 and $\hbar\omega_0$ = 1,153 cm^{-1}).

We found the experimental Davydov splittings of the D(Cy5)$_2$ dimer were even more pronounced at 15°C relative to D(Cy3)$_2$ (DS_{0-0} = 682 cm^{-1} and DS_{1-0} = 308 cm^{-1}). These values are similar in magnitude to the theoretical prediction determined from the factor $2Je^{-\lambda^2}\lambda^{2v_t}/v_t!$ (777 cm^{-1} and 193 cm^{-1}, respectively). From the simulated spectra, we determined the ratios of the vibronic band intensities $I_+^{(0-0)}/I_+^{(1-0)}$ = 0.98 for the

Table 4.2. Optimized values of the structural parameters of the D(Cy5)$_2$ dimer DNA construct at various temperatures, obtained from the Holstein model fit to absorption and circular dichroism spectra. These calculations used the values we determined for the electric transition dipole moment (EDTM) $|\mu_{eg}^0|$ = 13.0 D, and for each temperature, the electronic transition energy ε_{eg}, the vibrational mode frequency ω_0, and the Huang-Rhys parameter λ^2 obtained from our analyses of the absorption spectra of the Cy5 monomer DNA construct (see Table B.2. of Appendix B). The parameters listed are the resonant coupling strength J, the inter-chromophore twist angle ϕ_{AB}, the inter-chromophore distance R_{AB}, and the standard deviation of the Gaussian inhomogeneous disorder function $\sigma_{I,dim}$. Structural parameters are presented at temperatures below the melting transition at 65°C, for which the dimer model may reasonably be applied. Error bars were calculated based on a 1% deviation of the target function from its optimized value.

T (°C)	J (cm^{-1})	ϕ_{AB} (°)	R_{AB} (Å)	$\sigma_{I,dim}$ (cm^{-1})
15	499 +93/−41	89.0 +0.04/−0.09	3.1 +0.04/−0.1	217 +9/−11
25	538 +92/−43	88.7 +0.05/−0.1	3.3 +0.05/−0.1	234 +9/−9
35	510 +87/−34	88.4 +0.05/−0.1	3.6 +0.04/−0.1	260 +8/−9
45	537 +92/−38	86.0 +0.1/−0.3	4.8 +0.06/−0.1	294 +9/−9
55	517 +105/−49	78.5 +0.6/−1.1	6.9 +0.1/−0.2	323 +12/−11
65	323 +94/−105	78.8 +3.2/−1.5	8.0 +0.2/−0.3	350 +10/−8

symmetric exciton, and $I_{-}^{(0-0)}/I_{-}^{(1-0)}$ = 5.50 for the anti-symmetric exciton. As was seen in the examination of Cy3, we found that the symmetric (anti-symmetric) band intensity ratio decreased (increased) in the coupled D(Cy5)$_2$ dimer relative to that of the free monomer [$I_{mon}^{(0-0)}/I_{mon}^{(1-0)}$ = 2.95], as suggested by the perturbation theory.[8] However, these values are considerably smaller in magnitude than those predicted (1.90 and 10.53) by Eq. 2.16b.

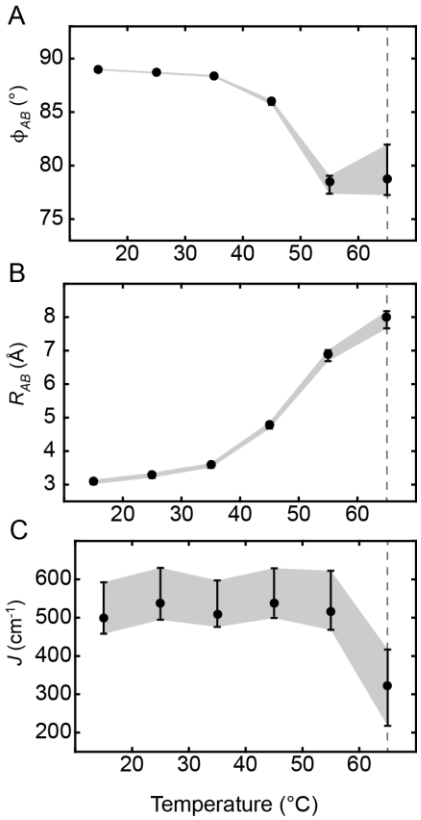

Figure 4.10: Temperature-dependent optimized structural parameters from D(Cy5)$_2$ dimer absorption and CD spectra. Error bars were calculated based on a 1% deviation of the target function from its optimized value. The dashed gray line at 65°C indicates the melting transition temperature T_m of the DNA constructs. **(A)** Inter-chromophore twist angle; **(B)** Inter-chromophore separation; and **(C)** Resonant electronic coupling parameter.

The temperature dependence of the D(Cy5)$_2$ dimer exhibited similar properties to that of the D(Cy3)$_2$ dimer. The exciton coupling of the dimer absorption and CD spectra

became less pronounced (see Figure 4.3), the Davydov splitting decreased (see Table B.4), and the vibronic band intensity ratio $I_{+(-)}^{(0-0)}/I_{+(-)}^{(1-0)}$ of the symmetric (anti-symmetric) exciton appeared to increase (decrease) (see Table B.6). The structural parameters of the $D(Cy5)_2$ dimer vary over the 15 – 65°C range are plotted in Figure 4.10 and presented in Table 4.2. The inter-chromophore separation R_{AB} increases from 3.1 – 8.0 Å, the inter-chromophore twist angle ϕ_{AB} decreases from 89.0 – 78.8°, the resonant coupling J decreases from 499 - 323 cm^{-1}.

The spectral inhomogeneity of the $D(Cy5)_2$ dimer construct increased from 217 – 350 cm^{-1}, in Figure 4.11 we compare the spectral inhomogeneity for both the D(Cy5) monomer and $D(Cy5)_2$ dimer DNA constructs as a function of temperature. As was seen in the Cy3 constructs, the D(Cy5) monomer DNA construct exhibits a level of static disorder greater than that of the dimer. Additionally, the $D(Cy5)_2$ dimer construct appears to have less static disorder than that of the $D(Cy3)_2$ dimer at low temperature, then undergoes a greater relative increase with temperature such that the two dimer constructs exhibit approximately equal levels of spectral inhomogeneity at 65°C. This suggests that

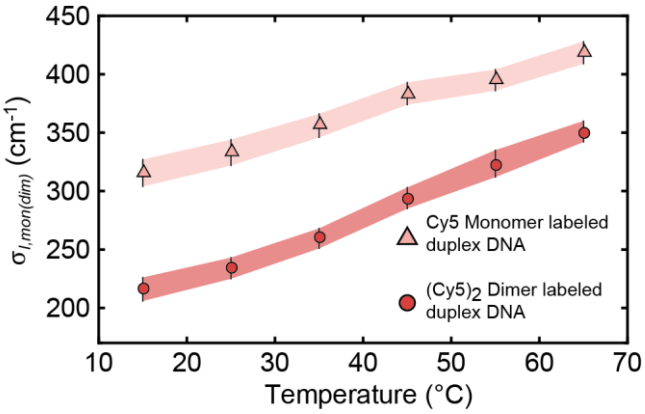

Figure 4.11: Comparison of the standard deviation of the inhomogeneous broadening Gaussian function for the D(Cy3) monomer (light red triangles) and $D(Cy3)_2$ dimer (red circles). Error bars are calculated from a 1% deviation of the target function.

the larger Cy5 chromophores have a more favorable packing condition than the Cy3 chromophores, which is disrupted by the elevation of temperature.

Conclusions

In this work, we studied the absorption and CD spectra of a $D(Cy3)_2$ and $D(Cy5)_2$ dimer, which was rigidly positioned within the sugar-phosphate backbone of double-stranded DNA. We applied an essential-state Holstein model to characterize the temperature-dependent excitons supported by the dimer, for which the electronic and vibrational states of the isolated monomers are internally coupled. At the lowest temperature we studied (15°C), the system exhibited intermediate-to-strong resonant coupling (J ~ 500 cm^{-1} for both the Cy3 or Cy5 constructs), comparable in magnitude or greater than the vibrational relaxation energy of the constituent monomers ($\lambda^2\hbar\omega_0$ ~ 600 cm^{-1} or ~ 335 cm^{-1} for the Cy3 and Cy5 constructs respectively). Under these conditions, the dimer can support delocalized excitons composed of symmetric and anti-symmetric superpositions of electronic-vibrational product states. This electronic structure is a consequence of the co-facial geometry of the cyanine dimers with inter-chromophore twist angle ϕ_{AB} ~ 80°- 85° and inter-chromophore separation R_{AB} ~ 3 - 6 Å.

The structural parameters of the $D(Cy3)_2$ and $D(Cy5)_2$ exhibited similar trends, in that the dyes were positioned close together, within the duplex of the DNA and at a nearly orthogonal orientation. However, the D(Cy5) monomer construct exhibits less electronic-vibrational coupling, as evidenced by the optimized Huang-Rhys parameter. Therefore, creating a larger difference between the vibrational relaxation energy and the excitonic coupling in the case of the $D(Cy5)_2$ dimer, although the excitonic coupling of the two dimer

constructs are similar in magnitude. This would suggest that the $D(Cy5)_2$ construct could better support delocalized excitons.

As the temperature was increased towards the ds – ss DNA melting temperature (T_m = 65 °C), the resonant coupling strength gradually decreased over an ~ 80 cm^{-1} range, while the Hamiltonian parameters characteristic of the monomer (i.e. the transition energy ε_{eg}, the Huang-Rhys electronic-vibrational coupling parameter λ^2, and the vibrational frequency ω_0) remained approximately independent of temperature. This is a consequence of the sensitivity of the local secondary structure of the dsDNA to temperature, which affects the inter-chromophore separation and twist angle, but not the electronic-vibrational properties internal to each monomer. Our accompanying 2DFS measurements allowed us to estimate the spectral homogeneous line width, which was approximately the same for both the D(Cy3) monomer and $D(Cy3)_2$ dimer (FWHM Γ_H = 186 cm^{-1}, corresponding to coherence time $\tau_c = (\pi c \Gamma_H)^{-1} \cong 57$ fs). The spectral inhomogeneity parameters of the monomer and dimer (given by the standard deviations $\sigma_{I,mon}$ and $\sigma_{I,dim}$, respectively) exhibited a systematic increase with temperature, signifying that the probe chromophores experience locally disordered, thermally activated regions of the DNA duplex, well below the melting transition. While the magnitude of spectral inhomogeneity is significant across the 15 – 65°C temperature range (220 – 350 cm^{-1}), the effects of exciton delocalization within the dimer are not dominated by the spectral inhomogeneity.

Although the Holstein model for the exciton-coupled $D(Cy3)_2$ or $D(Cy5)_2$ dimer is relatively simple as it assumes a single internal vibrational mode for each monomer, the model appears to capture the essential features of the experimental absorption and CD spectra of both dimer constructs over the full range of temperatures we investigated. The

success of the Holstein model may be due in large part to the presence of an intense Raman-active vibration at ~ 1,200 cm^{-1}, which is attributed primarily to symmetric stretching of the polymethine bridge of the chromophore.[49] Previous work by others have examined similar systems, such as dsDNA supported $(Cy5)_2$ dimers,[50] and $(Cy3)_2$ dimers attached to DNA using flexible linkers.[51] However, those studies did not account for the influence of the vibrational states of the cyanine chromophores, which led to claims of solely J-type and H-type dimer conformations, respectively. On the other hand, a similar Holstein model was previously used to describe a synthetically derived $(Cy3)_2$ dimer, which was rigidly held to a single achiral conformation (i.e., a racemic mixture) using covalent aliphatic groups.[11,12] While the intramolecular parameters and transition dipole moment for that system were roughly the same as those we found for the $D(Cy3)_2$ DNA dimer of the current work, the electronic properties of the synthetic $(Cy3)_2$ dimer are notably different. The intermolecular structural parameters ϕ_{AB} = 18° and R_{AB} = 10 Å correspond to a significantly stronger resonant coupling strength J = 820 cm^{-1} than the value we obtained for the most structured $D(Cy3)_2$ DNA conformation at 15 °C, and the electronic properties are dominated by the H-type (symmetric) exciton. It is a consequence of the relatively large inter-chromophore twist angle ϕ_{AB} = 83° of the D_2 symmetric chiral conformation of the $D(Cy3)_2$ DNA system that both H- (symmetric) and J- (anti-symmetric) type exciton components contribute significantly to the absorption and CD spectra.

For the $D(Cy3)_2$ and $D(Cy5)_2$ DNA systems, temperature variation allows the resonant coupling strength to be 'tuned' across the intermediate-to-strong exciton-coupling regime, while the Hamiltonian parameters characterizing the internal properties of the D(Cy3) or D(Cy5) monomers are approximately constant. Moreover, spectral

inhomogeneity (i.e. local site-energy disorder) is significant in this system, and is likely due to the presence of local structural fluctuations of the DNA backbone and base stacking that influence the packing of the chromophore probes, packing that led to similar configurations for both dimer constructs. Such local fluctuations of DNA are termed DNA 'breathing,' and are thought to be significant to molecular biological processes such as protein-DNA binding and protein function.[36] The above properties of the $D(Cy3)_2$ and $D(Cy5)_2$ dimer DNA construct suggest that it may be employed as a useful model system to test fundamental concepts of protein-DNA interactions, and the role of electronic-vibrational coherence in electronic energy migration within exciton-coupled bio-molecular arrays.

Summary Bridge to Chapter V

In this chapter, we examined cyanine dyes labeled within the duplex region of DNA, where the chromophores were rigidly held such that the inter-chromophore tilt angle and inter-chromophore slip angle could be assumed to be zero. However, different cyanine dye DNA constructs in which the dye is placed at locations with greater flexibility, such as fork template junctions invalidate this assumption. In Chapter V, we will explore the additional conformational parameters when considering Cy3-DNA constructs in which the location of the dimer probes is varied relative to the DNA fork junction.

CHAPTER V

EXAMINATON OF THE LOCAL STRUCTURE OF DNA FORK JUNCTIONS USING CY3 DIMERS

Overview

In this work, we examined the conformations cyanine dimers adopted at the single-strand/double-strand DNA fork junction using absorption, circular dichroism, and two-dimensional fluorescence spectroscopy. The fork junction has increased flexibility relative to the duplex, which was examined in the previous chapter, therefore three structural parameters (inter-chromophore twist, tilt and separation) were used in the conformational determination presented here. This section contains co-authored work. Absorption and circular dichroism measurements were performed by D. Jose, J. Widom, and I. Two-dimensional data was collected by D. Heussman and A. Tamimi. Model optimizations of the monomer were done by R. Keller under my supervision and I performed mathematical analysis of the dimer. A. H. Marcus and P. H. von Hippel collaborated in conceiving and planning the experiments.

Introduction

Determination of the local structure at the single-strand (ss) – double-strand (ds) DNA junction can illuminate the mechanisms underlying the processes of replication, repair, and transcription. The base pairs at the ss-dsDNA junctions exhibit spontaneous opening and closing, so called DNA 'breathing,' driven by thermal fluctuations.[1–3] These positionally dependent structural fluctuations are binding targets for proteins that modify the genome.[4]

Previous studies examined the positional dependence of the DNA 'breathing' using the fluorescent base analog 2-amino purine (2AP).[2,3] Their work found measurable unwinding approximately two base pairs into the duplex region under physiological conditions, and bases at ssDNA sites directly adjacent to the junction were significantly more unstacked than bases at ssDNA sites further from the junction.[3] Additional work found that constructs with longer ssDNA 'tails' exhibited an increase in the unstacked character of the dsDNA base directly adjacent to the junction of the lagging strand, but not the leading, suggesting that the increased length of the ssDNA 'tails' resulted in an increased 'flexing' of the DNA construct.[2]

In order to form a complete picture of the structural variation that occurs at the DNA fork junction, the conformation of the DNA backbone must also be characterized. To that end, the cyanine dyes Cy3 and Cy5 are commonly used fluorescent dyes which can be rigidly inserted into the backbone of DNA through phosphoramidite chemical insertion methods.[5–8] Circular dichroism (CD) and UV-Vis absorption have shown that the chromophore probes do not significantly perturb the duplex structure of the DNA constructs,[8–10] and T4 primosome helicase is able to 'unwind past' these internally labeled dyes without significant difficulty.[8] It has recently been shown that the local structure of the dyes can be determined from calculations that account for the electronic-vibrational (vibronic) coupling of the chromophores.[11–13]

Additionally, the cyanine dyes have been used to detect 'breathing' motions of the DNA backbone on microsecond timescales using single molecule FRET and linear dichroism measurements.[10] While molecular dynamics simulations have shown the dyes exist in a variety of external and intercalated conformations when labeled in the DNA

duplex.[14] Although the ensemble measurements used here cannot distinguish these separate structural fluctuations, the spectral inhomogeneity can be used as a proxy to indicate the magnitude of the fluctuations about the average ensemble configuration.

As illustrated in Figure 5.1, variations in the environment surrounding the chromophores can result in a distribution of structures, and therefore a distribution of homogeneously broadened lineshapes for each system, which are added together to result in the inhomogeneously broadened total lineshape observed in ensemble measurements. Rather than calculate the distributions of the structural parameters, the inhomogeneous broadening is described by a Gaussian distribution which is convolved with the homogeneous lineshape of the average conformation.[15–17] The larger the structural distribution due to conformational fluctuations, and 'breathing' the greater the spectral inhomogeneity.

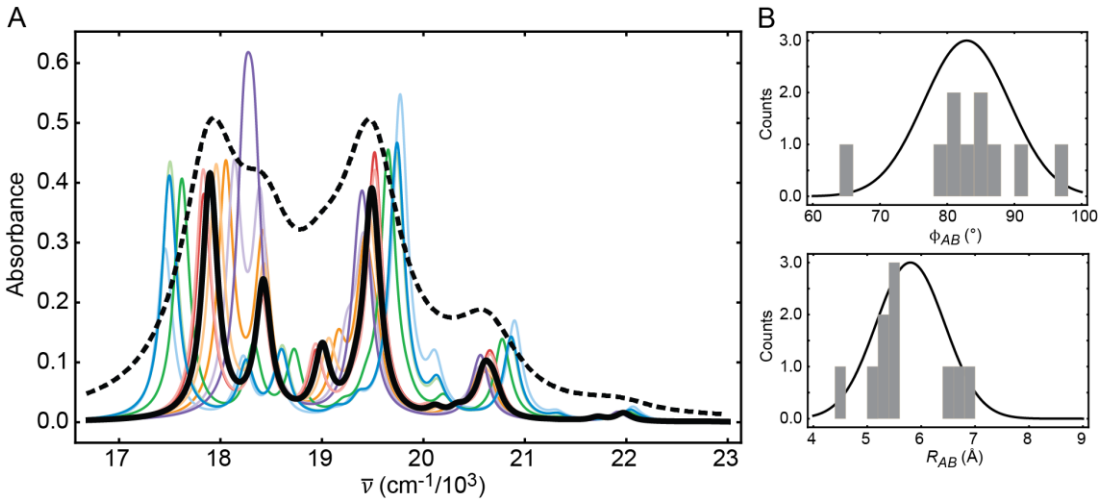

Figure 5.1: Illustration of how structural fluctuations lead to the inhomogeneously broadened spectrum. **(A)** The homogeneous lineshape of the average conformation (thick black) and 10 homogeneous lineshapes from a distribution of conformations (various colors). The inhomogeneously broadened lineshape (black dashed). **(B)** The histograms of the twist angle and separation distance used to create the 10 colored homogeneous lineshapes in **(A)** overlapped with the probability distribution used to randomly select the angle and separation distance

We examined the structural conformations of Cy3 dimers placed at positions near the ss-dsDNA fork junction compatible to those previously examined with fluorescent base analogs,[3] using absorption, CD, and two-dimensional fluorescence spectroscopy (2DFS). Our results indicate a positional dependence of the average conformation and fluctuations, reminiscent of that seen for the fluorescent base analogs.

Results

The experimental considerations and techniques used in this section are described in Chapter III, and the sequences of the DNA constructs used are presented in Table 3.2. To recall, the prefix 'D' or 'M' is used to designate between the dimer and monomer labeled DNA constructs respectively ('U' indicates an unlabeled construct). The DNA oligonucleotides labeled at the fork use the established convention where positive numbers indicate constructs labeled within the double-stranded (ds) DNA duplex region and negative numbers indicate constructs labeled within the single-stranded (ss) DNA fork region. The number indicates the position away from the ss-dsDNA fork junction. (see Figure 3.1). [2,3]

Absorption and CD Measurements

The monomer and dimer absorption and dimer circular dichroism spectra of the Cy3 labeled DNA constructs are presented in Figure 5.2. The monomer absorption does not change appreciably with dye position. The absorption and circular dichroism of the dimer constructs Dds, D3, and D2 appear similar, with a red shift and splitting of the 0-0

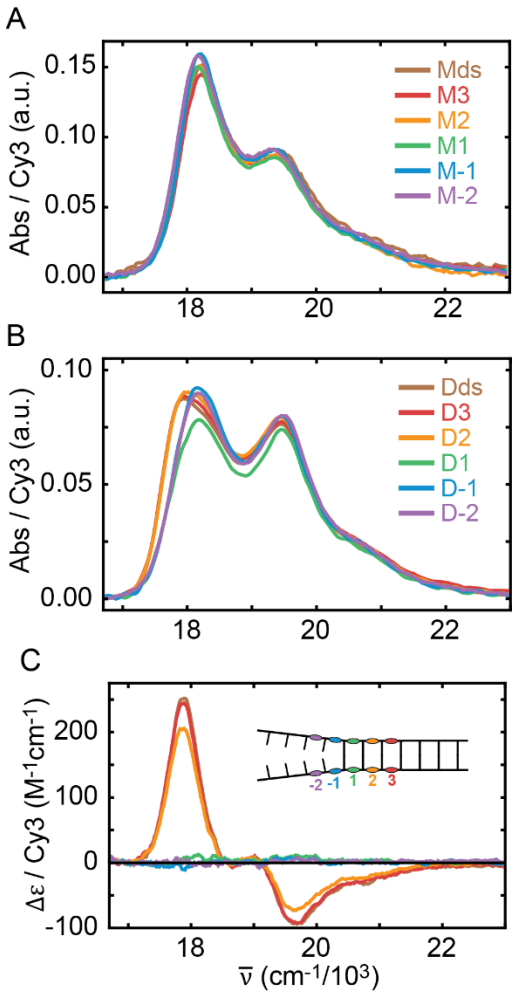

Figure 5.2: Absorption and circular dichroism measurements of the Cy3 **(A)** monomer and **(B & C)** dimer labeled constructs described in Table 3.1. Brown Mds or Dds, Red M3 or D3, Orange M2 or D2, Green M1 or D1, Blue M-1 or D-1, Purple M-2 or D-2.

feature in the absorption and a large bisignate CD signal, indicating that the conformation of the dyes ≥ 2 base pairs into the duplex region is similar to the conformation adopted by dyes buried deep within the duplex. However, the intensity of the D2 CD signal is decreased slightly, indicating some variation from the buried duplex. The constructs D1, D-1, and D-2 do not exhibit the red shift and apparent splitting of the low energy feature in the absorption spectra and the circular dichroism is reduced to near zero, however, the absorption spectra is still perturbed from that of the monomer indicating that the dyes are indeed coupled. The similarities in these spectra suggest that the dimer one base pair into

the duplex region has a conformation more similar to that of dimers within the ssDNA than that of the dsDNA. This is in agreement with prior studies indicating that the nucleotides at this position are in an 'open' configuration.[2,3]

The melting curves of the dimer samples, in which the absorption at 260 nm is examined as a function of temperature, are presented in Figure 5.3 A. The cooperative nature of the melting transition results in the sigmoidal shape of the melting curve and can be used to the determine the 'melting temperature,' in which 50% of the DNA is denatured.[18] From Figure 5.3 B we see that the fork labeled constructs melt at ~60°C, while the duplex dimer melts at 65°C and the unlabeled duplex at 67°C. The depreciation of the melting temperature of the fork samples versus the duplex constructs is partially explained by the reduction in the length of the duplex region (54 – 65% reduction). While the difference in melting temperature between Uds and Dds suggests that the presence of the Cy3 dimer partially destabilizes the oligonucleotide.

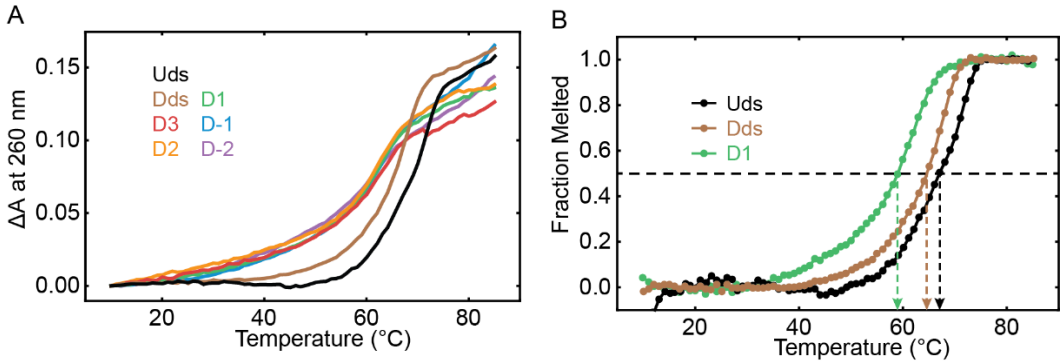

Figure 5.3: Melting curves of the fork labeled DNA constructs taken at 260 nm. **(A)** Differential absorbance of the six Cy3 fork labeled dimer constructs and the unlabeled sample Uds. **(B)** Representative fraction melted of the unlabeled, duplex, and fork constructs determined by removing the baselines.[18] The duplex dimer melts at 65°C while the unlabeled duplex melts slightly higher at 67°C and the fork constructs lower at ~60°C

Temperature dependent measurements of the six monomer constructs (Mds, M3, M2, M1, M-1, and M-2) were examined to determine the intra-molecular parameters

(transition energy ε_{eg}, vibrational mode energy ω_0, and the Huang-Rhys parameter λ^2) as was done previously.[11] The intra-molecular parameters do not appear to depend on temperature (Tables C.1 – C.6 of Appendix C) or probe position, as shown in Figure 5.4 and Table C.7 of Appendix C. The average value for the transition energy, $\bar{\varepsilon}_{eg}$, was determined to be 18,248 cm^{-1}, the average vibrational mode energy, $\bar{\omega}_0$, was 1,123 cm^{-1}, and Huang Rhys parameter, $\bar{\lambda}^2$, was 0.57.

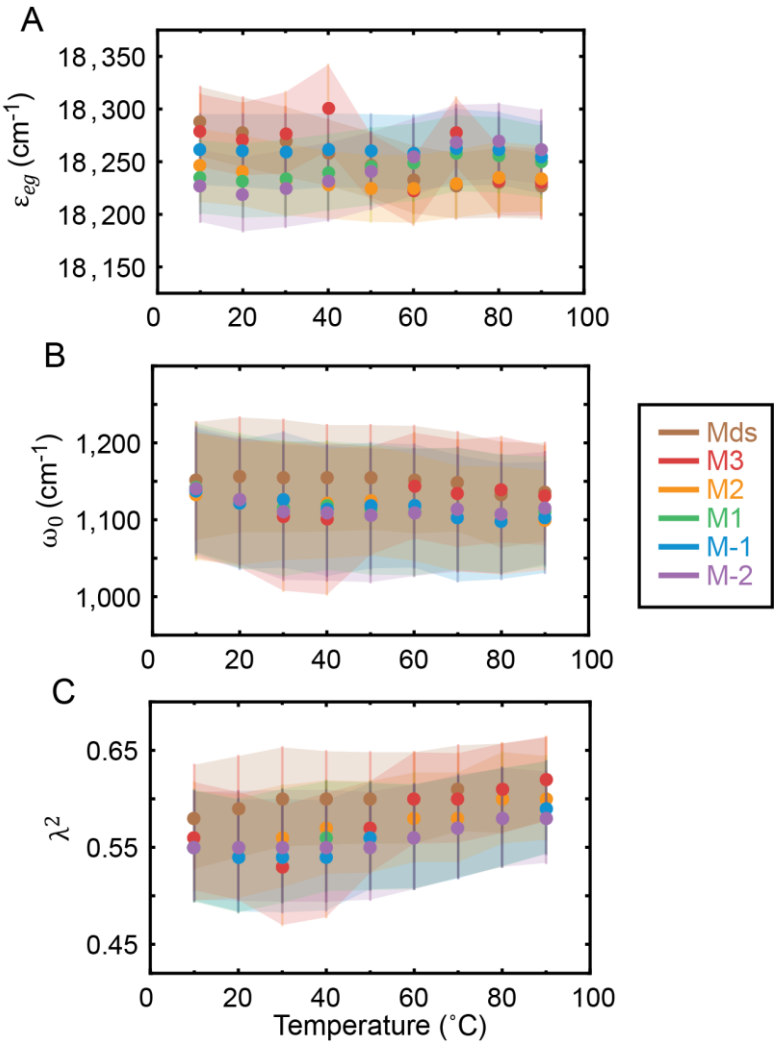

Figure 5.4: Intra-molecular parameters determined from optimizations of the monomer absorption spectra. **(A)** The transition energy ε_{eg}, **(B)** the vibrational mode energy ω_0, and **(C)** the Huang-Rhys parameter λ^2. Error bars were calculated based on a 1% deviation of the target function from its optimized values.

Conformational Determination of Cy3 Dimers Located at the Fork Junction

The absorption and CD spectra of the dimer constructs were used to determine the relative conformation of the Cy3 dyes at the various probe positions examined. Due to the increased flexibility of the fork junction, we were unable to assume that the inter-chromophore tilt angle was constrained as done previously.[11] Therefore, we performed optimizations to the absorbance and CD measurements using the inter-chromophore twist angle ϕ_{AB}, the inter-chromophore tilt angle δ_{AB}, and the inter-chromophore separation R_{AB}. The optimizations resulted in multiple conformations equally capable of reproducing the experimental absorbance and circular dichroism spectra. Therefore, the range of possible structural parameters from these degenerate configurations is presented, with the 1% deviation from the target function calculated from the upper or lower end of the structural parameter range.

At 10°C, the lowest temperature examined, the constructs Dds, D3 and D2 have a preferred structural configuration with a high degree of twist 85-80° and small separation distance 5-7 Å. With the decrease in twist angle and increase in separation as the probe is moved towards the fork. Upon increasing in temperature, the twist angle decreases and the separation distance increases while the tilt angle remains undefined within the range -10° – 20° , as shown in the left-hand side Figure 5.5.

At 10°C the constructs D1, D-1, and D-2, span a range of twist angles, from 50 to 120°, and a span of separation distances, from 6 to 13Å. The large span of optimized fit parameters removes any apparent temperature dependent trend as seen in the right-hand side of Figure 5.5. Of note, the inclusion of the tilt angle created a high degree of ambiguity, as it creates a projection of the transition dipole moment onto the separation distance,

therefore changes in the tilt angle can be countered with changes in the separation distance. When the tilt angle was minimized the separation, distance ranged from 10-12 Å. A large degree of tilt resulted in smaller separation distances until the bounds of the optimization were reached. The temperature dependent absorption and CD spectra are presented in Appendix C, Figure C.1 and the optimized conformational parameters are recorded in Tables C.8 – C.13.

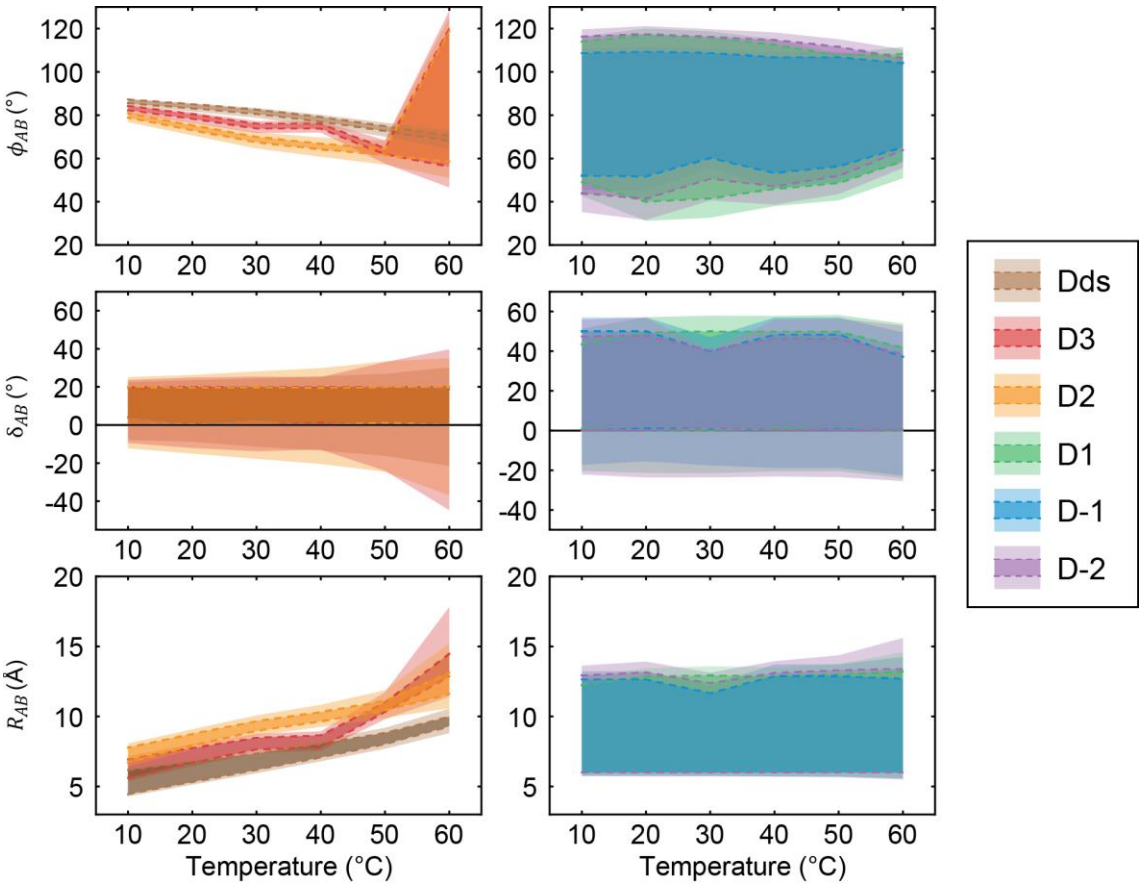

Figure 5.5: Temperature-dependent optimized structural parameters from fork junction labeled Cy3 dimer absorption and CD spectra. The dark-colored sections, marked with dashed lines indicate the range of degenerate conformational parameters and the light-colored sections indicate the calculated 1% deviation from the range boundaries. The structural parameters are the inter-chromophore twist angle ϕ_{AB}, the inter-chromophore tilt angle δ_{AB}, and inter-chromophore separation distance R_{AB}. On the left are the optimized parameters for the samples Dds (brown), D3 (red) and D2 (orange). On the right are the optimized parameters for the constructs D1 (green), D-1 (blue), and D-2 (purple).

Spectral Inhomogeneity of the Fork Junction

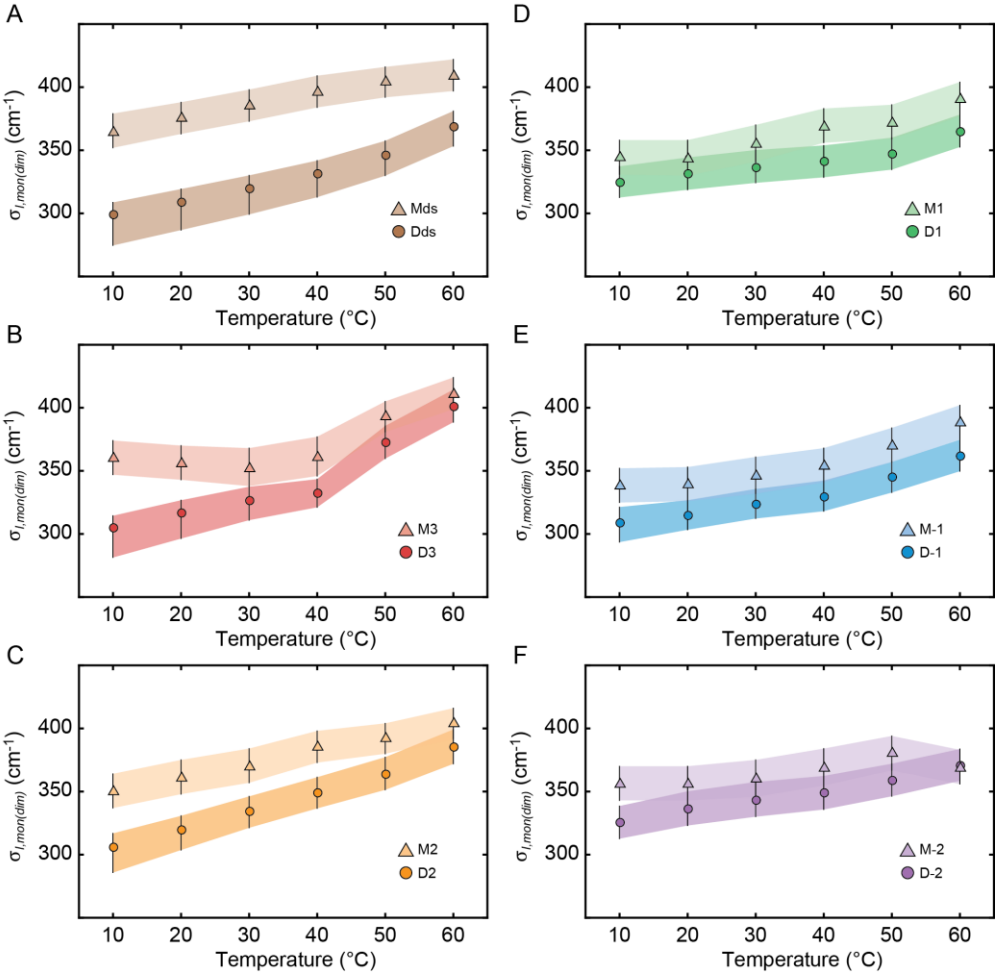

Figure 5.6: Comparison of the monomer (triangles) and dimer (circles) inhomogeneous broadening standard deviations ($\sigma_{I,mon(dim)}$) for the family of Cy3 DNA constructs labeled at the fork junction. **(A)** The duplex labeled Dds and Mds constructs, **(B)** D3 and M3, **(C)** D2 and M2, **(D)** D1 and M1, **(E)** D-1 and M-1, and **(F)** D-2 and M-2. Error bars are calculated from a 1% deviation of the target function.

In Figure 5.6 we compare the spectral inhomogeneity of the monomer ($\sigma_{I,mon}$) and dimer ($\sigma_{I,dim}$) for the six probe positions examined. All constructs exhibit an increase in the inhomogeneous standard deviation as a function of temperature. The constructs labeled $\geq$ 2 base pairs into the duplex region (Figure 5.6 A-C) exhibit a clear difference in the amount of spectral inhomogeneity between the monomer and dimer at low temperature, and a reduction in that difference as the temperature is increased to near the melting

temperature. The other constructs (Figure 5.6 D-E) have a much smaller difference between the dimer and monomer at low temperature, suggesting that the increased flexibility near the fork junction allows the molecules of the dimer to experience a greater degree of structural fluctuations near the fork, similar to that seen by the monomer.

The temperature dependent spectral inhomogeneity by probe position is compared in Figure 5.7 for both monomer (A) and dimer (B) constructs. The constructs in which the monomer probe is labeled within the double-stranded (ds) DNA tend to have a larger inhomogeneous standard deviation than the constructs labeled within the single-stranded (ss) DNA tails and this trend is maintained across temperatures. The dimer constructs however, have a lower inhomogeneous standard deviation for the dsDNA labeled probes, indicative of positional dependent DNA 'breathing' whereby the labels adjacent to or past the fork junction experience a larger distribution of structural fluctuations than those buried within the duplex. Interestingly, upon heating, the trend inverts and at elevated temperatures the dsDNA labeled structures have a larger inhomogeneous standard deviation than the ssDNA constructs.

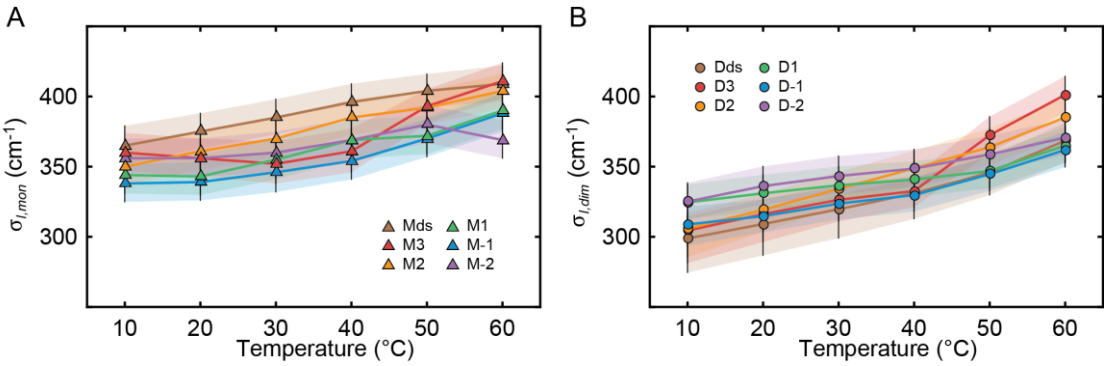

Figure 5.7: Comparison of the temperature dependent inhomogeneous broadening standard deviation across probe position for the monomer constructs **(A)** Mds – brown, M3 – red, M2 – orange, M1 – green, M-1 – blue, M-2 – purple, and the dimer consructs **(B)** Dds – brown, D3 – red, D2 – orange, D1 – green, D-1 – blue, D-2 – purple. Error bars are calculated from a 1% deviation of the target function.

Effects of ssDNA 'Tail' Length

We compared the constructs D-1 and F(Cy3)$_2$ (DNA sequence presented in Table 3.1), as they had the same probe position relative to the fork junction but different lengths of the ssDNA 'tails' (11 bases versus 30 or 44 bases for the leading or lagging strand respectively). The absorption and CD spectra of these samples, along with their temperature dependent conformational parameters are presented in Figure 5.8. The absorption spectra of these samples are similar, however the F(Cy3)$_2$ dimer construct has a large CD signal and D-1 has little to no discernable CD signal from the noise. A moving average of the D-1 CD highlights a trend similar to that of the F(Cy3)2 construct, but additional measurements with a reduction in the noise are necessary to validate this.

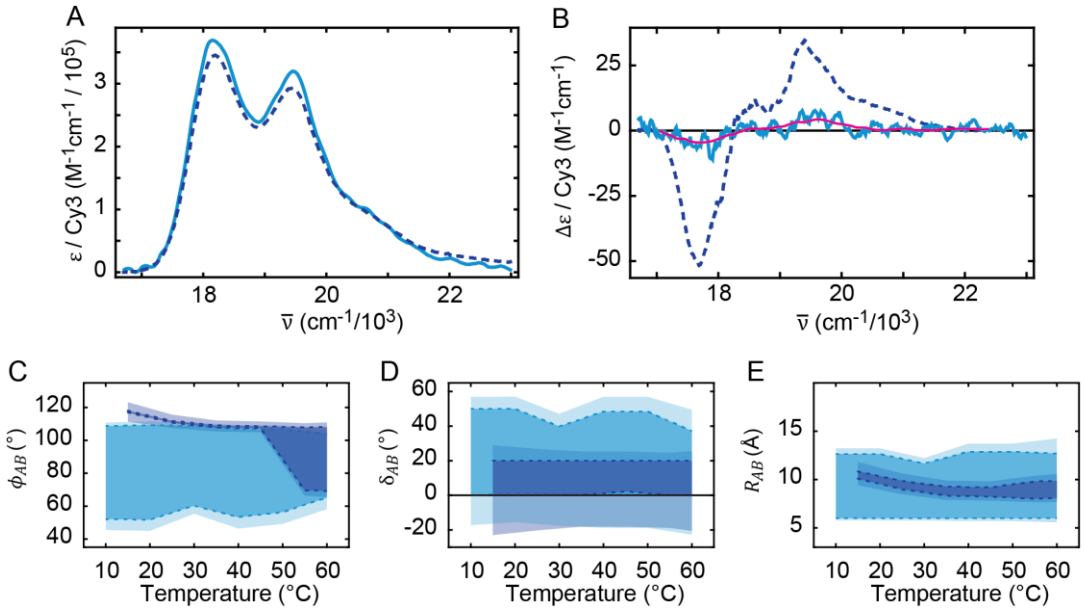

Figure 5.8: Comparison of the **(A)** absorption and **(B)** CD spectra of the constructs F(Cy3)$_2$ (dark blue, dashed) and D-1 (light blue, solid), in which the Cy3 dimer is in the same position relative to the fork, but the length of the ssDNA tails and duplex region are different. The magenta overlay on the D-1 CD spectra is the moving average, with a span of 50. **(C - E)** Optimized structural parameters determined from the absorption and CD of the D-1 and F(Cy3)$_2$ DNA constructs **(C)** inter-chromophore twist angle ϕ_{AB}; **(D)** inter-chromophore tilt angle δ_{AB}; **(E)** inter-chromophore separation R_{AB}

Two possibilities exist that could explain the same perturbation of the absorbance spectra yet different CD spectra. At a twist angle of 90° the sign of the CD inverts (as does the sign of the excitonic coupling). Therefore, a large distribution of conformations about 90° or a bimodal distribution equally distributed around 90° (i.e. 65° and 115°) would result in the cancellation of the CD signal. As previously discussed, the longer ssDNA tails are thought to flex the DNA,[2] which may result in the preferential conformation of the Cy3 dyes in the F(Cy3)$_2$ construct (ϕ_{AB} = 115° and R_{AB} = 10 Å) while the Cy3 dimer in the D-1 exists in a range of conformations.

Conformations Determined from Two-Dimensional Fluorescence Spectroscopy

The inability to determine a unique solution for the fork labeled constructs with greater conformational flexibility led to the use of two-dimensional fluorescence spectroscopy in an attempt to elucidate the average conformation of the ensemble. As described in Chapters II and III, 2DFS is sensitive to local structure and an indispensable tool for conformational determination. This technique has been used by our group to determine the relative conformation of electronically coupled porphyrin systems and dinucleotides.[19–22] However, this is the first examination by our group of excitonically coupled systems that exhibit electronic-vibrational coupling.

Representative 2DFS spectra of the fork dimer constructs, D2 and D1, are presented in Figure 5.9. These constructs were chosen as they exhibit the greatest amount of change between two neighboring probe positions. The full sets of 2D spectra for these constructs are presented in Figures C.2 and C.3 of Appendix C. The laser excitation was centered at 532 nm with a bandwidth of ~50 nm. The variation in the positions and weightings of the

off-diagonal coupling terms provides insight into the conformational differences of the constructs.

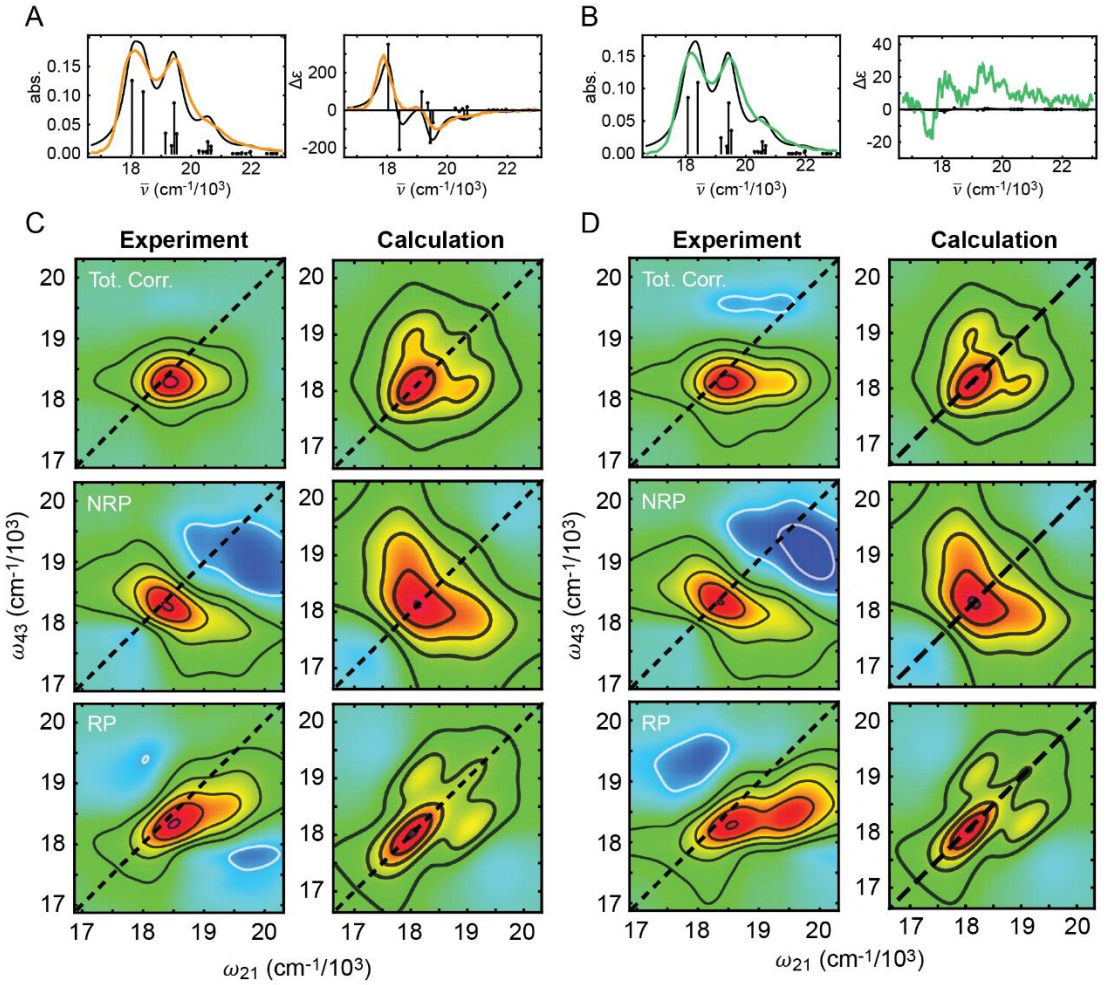

Figure 5.9: Calculated optimizations from the absorption, CD, and 2DFS spectra of the D2 and D1 dimer DNA constructs. **(A)** Absorption and CD of D2 (orange) overlaid with the calculated spectra (black). **(B)** Absorption and CD of D1 (green) overlaid with the calculated spectra (black). **(C)** The real part of the total correlation (Tot. Corr.), rephasing (RP) and non-rephasing (NRP) 2DFS spectra for the experimentally collected (left) and calculated (right). (D) The real part of the total correlation (Tot. Corr.) rephasing (RP), and non-rephasing (NRP) 2DFS spectra for the experimentally collected (left) and calculated (right)

The 2DFS spectra were calculated according to Eqs. (2.27 - 2.32) with the corrections given by Eqs. (2.35 and 2.36) to account for the finite bandwidth of the laser, the super Gaussian exponential factor was given by b_L = 1.5. The optimized spectra for the

constructs D2 and D1 are shown next to the experimental spectra in Figure 5.9, and the full set of calculated 2D spectra are presented in Figures C.4 and C.5.

The optimization from the absorption, CD, and 2DFS of the D2 dimer DNA construct determined an average structural conformation with ϕ_{AB} = 79.6°, δ_{AB} = 8.5°, and R_{AB} = 7.7 Å, resulting in an excitonic coupling constant J = 349 cm^{-1}. The relative fluorescence quantum yield from the doubly excited states to the singly excited states was found to be Γ_{2D} = 0, and the homogeneous broadening was optimized at Γ_H = 200 cm^{-1} while the standard deviation of the inhomogeneous broadening was $\sigma_{i,dim}$ = 307 cm^{-1}. The optimized configuration for D1 was determined to be ϕ_{AB} = 105.3°, δ_{AB} = 34.4°, and R_{AB} = 5.63 Å, resulting in an excitonic coupling constant J = -304 cm^{-1}, with Γ_{2D} = 0, Γ_H = 200 cm^{-1}, and $\sigma_{i,dim}$ = 316 cm^{-1}. For both constructs the relative quantum yield from the doubly excited state to the singly excited state, as given by the parameter Γ_{2D}, is negligible. Thus, indicating that the population in the doubly excited state undergoes non-radiative relaxation processes in this system. Due to the computational cost of optimizing to the 2DFS spectra, an insufficient number of optimizations were output in order to determine if there was a single optimal configuration or a range of degenerate structural conformations as was seen for the linear spectra. However, these results suggest the structural constraints within the duplex dimer that result in a right-handed configuration of the cyanine dimer relax and at positions adjacent to or past the ss-ds DNA fork junction, the dimers can adopt either left- or right-handed configurations. The 2DFS or absorption spectra alone cannot distinguish the orientation of the twist, highlighting the importance of utilizing the three techniques simultaneously.

Conclusions

We examined the conformations of the Cy3 dimers labeled at the ss-dsDNA fork junction using absorption, circular dichroism, and two-dimensional fluorescence spectroscopy. From our analyses we determined that Cy3 dimers labeled two base pairs or more into the duplex region of DNA experience conditions near equivalent to that of dimers labeled deep within the duplex region. Adopting local conformations with an inter-chromophore twist angle of ~83° twist and a separation distance of 6 Å. While dimers labeled one base pair into the duplex region experience conditions equivalent to that of dimers labeled within the non-complementary single-stranded region. The conformations of these fork labeled constructs exhibited a large range of structural parameters that are equally capable of recreating the absorption and CD signal with an inter-chromophore tilt from 60 to 115° and separation distance of 6 to 13Å. The tilt angle remained indeterminate from optimizations to the absorption and circular dichroism.

At low temperatures, the duplex labeled constructs exhibited less spectral inhomogeneity than the constructs labeled adjacent to or past the ss-dsDNA junction, indicative of the positional dependent DNA 'breathing' that occurs at the junction.[1–3] Increasing the temperature resulted in an increase in the spectral inhomogeneity due to thermally populated sub-states, likely a result of 'bubble' formation as the DNA denatures.[1]

Differences were found in samples with the same relative Cy3 probe position to the fork but different lengths of the ssDNA tails. There are two possible explanations that account for this, either a large distribution about $\phi_{AB} = 90°$ or a bimodal distribution of twist angles with equally likely hood of twisting left or right handed away from 90° (i.e. 65° and 115°). The construct with the longer ssDNA regions adopted preferential average

configuration with a twist angle of 115°, whereas the construct with shorter ssDNA regions did not exhibit a preferential orientation within the limits of our experiments. These results are consistent with prior findings that longer ssDNA strands result in a 'flexing' of the fork junction that perturbs one strand more than the other.[2]

The calculated 2DFS spectra for the D2 and D1 constructs appear strikingly similar given the differences in the structural parameters. This suggests that the 2DFS may not be as sensitive to structural variation when the electronic-vibrational coupling of the chromophore is included. The current implementation of the simple Holstein Hamiltonian model to calculate the 2DFS spectra cannot distinguish conformations when the excitonic coupling parameter is equivalent or opposite as a result of the twist angle exceeding 90°. The combination of fitting the absorption and CD with the 2DFS spectra is therefore necessary to reduce the ambiguities in the system.

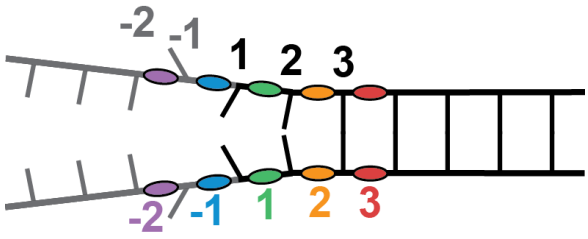

Figure 5.10: Representation of the structure near the fork junction. Black is used to indicate the complementary bases within the 'duplex-region' while gray indicates the non-complementary 'fork-region.' Labels above indicate the base positions as described by Davis et al. and below indicate the Cy3 positions used in this work. Cy3 probes at positions -2, -1, and 1 exhibit similar behavior, while Cy3 probes at positions 2, and 3 appear like that of dyes located within the duplex region.

Figure 5.10 illustrates our analysis of the DNA fork junction combined with the prior work of others. Under physiological conditions, unwinding penetrates two base pairs into the duplex region,[3] resulting in the backbone and Cy3 positioned one base into the complementary dsDNA region to appear equivalent to the Cy3 probes located within the

ssDNA tails, with the base adjacent to the junction less stacked than the others.[3] While the breathing penetrates ~2bp into the duplex, the Cy3 probes located beyond those base pairs appear predominantly like those labeled deep within the duplex, with slight variation at the second position.

Summary and Bridge to Chapter VI

Chapters IV and V examined the average conformations that Cy3 dimers adopt when labeled within DNA, resulting in intermediate-to-strong exciton coupling that can be 'tuned' with temperature and probe position while the intra-molecular parameters remain approximately constant. This property suggests that the Cy3 dimer labeled DNA constructs could be useful model systems to examine the role of electronic-vibrational coherence within exciton-coupled molecules. Chapter VI will examine the electronic-vibrational coherence of the duplex dimer labeled DNA construct using time dependent two-dimensional fluorescence spectroscopy.

CHAPTER VI

EXCITED STATE DYNAMICS OF EXCITONICALLY COUPLED CY3 DIMERS

Overview

This chapter examines the excited state dynamics and observed oscillatory behavior of the time-resolved two-dimensional fluorescence spectroscopy signal of the duplex labeled $D(Cy3)_2$ dimer DNA construct. This section contains co-authored work. I preformed data collection and analysis of experiments conceived and planned in collaboration with A. H. Marcus.

Introduction

Time-resolved ultrafast experiments have repeatedly observed the spectral signatures of long-lasting coherence in photosynthetic antenna complexes, suggesting that quantum coherence may contribute to the energy transfer mechanism.[1–6] Although initially ascribed to excitonic beatings, recent studies have shown that the oscillatory behavior of the spectral response can be understood by considering the role of vibrations, specifically delocalized electronic vibrational states.[7–11] Unambiguous assignment of the spectral features remains difficult due to the complex structure of the 2D spectra o large photosynthetic antenna complexes. Therefore, molecular model systems that utilize resonant excitonic coupling in combination with intra-molecular electronic-vibrational (vibronic) coherence provide a resource to examine the role of coherence in energy transfer.

The chromophore Cy3 is one such model system. Time-resolved ultrafast studies have been done on Cy3 dimers directly tethered by butyl chains creating an *bis*-cyanine H-dimer,[8,9] and large J-aggregates of Cy3 in which the molecules from mesoscopic tubes.[10,11] Studies of both systems revealed oscillatory features. In the case of the dimer a long-lived oscillation with a frequency of ~1,400 cm^{-1} was observed and assigned to the inter-exciton coherence.[8,9] Whereas the studies of the J-aggregates found lower frequency oscillations, at 160 and 476 cm^{-1},[11] or 462 and 705 cm^{-1}.[10] These oscillatory features were assigned to vibrational coherence in the ground state and vibronic coherence in the excited state,[11] or as a result of a coherent interaction of excitonic bands with an underdamped, quasi-resonant vibration.[10]

As seen previously, the cyanine dyes internally labeled within DNA exhibit intermediate-to-strong excitonic coupling that can be tuned with temperature[12] and probe position. This allows for the separation of the effects of the vibronic coupling from the excitonic coupling contribution. In this work, we examined the ultrafast dynamics of a Cy3 dimer located deep within the constrained duplex region of DNA at room temperature using time resolved two-dimensional fluorescence spectroscopy (2DFS). We observed low frequency oscillatory features and modeled the response using the simple Holstein model.

Results

The experimental conditions and DNA sequence of the cyanine dimer DNA construct, $D(Cy3)_2$, are described in Chapter III and the temperature dependent excitonic coupling and local structure of the dimer DNA construct are explored in Chapter IV. In this work, room temperature (22°C) time resolved two-dimensional fluorescence

spectroscopy experiments were performed with the laser excitation centered at 530 nm and approximately 16 nm of bandwidth. We examined a population time (t_{32}) range from 0 – 350 fs in 5 fs step increments. Figure 6.1 presents the 2DFS spectra taken at $t_{32} = 0$, the laser excitation spectrum overlaid with the absorption spectrum is displayed above and to the right of the 2D spectra, from this we can see that the laser was positioned between the 0-0 and 1-0 features of the absorption spectrum but the laser bandwidth is smaller than the effective vibrational mode used to describe the system ($\Delta\bar{\nu}_L \approx 555$ cm^{-1} versus $\omega_0 = 1{,}110$ cm^{-1}).

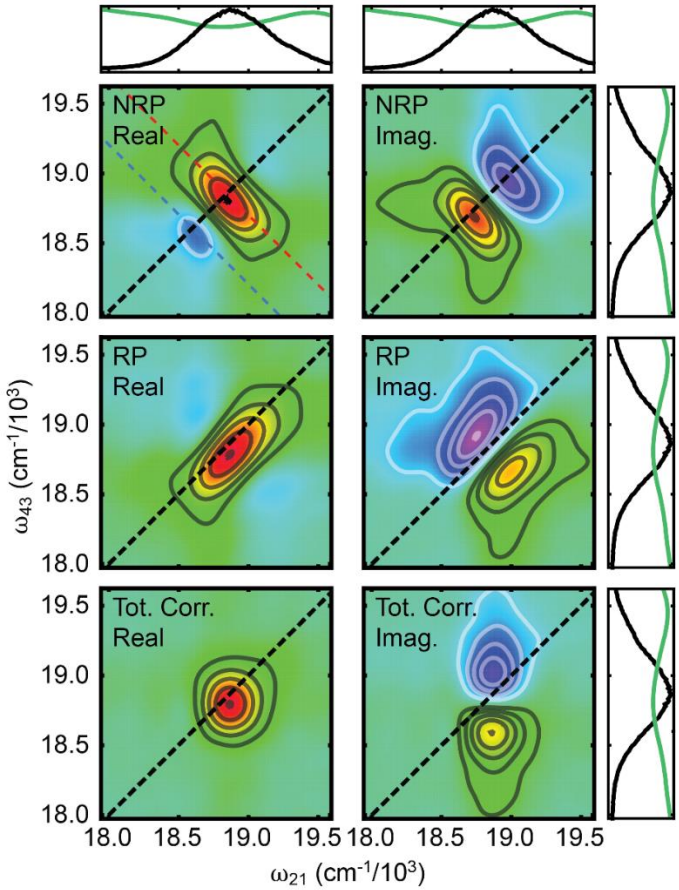

Figure 6.1: 2DFS spectra of the D(Cy3)$_2$ DNA complex with narrow bandwidth laser excitation. Shown are the real and imaginary components of the non-rephasing (NRP), rephasing (RP), and total correlation (Tot. Corr.) spectra. The laser spectrum (black) is overlaid with the D(Cy3)$_2$ absorption spectrum (green) over the region examined in the 2D plots. The anti-diagonal dashed blue and red lines in the real part of the NRP indicate where the time-resolved spectra was examined as a function of the population time (t_{32}).

Although the 2DFS spectra, under narrowband conditions, do not have the distinguishable features observed with larger bandwidth laser excitation (compare to Figure 5.6), regions of the spectra oscillate in amplitude with population time. This is demonstrated in Figure 6.2 A, where anti-diagonal slices of the non-rephasing (NRP) spectra (taken at the locations of the dashed red and blue lines in Figure 6.1) are plotted with respect to t_{32}. In Figure 6.2 B we plot the point amplitude taken from the diagonal – anti-diagonal crossing points of the NRP spectra with respect to t_{32}. From this, it is apparent that there is a non-oscillatory decay underlying the long-lived oscillatory features.

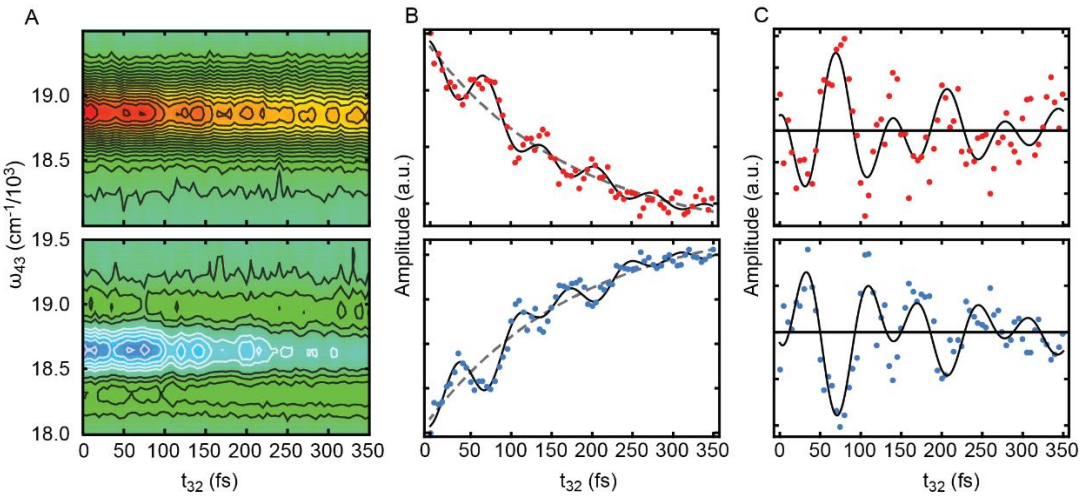

Figure 6.2: The oscillatory behavior of the NRP signal. **(A)** Slices taken along the antidiagonal positions of the NRP signal indicated in Figure 6.1 as a function of the population time. **(B)** Point amplitudes as a function of population time taken at the anti-diagonal / diagonal crossing points. The dashed gray line indicates the non-oscillatory decay and the solid black line is the best fit trace using two oscillatory frequencies. **(C)** The oscillatory features with the non-oscillatory decay removed, the solid black line indicates the best fit dampened sine function

This non-oscillatory decay was removed according to

$$y = y_0 + A_{tot} \exp\left[{}^{-t_{32}}/_{\tau_{tot}}\right] \tag{6.1}$$

where A_{tot} indicates the amplitude and τ_{tot} is the dephasing time.

A summation of damped sine waves was then used to characterized the oscillatory behavior of the point amplitudes[1]

$$y = \sum_{i=1}^{2} A_i \exp\left[{}^{-t_{32}}/_{\tau_i}\right] \sin(\omega_i t_{32} + \varphi_i) \tag{6.2}$$

where A_i, ω_i, φ_i, and τ_i indicate the amplitude, frequency, phase, and damping time constant of the i^{th} component $(i = 1 - 2)$. We chose to fit the oscillatory feature with two frequency components, as the Fourier transform with respect to t_{32} revealed two main frequency signatures (discussed below). The best fits are shown overlaid in Figures 6.2 B & C and the fit frequencies and dampening times are presented in Table 6.1, a complete table of all fit parameters is presented in Appendix D, Table D.1. The non-oscillatory had a dephasing time of approximately 185 fs, while the oscillatory components had dampening constants with similar timescales, from 200 – 250 fs.

Table 6.1: Analysis of the oscillatory features of the dimer NRP signal. Presented are the oscillatory frequencies ω_i, the damping times τ_i, and the dephasing time τ_{tot}.

	ω_1 (cm^{-1})	ω_2 (cm^{-1})	τ_1 (fs)	τ_2 (fs)	τ_{tot} (fs)
blue	250	489	200	223	192
red	249	483	200	247	181

Characterization of the Oscillatory Behavior

The Fourier transforms of the point amplitudes taken from the real part of the NRP spectra are presented in Figure 6.3, and indicate two main oscillatory frequencies were present. A larger ~490 cm^{-1} feature and a smaller amplitude ~250 cm^{-1} feature. Our examination of the D(Cy3) monomer labeled DNA construct in the same positions of the

NRP spectrum revealed a single oscillatory component, the lower frequency ~250 cm^{-1} feature. This suggests that this lower frequency oscillation may be a result of the intra-molecular properties of the Cy3. However, our simple Holstein Hamiltonian model uses only a single effective vibrational mode at 1,110 cm^{-1} and cannot account for this oscillatory feature in the monomer spectra.

The absence of the ~490 cm^{-1} from the monomer indicates that this feature may be a result of the excitonic coupling of the vibronically coupled $D(Cy3)_2$ dimer, and is similar in magnitude to the Davydov splitting of the 0-0 feature observed in the absorption and circular dichroism spectra at 25°C which was determined to be 511 cm^{-1}.[12] This feature is also similar to the oscillatory feature observed in the study of the J-aggregate system, a result of the coherent interaction of the excitonic bands with a quasi-resonant vibration. The excitonic splitting is similarly matched to the out of plane vibrations observed in resonant Raman spectra of a related cyanine dye[13] shown to couple to excitons[14] which could explain the oscillatory behavior observed.

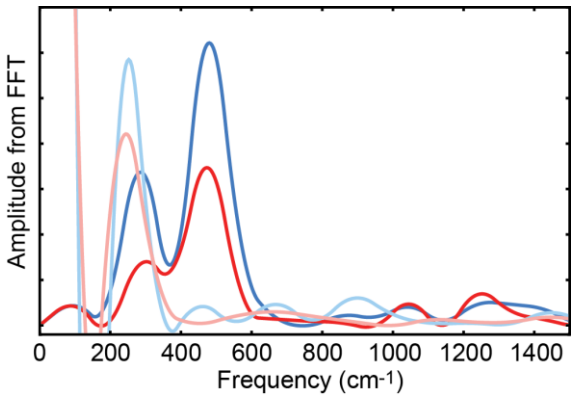

Figure 6.3: The Fourier transform of the point amplitudes taken from the time-resolved NRP spectra of the Cy3 dimer and monomer labeled DNA constructs after the slow decay had been removed. The spectra indicate the dimer has oscillatory features at ~490 cm^{-1} and ~250 cm^{-1} while the monomer has ~ 240 cm^{-1}.

We performed a Fourier transform along the waiting time t_{32} for all points on the 2D non-rephasing (NRP) and rephasing (RP). These 2D FFT maps allow the lineshape of the beating signal to be visually mapped onto 2DFS spectra.[10,11,15,16] Figure 6.4 shows the amplitude distribution for the two strongest oscillations, 250 cm^{-1} and 490 cm^{-1}. The real positive (negative) part of the NRP and RP spectrum at t_{32} = 0 is shown as black (white) contour lines.

We see that the features of the NRP spectrum beating at 250 cm^{-1} predominantly occurs along the diagonal, with greatest amplitude occurring at a position between the positive and negative features. These same positions oscillate at the higher, ~490 cm^{-1} frequency as well. In the RP spectrum, the position of greatest oscillation is an upper off-diagonal feature, in addition to features in a secondary upper off-diagonal position and on the positive feature along the diagonal.

We calculated the time dependent 2D response using our simple Holstein model for the Cy3 dimer system given the correction for the finite bandwidth [Eqs. (2.35) & (2.36)]. For these calculations we used the intra-molecular and structural parameters determined from optimizations to the absorption and circular dichroism spectra (electronic transition energy $\varepsilon_{eg} = 18{,}277$ cm^{-1}, effective vibrational mode frequency $\omega_0 = 1{,}109$ cm^{-1}, Huang-Rhys parameter $\lambda^2 = 0.56$, inter-chromophore twist angle ϕ_{AB} =80.1°, inter-chromophore tilt angle $\delta_{AB} = 0°$, inter-chromophore separation R_{AB} =6.5 Å).[12] A value of $\Gamma_{2D} = 0.2$ was used to describe the relative quantum yield from the doubly excited state to the singly excited state, and the homogeneous and inhomogeneous broadening parameters were given by $\Gamma_H = 250$ cm^{-1}, $\sigma_{I,dim} = 225$ cm^{-1}. The 2D FFT maps from the calculated spectra predict similar locations of oscillatory behavior for the NRP spectra, however they calculated RP

spectra do not exhibit the oscillatory amplitude seen on the positive feature along the diagonal.

The differences in the positions of the oscillatory features determined experimentally and from our Holstein model may be a result of the correction used to account for the finite bandwidth of the laser. In considering the overlap of the inhomogeneously broadened lineshapes with the laser excitation spectrum, we are effectively shifting the transitions to the edges of the inhomogeneously broadened spectra that underlie the laser, thereby selecting out components on the blue edge of the 0-0 feature and red edge of the 1-0 feature. This results in the reduction the effective spacing between the 0-0 and 1-0 feature, from approximately 1,200 cm^{-1} to approximately 530 cm^{-1}. Likewise, the spacing between the two transitions under the 0-0 feature previously had a Davydov splitting of 511 cm^{-1}, now have a spacing of ~245 cm^{-1}. Resulting in ambiguities about the identity of the oscillatory features.

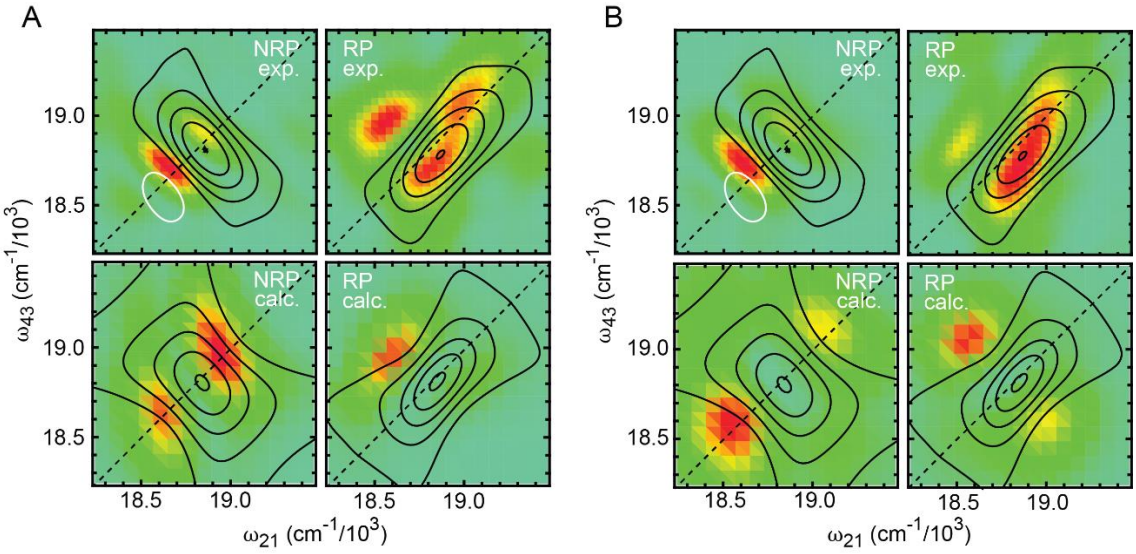

Figure 6.4: The Fourier-transform amplitude maps of the non-rephasing (NRP) and rephasing (RP) spectra for the two strongest oscillations observed experimentally. **(A)** The positions of features beating at a frequency of 250 cm^{-1} determined from the experiment (left) and Holstein model calculation (right) with the contour lines indicating the real part of the NRP and RP. **(B)** Positions of the features beating at 490 cm^{-1}.

The Fourier transform of the points along the diagonal of the NRP spectrum are shown in Figure 6.5. We see that the same oscillation frequencies dominate in the calculation as were observed experimentally, with a redistribution of relative amplitude. In comparison, the calculated Fourier transform for points taken from a calculation using a broad white light excitation are dominated by oscillations at a higher, 1,200 cm^{-1} frequency.

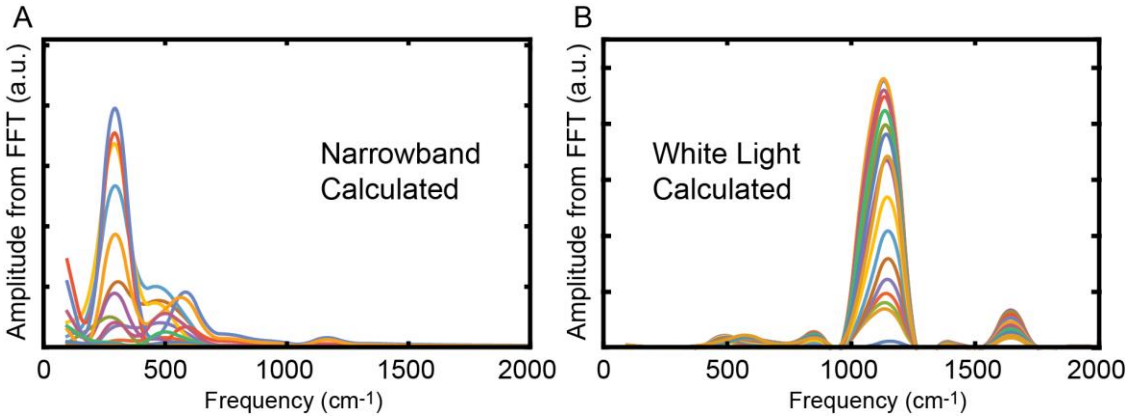

Figure 6.5: Fourier transforms of points taken along the diagonal of the time-resolved NRP spectrum calculated using the Holstein model under **(A)** narrow band conditions and **(B)** broad white light continuum conditions.

We examined the 2D FFT map of the NRP spectrum of the white light calculated time resolved signal to examine the positions of oscillatory behavior when unperturbed by transition energy shifts due to the corrections for the laser, Figure 6.6. We see from these 2D FFT maps that the lower frequency oscillations coincide with features that are along the diagonal at the 1-0 position, or off-diagonal positions which couple the 0-0 and 1-0 features. Whereas the higher frequency, ~1,260 cm^{-1}, feature occurs along the diagonal between the 0-0 and 1-0 features where the amplitude of the NRP spectrum is lowest. The RP spectrum has similarly positioned places of oscillation amplitude for the lower frequency features, however the ~1,260 cm^{-1} feature occurs in the off diagonal positions rather than the diagonal as observed in the NRP. This higher frequency oscillation matches

the spacing between the 0-0 and 1-0 feature of the absorption spectrum, therefore it is reasonable that the positions of greatest amplitude occur on the regions of the 2DFS spectra where these spectral features are coupled.

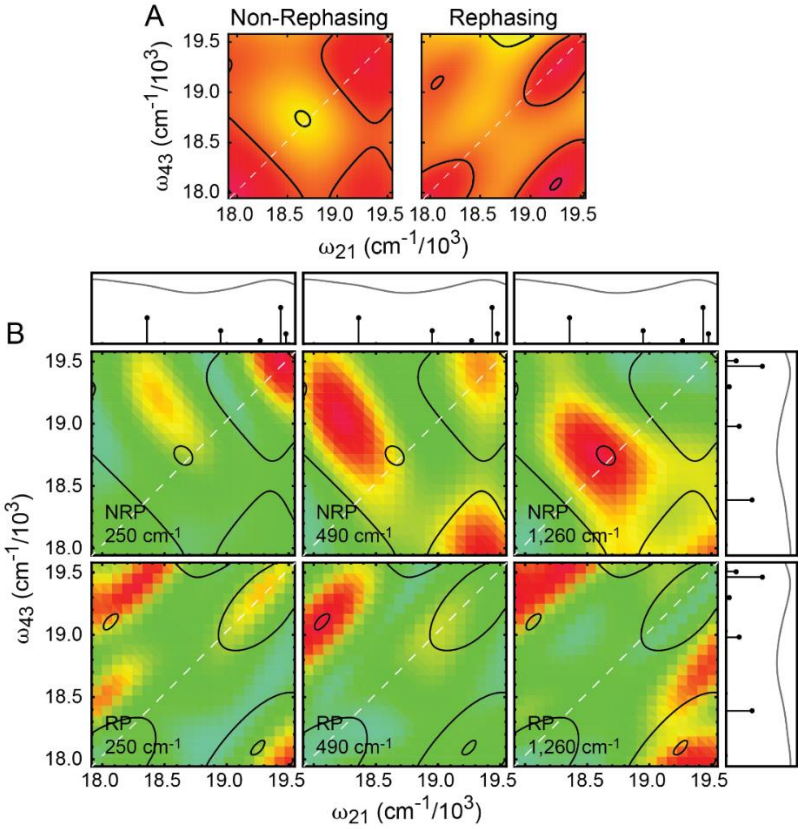

Figure 6.6: Examination of the oscillatory features calculated under white light conditions. **(A)** The real part of the NRP and RP 2DFS spectra at $t_{32} = 0$. **(B)** 2D FFT maps of the two frequencies observed under narrow band conditions (250 cm^{-1} and 490 cm^{-1}) and the dominant oscillatory feature observed for the white light calculation (1260 cm^{-1}).

Conclusions

We examined the excited state dynamics of the $D(Cy3)_2$ dimer when labeled in DNA using time-resolved 2DFS measurements. We found that the dimer exhibited two long oscillatory features on a non-oscillatory decay. The oscillatory features could be described by two frequencies, ~250 cm^{-1} and ~490 cm^{-1} with damping time constants of ~220 fs. Examination of the monomer construct revealed a single oscillatory feature at the

lower, ~250 cm^{-1} frequency, thus indicating the lower frequency may be due to intra-molecular vibrational coherence unaccounted for in our simple Holstein model. However, analysis of the dimer under the simple Holstein model of the dimer did yield oscillations of this frequency.

The ~490 cm^{-1} oscillatory feature observed in the dimer is approximately equal to the Davydov splitting of the 0-0 feature observed in 25°C absorption and CD spectra. It is also closely matched to the out of plane vibration of the cyanine dye indicating that it may be a result of a coherent interaction of the excitonic bands with the quasi-resonant vibration as observed in the J-aggregate system.[10]

A more robust inclusion of the finite laser bandwidth will be necessary to account for the ambiguities in the origins of the oscillatory features. Under the current implementation, the transitions within the broad inhomogeneous lineshapes, likely a result of the structural variation and fluctuations that occur due to DNA 'breathing,' [17] are considered uncorrelated. Therefore, our laser can selectively excite features from the blue edge of the broadened 0-0 mode and the red edge of the 1-0 mode. This results in effectively reducing the vibrational mode from 1,200 cm^{-1} to 530 cm^{-1}.

When compared with the calculation of the white light model we see that the oscillatory behavior is dominated by a higher frequency feature at ~1260 cm^{-1} corresponding to the vibronic coupling of the system. This feature is inaccessible in our system because of the limited bandwidth of the laser used. Increased laser bandwidth may access the higher oscillatory feature which matches the separation of the 0-0 and 1-0 features of the absorption spectrum as was seen in the examination of the *bis*-cyanine H-dimer system.[8,9]

The advantage of the Cy3 dimer labeled DNA system over that of the *bis*-cyanine dimer or J-aggregates is the 'tunability' of the system with temperature. The electronic-vibrational coupling within the molecule remains constant with temperature, while the electronic coupling between the two chromophores varies.[12] This allows for the exploration of the models put forward to explain the effects of vibronic coherences in energy transport of biomolecular systems

CHAPTER VII

CONCLUDING REMARKS

Throughout this dissertation we have examined the local structure and excited state dynamics of cyanine dye dimers, Cy3 and Cy5, when internally labeled within the backbone of DNA. This was done using the complementary techniques of absorption, circular dichroism (CD), and two-dimensional fluorescence spectroscopy (2DFS). The experimental data was fit using the simple Holstein model to account for the electronic-vibrational (vibronic) coupling in addition to the excitonic coupling.

Our Holstein model includes several simplifying approximations, such as the use of a single effective vibrational mode and the characterization of the exciton coupling through the point dipole approximation. The success of using a single effective vibrational mode is likely a result of the intense Raman-active vibration at ~1200 cm^{-1}, which is attributed primarily to symmetric stretching of the polymethine bridge of the chromophore.[1] If additional vibrational modes were included the increased density of states would enable a more accurate fit to the observed experimental spectra, particularly in the higher energy regions.[2] However, it is not clear if the inclusion of additional modes would provide additional physical meaning to the system. Likewise, a more robust model of the exciton coupling could be applied to our system, as the separation distance is smaller than the length of the chromophores and is on the same order as the dipole radius.[3,4] However, the main advantage of these approximations is in the simplicity, as it lends itself to be used commonly amongst molecular biological research groups that rely on linear spectroscopic

techniques (absorption and CD) to examine the local structure and disorder of fluorescently labeled systems.

In the examination of our fluorescently labeled DNA constructs, we saw that the intramolecular parameters of the cyanine dyes Cy3 and Cy5 remain effectively constant with temperature and probe position. While the inter-chromophore structural parameters exhibited temperature and position dependence. When labeled within the double-stranded duplex of DNA, the cyanine dyes adopt a closely packed, near orthogonal configuration with a right-handed preference. As the cyanine dimer is moved closer to the single-strand – double-stranded fork junction, we see that the twist angle relaxes, and the separation increases for dyes labeled ≥ 2 base pairs into the duplex. However, dyes located adjacent to the fork junction or within the single-stranded DNA region adopt either a large distribution or bimodal distribution of conformations, with little to no preference for left or right-handed twist, unless the single-strand DNA 'tails' are long. The 'flexing' of the DNA invoked by the long single strand regions results in a preferred left-handed conformation. These results are consistent with the positionally dependent structural variation previously observed at the single-strand – double-stranded DNA junction using fluorescent base analogs.[5,6]

We examined the degree of structural disorder of the cyanine dye – DNA systems using the spectral inhomogeneity as an indicator of the extent of the distributions about the ensemble average. We see that for all constructs, dimer and monomer, the inhomogeneity increases with temperature, indicative of thermally populated sub-states in the system. The Cy5 labeled constructs appeared to have less structural variation than the Cy3 systems, indicating that the larger chromophores more readily stacked, however upon elevated

temperatures the structural fluctuations as measured through the spectral inhomogeneity of the two dyes was near equivalent. Additionally, constructs labeled within the double-stranded duplex have a lower amount of spectral inhomogeneity than the constructs labeled at the DNA fork junction, indicative of the positional dependent DNA 'breathing.' Furthermore, the monomer appears to have greater inhomogeneity than the dimer. Possibly a result of the less favorable packing of the monomer with the opposing thymine or lack of opposing base. This less favorable packing of the monomer is supported by molecular dynamics simulations that examined the Cy3 monomer probe fluctuations and found the dye could be positioned external and intercalated into the double-stranded DNA duplex.[7]

The interpretation of the spectral inhomogeneity is model dependent. If additional vibrational modes were considered the increased density of states would result in a decrease in the standard deviation of the inhomogeneous Gaussian function needed approximate the width of the experimentally observed spectra.[2] Likewise, the calculations of the dimer have a greater number of transitions underlying each vibrational band (i.e. 2, 4, 6 transitions for the 0-0, 1-0, and 2-0), while the monomer has a single transition under each vibrational band. If the monomer had an equal number of transitions, it is possible that the magnitude of the optimized inhomogeneous standard deviation would be decreased. While this makes direct comparison of the values suspect, the trends of the increased disorder with temperature and probe position remain valid.

The optimized intramolecular and structural parameters of the cyanine dimer – DNA system indicate that this system could be used as a model system to examine the role of vibronic coherence in electronic energy transfer. Time-resolved 2DFS measurements of the Cy3 dimer labeled deep within the double-stranded duplex of DNA reveal signatures

of coherence, with oscillatory features with frequencies of ~250 cm^{-1} and ~490 cm^{-1}. A ~250 cm^{-1} feature was also observed in the monomer labeled construct, and therefore may be a result of the intramolecular parameters unaccounted for in our model. The narrow laser bandwidth limited our ability to observe a coherence that matched the vibrational mode splitting observed in the absorption spectra as seen in other Cy3 dimer systems.[8,9] Additionally, the corrections applied in our theoretical model to account for the bandwidth of the laser caused ambiguities in the origins of the oscillatory features. The ~490 cm^{-1} feature could be accounted for in two ways. Either as the coherent interaction of the excitonic band with a quasi-resonant vibration, as the 511 cm^{-1} Davydov splitting of the 0-0 feature closely matches the out of plane vibration of a related cyanine dye observed in resonant Raman spectra.[1,10,11] On the other hand it may be the selection of the vibronically coupled features that lie on the blue edge of the 0-0 and red edge of the 1-0 features due to the inhomogeneity of the system overlapped with the narrow laser excitation bandwidth.

Future experiments with the expanded laser bandwidth will be needed to further investigate the origins of these oscillations. By replacing traditional lenses with all reflective optics within the white light path of our home-built non-collinear optical parametric amplifier we are now able to span the vibrational mode of Cy3. Additionally, the laser center frequency can be tuned to the red in order to excite the Cy5 systems which have reduced electronic-vibrational coupling in comparison to Cy3, but approximately equal exciton coupling when labeled within DNA. This suggests that the Cy5 dimer system may be better suited to support delocalized excitons.

APPENDIX A

SUPPLEMENTARY INFORMATION: SPACE FILLING MODELS OF THE CY3 DIMERS

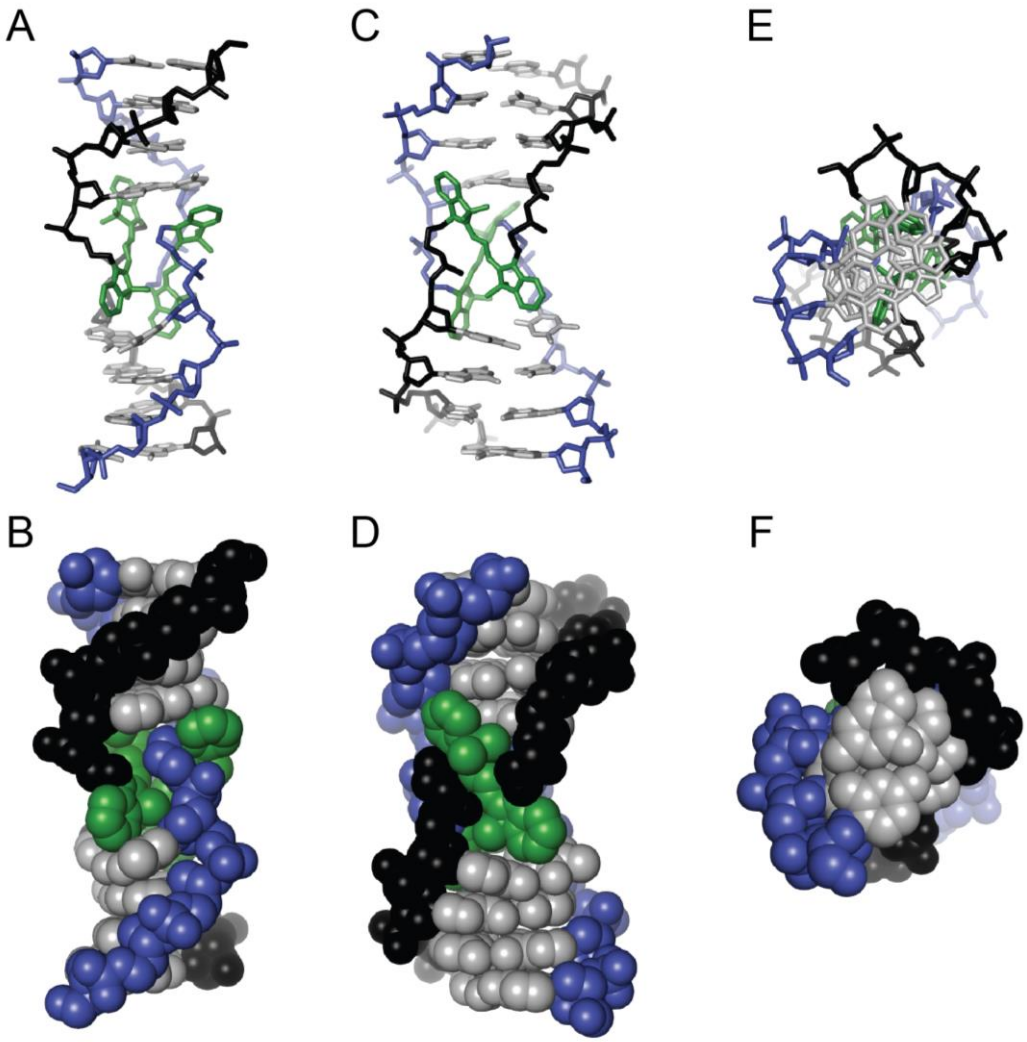

Figure A.1: Ball and stick and space-filling models of the D(Cy3)$_2$ DNA construct calculated using the Spartan program (Wavefunction, Inc.), and further refined using the PyMol program. The models show the D(Cy3)$_2$ chromophore dimer, with approximate D_2 symmetry, within the surrounding bases of the DNA duplex. **(A** & **B)** The construct is shown with an orientation emphasizing the inter-chromophore separation, R_{AB}. **(C** & **D)** The construct is shown with an orientation an emphasizing the inter-chromophore twist angle ϕ_{AB}. **(E** & **F)** The construct is viewed along the axial direction of the DNA duplex.

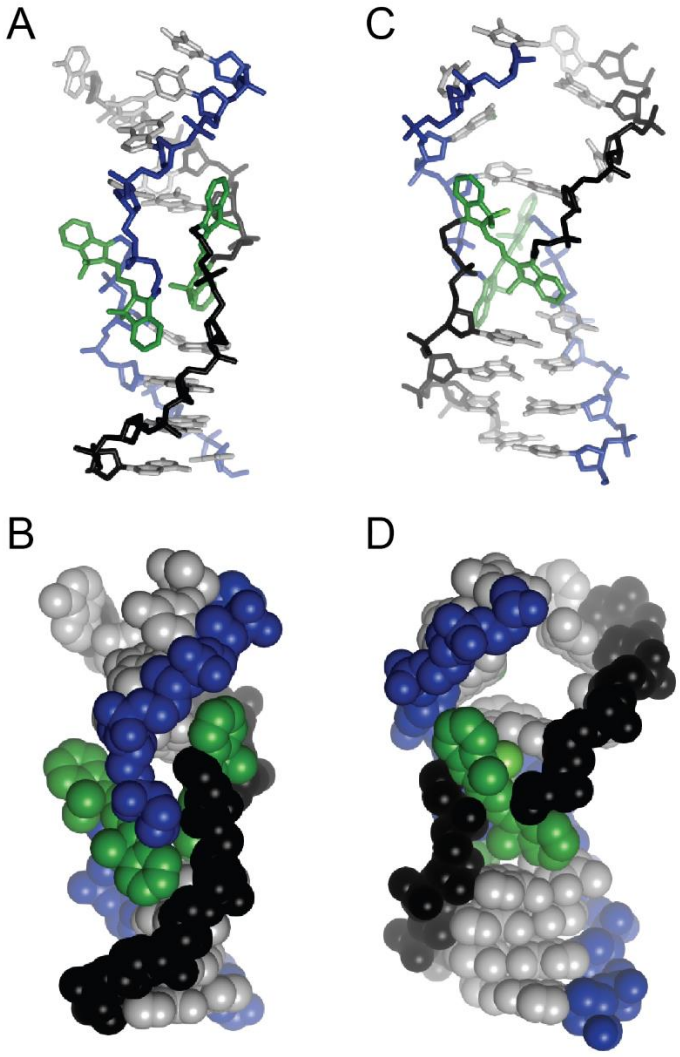

Figure A.2: Ball and stick and space-filling models of the F(Cy3)$_2$ DNA construct calculated using the Spartan program (Wavefunction, Inc.), and further refined using the PyMol program. **(A & B)** The construct is shown with an orientation emphasizing the inter-chromophore separation, R_{AB} and inter-chromophore tilt angle δ_{AB}. **(C & D)** The construct is shown with an orientation an emphasizing the inter-chromophore twist angle ϕ_{AB}.

APPENDIX B

SUPPLEMENTARY INFORMATION: DETERMINATION OF LOCAL CONFORMATIONS OF CONSTRAINED SYSTEMS WITH LINEAR SPECGTROSCOPIC TECHNIQUES

Table B.1: Optimized values of the Hamiltonian parameters of the D(Cy3) monomer DNA construct at various temperatures, obtained from model fits of Eqs. (2.17), (2.2) and (2.3) to the absorption spectra. These optimization calculations used the electric transition dipole moment (EDTM) $\left|\mu_{eg}^{0}\right|$ = 12.8 D, which was determined from integration of the absorption lineshape.[1] The parameters listed are the electronic transition energy ε_{eg}, the vibrational mode frequency ω_0, the Huang-Rhys parameter λ^2, and the standard deviation of the Gaussian disorder function $\sigma_{I,mon}$.

T (°C)	ε_{eg} (cm^{-1})	ω_0 (cm^{-1})	λ^2	$\sigma_{I,mon}$ (cm^{-1})
15	18,285 +40/−39	1,116 +99/−103	0.54 +0.07/−0.06	333 +18/−17
25	18,277 +38/−37	1,109 +88/−90	0.56 +0.06/−0.06	347 +18/−17
35	18,266 +36/−35	1,119 +82/−84	0.56 +0.06/−0.06	353 +18/−17
45	18,262 +36/−35	1,113 +82/−82	0.56 +0.06/−0.05	380 −18/ +17
55	18,280 +39/−38	1,124 +93/−96	0.55 +0.06/−0.06	380 +18/−17
60	18,289 +42/−41	1,107 +95/−98	0.54 +0.07/−0.06	365 +18/−17
65	18,301 +45/−45	1,103 +103/−107	0.54 +0.07/−0.07	367 +18/−17
70	18,308 +44/−43	1,100 +102/−100	0.56 +0.07/−0.06	388 +18/−18
75	18,323 +49/−48	1,072 +120/−120	0.54 +0.08/−0.07	376 +18/−17
85	18,309 +42/−41	1,091 +94/−92	0.56 +0.06/−0.06	399 +18/−17

Table B.2: Optimized values of the Hamiltonian parameters of the D(Cy5) monomer DNA construct at various temperatures, obtained from model fits of Eqs. (2.17), (2.2) and (2.3) to the absorption spectra. These optimization calculations used the electric transition dipole moment (EDTM) $\left|\mu_{eg}^{0}\right|$ = 13.0 D, which was determined from integration of the absorption lineshape.[1] The parameters listed are the electronic transition energy ε_{eg}, the vibrational mode frequency ω_0, the Huang-Rhys parameter λ^2, and the standard deviation of the Gaussian disorder function $\sigma_{I,mon}$.

T (°C)	ε_{eg} (cm^{-1})	ω_0 (cm^{-1})	λ^2	$\sigma_{I,mon}$ (cm^{-1})
15	15,498 +27/−27	1,153 +144/−150	0.25 +0.04/−0.04	315 +12/−11
25	15,500 +26/−26	1,143 +133/−139	0.26 +0.04/−0.04	333 +11/−11
35	15,497 +23/−23	1,208 +118/−120	0.26 +0.04/−0.04	356 +10/−10
45	15,495 +23/−23	1,234 +109/−109	0.28 +0.03/−0.03	383 +10/−9
50	15,494 +22/−22	1,225 +108/−111	0.27 +0.03/−0.03	380 +10/−9
55	15,495 +22/−22	1,246 +109/−108	0.27 +0.03/−0.03	395 +9/−9
60	15,495 +23/−23	1,240 +110/−109	0.28 +0.03/−0.03	402 +10/−9
65	15,507 +22/−22	1,269 +106/−103	0.28 +0.03/−0.03	418 +10/−9
70	15,512 +21/−21	1,265 +97/−95	0.29 +0.03/−0.03	425 +9/−9
75	15,517 +20/−20	1,299 +92/−89	0.29 +0.03/−0.03	447 +9/−8

Table B.3: Davydov splittings of the $0-0$ and $1-0$ vibronic bands of the $D(Cy3)_2$ dimer DNA construct. Experimental values are determined from the energy difference between the optimized upper energy symmetric (+) and lower energy anti-symmetric (–) states within the vibronic band. For the $1-0$ vibronic band, only single-particle states are considered. Theoretical values are determined by the expression $DS_{v_t-0} = 2Je^{-\lambda^2}\lambda^{2v_t}/v_t!$, where v_t phonon occupancy.

T (°C)	J (cm^{-1})	DS_{0-0} (cm^{-1})		DS_{1-0} (cm^{-1})	
		Theory	Experiment	Theory	Experiment
15	529	616	532	333	327
25	514	587	511	329	307
35	497	567	499	318	297
45	483	552	488	309	289
55	467	538	480	296	285
60	449	524	469	283	280
65	362	422	392	228	225

Table B.4: Davydov splittings of the $0-0$ and $1-0$ vibronic bands of the $D(Cy5)_2$ dimer DNA construct. Experimental values are determined from the energy difference between the optimized upper energy symmetric (+) and lower energy anti-symmetric (–) states within the vibronic band. For the $1-0$ vibronic band, only single-particle states are considered. Theoretical values are determined by the expression $DS_{v_t-0} = 2Je^{-\lambda^2}\lambda^{2v_t}/v_t!$, where v_t phonon occupancy.

T (°C)	J (cm^{-1})	DS_{0-0} (cm^{-1})		DS_{1-0} (cm^{-1})	
		Theory	Experiment	Theory	Experiment
15	499	777	682	193	308
25	538	775	676	202	323
35	510	775	685	205	316
45	530	759	676	212	320
55	517	768	685	207	312
65	323	475	455	135	166

Table B.5: Temperature-dependent vibronic band intensity ratios $I_{\pm}^{(0-0)}/I_{\pm}^{(1-0)}$ for the symmetric (+) and anti-symmetric (−) exciton bands of the D(Cy3)$_2$ dimer DNA construct. The temperature-independent vibronic band intensity ratio for the D(Cy3) monomer DNA construct is $I^{(0-0)}/I^{(1-0)}$ = 1.60. The perturbation theory prediction is given by Eq. (16), which assumes that the system resides in the weak exciton-coupling regime (i.e. $|J| \ll \lambda^2\hbar\omega_0$ = 602 cm^{-1}).

T (°C)	J (cm^{-1})	Anti-symmetric exciton (−)		Symmetric exciton (+)	
		Theory	Experiment	Theory	Experiment
15	529	4.31	2.60	0.84	0.62
25	514	4.02	2.47	0.83	0.63
35	497	3.88	2.43	0.82	0.66
45	483	3.81	2.37	0.86	0.68
55	467	3.77	2.36	0.91	0.72
60	449	3.80	2.35	0.94	0.74
65	362	3.29	2.22	1.07	0.88

Table B.6: Temperature-dependent vibronic band intensity ratios $I_{\pm}^{(0-0)}/I_{\pm}^{(1-0)}$ for the symmetric (+) and anti-symmetric (−) exciton bands of the D(Cy5)$_2$ dimer DNA construct. The temperature-independent vibronic band intensity ratio for the D(Cy5) monomer DNA construct is $I^{(0-0)}/I^{(1-0)}$ = 2.95. The perturbation theory prediction is given by Eq. (16), which assumes that the system resides in the weak exciton-coupling regime (i.e. $|J| \ll \lambda^2\hbar\omega_0$ = 335 cm^{-1}).

T (°C)	J (cm^{-1})	Anti-symmetric exciton (−)		Symmetric exciton (+)	
		Theory	Experiment	Theory	Experiment
15	499	10.53	5.50	1.90	0.98
25	538	10.18	5.11	1.79	0.93
35	510	9.44	4.89	1.83	1.01
45	537	8.61	4.48	1.76	1.02
55	517	8.91	4.35	1.84	1.04
65	323	5.84	3.76	2.25	1.64

APPENDIX C

SUPPLEMENTARY INFORMATION: CONFORMATION OF CY3 DIMERS NEAR FORK JUNCTIONS

Table C.1: Optimized values of the Hamiltonian parameters of the Mds monomer DNA construct at various temperatures, obtained from model fits of Eqs. (2.17), (2.2), and (2.3). The parameters listed are the intra-molecular parameters (electronic transition energy ε_{eg}, the vibrational mode frequency ω_0, and the Huang-Rhys parameter λ^2) and the standard deviation of the Gaussian disorder function $\sigma_{I,mon}$.

T (°C)	ε_{eg} (cm^{-1})	ω_0 (cm^{-1})	λ^2	$\sigma_{I,mon}$ (cm^{-1})
10	18,288 +33/-33	1,151 +76/-77	0.58 +0.06/-0.05	365 +14/-13
20	18,278 +33/-33	1,156 +77/-72	0.59 +0.05/-0.05	375 +13/-12
30	18,269 +33/-33	1,155 +75/-71	0.60 +0.05/-0.05	385 +13/-12
40	18,258 +32/-31	1,154 +69/-69	0.60 +0.05/-0.05	396 +13/-12
50	18,247 +31/-31	1,155 +68/-68	0.60 +0.05/-0.05	404 +12/-12
60	18,233 +32/-32	1,152 +70/-69	0.60 +0.05/-0.05	409 +13/-12
70	18,227 +31/-31	1,149 +65/-64	0.61 +0.05/-0.04	430 +12/-11
80	18,230 +33/-33	1,132 +69/-68	0.61 +0.05/-0.05	430 +13/-12
90	18,227 +31/-31	1,136 +64/-63	0.62 +0.04/-0.04	444 +12/-11

Table C.2: Optimized values of the Hamiltonian parameters of the M3 monomer DNA construct at various temperatures, obtained from model fits of Eqs. (2.17), (2.2), and (2.3). The parameters listed are the intra-molecular parameters (electronic transition energy ε_{eg}, the vibrational mode frequency ω_0, and the Huang-Rhys parameter λ^2) and the standard deviation of the Gaussian disorder function $\sigma_{I,mon}$.

T (°C)	ε_{eg} (cm^{-1})	ω_0 (cm^{-1})	λ^2	$\sigma_{I,mon}$ (cm^{-1})
10	18,279 +35/-34	1,132 +81/-81	0.56 +0.06/-0.05	360 +14/-13
20	18,271 +35/-34	1,122 +84/-84	0.55 +0.06/-0.05	356 +14/-13
30	18,277 +39/-38	1,104 +96/-96	0.53 +0.06/-0.06	352 +16/-14
40	18,301 +41/-40	1,101 +99/-98	0.54 +0.07/-0.06	361 +16/-15
50	18,244 +32/-31	1,125 +70/-70	0.57 +0.05/-0.05	393 +12/-12
60	18,222 +32/-32	1,144 +69/-68	0.60 +0.05/-0.05	411 +13/-12
70	18,278 +33/-32	1,134 +70/-69	0.60 +0.05/-0.05	418 +13/-12
80	18,232 +33/-33	1,139 +69/-68	0.61 +0.05/-0.05	434 +13/-12
90	18,230 +32/-31	1,131 +65/-64	0.62 +0.04/-0.04	442 +12/-11

Table C.3: Optimized values of the Hamiltonian parameters of the M2 monomer DNA construct at various temperatures, obtained from model fits of Eqs. (2.17), (2.2), and (2.3). The parameters listed are the intra-molecular parameters (electronic transition energy ε_{eg}, the vibrational mode frequency ω_0, and the Huang-Rhys parameter λ^2) and the standard deviation of the Gaussian disorder function $\sigma_{I,mon}$.

T (°C)	ε_{eg} (cm^{-1})	ω_0 (cm^{-1})	λ^2	$\sigma_{I,mon}$ (cm^{-1})
10	18,246 +35/-34	1,132 +82/-84	0.55 +006/-0.06	350 +14/-13
20	18,241 +34/-33	1,122 +79/-80	0.55 +0.06/-0.05	361 +14/-13
30	18,233 +34/-34	1,126 +77/-78	0.56 +0.05/-0.05	370 +14/-13
40	18,228 +32/-32	1,121 +71/-71	0.57 +0.05/-0.05	385 +13/-12
50	18,224 +32/-31	1,125 +71/-71	0.57 +0.05/-0.05	392 +12/-12
60	18,224 +32/-32	1,116 +69/-69	0.58 +0.05/-0.05	404 +12/-12
70	18,229 +32/-32	1,102 +68/-69	0.58 +0.05/-0.05	411 +12/-12
80	18,235 +34/-33	1,099 +70/-70	0.60 +0.05/-0.05	417 +13/-12
90	18,234 +32/-31	1,099 +65/-64	0.60 +0.05/-0.04	432 +12/-11

Table C.4: Optimized values of the Hamiltonian parameters of the M1 monomer DNA construct at various temperatures, obtained from model fits of Eqs. (2.17), (2.2), and (2.3). The parameters listed are the intra-molecular parameters (electronic transition energy ε_{eg}, the vibrational mode frequency ω_0, and the Huang-Rhys parameter λ^2) and the standard deviation of the Gaussian disorder function $\sigma_{I,mon}$.

T (°C)	ε_{eg} (cm^{-1})	ω_0 (cm^{-1})	λ^2	$\sigma_{I,mon}$ (cm^{-1})
10	18,235 +35/-34	1,142 +83/-84	0.55 +0.06/-0.06	344 +14/-13
20	18,232 +35/-35	1,126 +86/-88	0.54 +0.06/-0.06	343 +15/-13
30	18,234 +37/-36	1,115 +87/-88	0.55 +0.06/-0.06	355 +15/-14
40	18,240 +36/-36	1,119 +83/-84	0.56 +0.06/-0.06	369 +14/-13
50	18,245 +37/-36	1,114 +84/-85	0.56 +0.06/-0.05	372 +14/-13
60	18,249 +37/-36	1,111 +82/-83	0.56 +0.06/-0.05	390 +14/-13
70	18,258 +36/-36	1,114 +79/-79	0.57 +0.05/-0.05	404 +14/-13
80	18,256 +36/-35	1,108 +77/-77	0.58 +0.05/-0.05	409 +14/-13
90	18,250 +34/-34	1,111 +71/-71	0.59 +0.05/-0.05	424 +13/-12

Table C.5: Optimized values of the Hamiltonian parameters of the M-1 monomer DNA construct at various temperatures, obtained from model fits of Eqs. (2.17), (2.2), and (2.3). The parameters listed are the intra-molecular parameters (electronic transition energy ε_{eg}, the vibrational mode frequency ω_0, and the Huang-Rhys parameter λ^2) and the standard deviation of the Gaussian disorder function $\sigma_{I,mon}$.

T (°C)	ε_{eg} (cm^{-1})	ω_0 (cm^{-1})	λ^2	$\sigma_{I,mon}$ (cm^{-1})
10	18,261 +34/-33	1,137 +81/-82	0.55 +0.06/-0.06	338 +14/-13
20	18,260 +35/-34	1,121 +83/-85	0.54 +0.06/-0.06	339 +14/-13
30	18,259 +36/-36	1,127 +87/-89	0.54 +0.06/-0.06	346 +15/-14
40	18,261 +35/-35	1,113 +84/-86	0.54 +0.06/-0.06	354 +14/-13
50	18,260 +35/-35	1,119 +81/-82	0.56 +0.06/-0.05	370 +14/-13
60	18,258 +36/-35	1,118 +80/-80	0.56 +0.05/-0.05	388 +14/-13
70	18,263 +37/-36	1,102 +82/-82	0.57 +0.06/-0.05	398 +14/-13
80	18,262 +35/-34	1,098 +76/-75	0.58 +0.05/-0.05	411 +13/-12
90	18,254 +34/-34	1,103 +72/-72	0.59 +0.05/-0.05	418 +13/-12

Table C.6: Optimized values of the Hamiltonian parameters of the M-2 monomer DNA construct at various temperatures, obtained from model fits of Eqs. (2.17), (2.2), and (2.3). The parameters listed are the intra-molecular parameters (electronic transition energy ε_{eg}, the vibrational mode frequency ω_0, and the Huang-Rhys parameteλ^2r) and the standard deviation of the Gaussian disorder function $\sigma_{I,mon}$.

T (°C)	ε_{eg} (cm^{-1})	ω_0 (cm^{-1})	λ^2	$\sigma_{I,mon}$ (cm^{-1})
10	18,227 +34/-34	1,140 +81/-82	0.55 +0.06/-0.05	356 +14/-13
20	18,219 +35/-35	1,126 +82/-84	0.55 +0.06/-0.06	356 +14/-13
30	18,224 +37/-36	1,110 +87/-88	0.55 +0.06/-0.06	360 +15/-14
40	18,231 +37/-37	1,109 +87/-88	0.55 +0.06/-0.06	369 +15/-14
50	18,241 +37/-36	1,106 +86/-87	0.55 +0.06/-0.05	380 +14/-13
60	18,254 +37/-36	1,109 +83/-82	0.56 +0.06/-0.05	369 +14/-13
70	18,268 +36/-36	1,113 +81/-80	0.57 +0.05/-0.05	408 +14/-13
80	18,269 +36/-35	1,107 +77/-77	0.58 +0.05/-0.05	411 +14/-13
90	18,262 +37/-33	1,115 +73/-72	0.58 +0.05/-0.05	424 +13/-12

Table C.7: The mean optimized values of the intra-molecular parameters for the fork labeled constructs. The parameters listed are the mean electronic transition energy $\bar{\varepsilon}_{eg}$, the vibrational mode frequency $\bar{\omega}_0$, and the Huang-Rhys parameter $\bar{\lambda}^2$.

Construct	$\bar{\varepsilon}_{eg}$ (cm^{-1})	$\bar{\omega}_0$ (cm^{-1})	$\bar{\lambda}^2$
Mds	18,251	1,149	0.60
M3	18,259	1,126	0.58
M2	18,233	1,116	0.57
M1	18,244	1,118	0.56
M-1	18,260	1,115	0.56
M-2	18,244	1,115	0.56

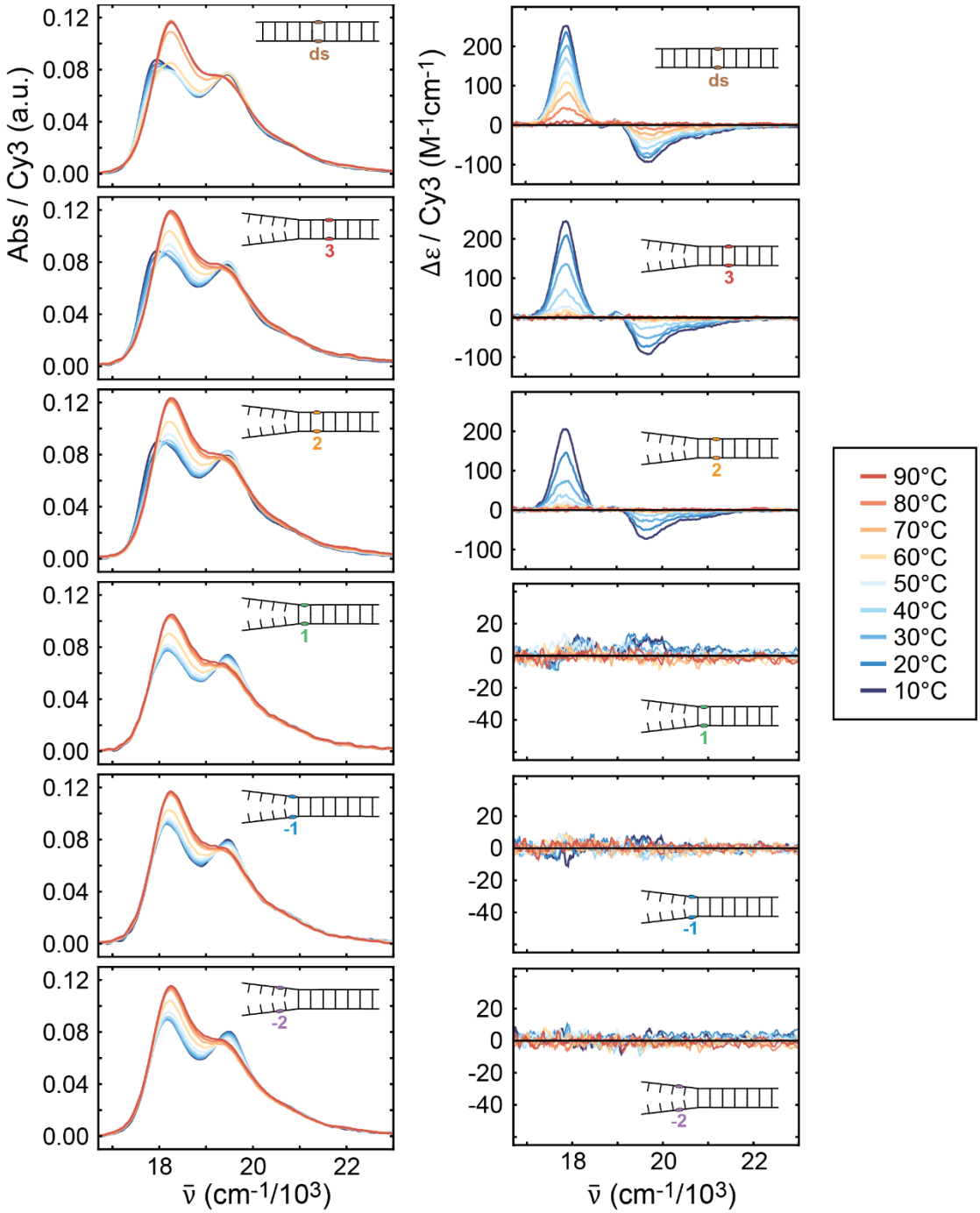

Figure C.1: Temperature dependent absorption and circular dichroism measurements of the Cy3 dimer labeled fork constructs. Blue 10°C - Red 90°C.

Table C.8: Optimized values of the structural parameters of the Dds dimer DNA construct at various temperatures, obtained from the Holstein model fit to absorption and circular dichroism spectra. The intra-molecular parameters were determined from our analyses of the absorption spectra of the Mds monomer DNA construct (see Table C.1). The parameters listed are the inter-chromophore twist angle ϕ_{AB}, the inter-chromophore tilt angle δ_{AB}, the inter-chromophore distance R_{AB}, and the standard deviation of the Gaussian inhomogeneous disorder function $\sigma_{I,dim}$. The error bars were calculated based on a 1% deviation from the range of degenerate conformation parameters.

T (°C)	ϕ_{AB} (°)	δ_{AB} (°)	R_{AB} (Å)	$\sigma_{I,dim}$ (cm^{-1})
10	85.5 -1.1 87.3 +0.2	4.0 -11.8 19.8 +2.8	4.5 -0.2 6.2 +0.2	299 +10/-24
20	83.2 -1.4 85.1 +0.4	0.3 -9.1 19.9 +3.6	5.3 -0.2 6.8 +0.2	309 +10/-22
30	80.6 -1.8 82.6 +0.7	2.7 -14.1 20.0 +4.6	6.2 -0.2 7.4 +0.3	320 +10/-20
40	77.0 -2.2 79.1 +1.0	0.2-13.5 19.8 +5.8	7.1 -0.3 8.1 +0.3	331 +11/-18
50	72.7 -2.6 74.9 +1.6	1.5 -17.6 19.5 +7.4	8.0 -0.3 8.8 +0.4	346 +12/-16
60	68.1 -3.8 70.3 +2.7	0.1 -21.5 18.8 +11.5	9.3 -0.5 10.0 +0.6	368 +12/-15

Table C.9: Optimized values of the structural parameters of the D3 dimer DNA construct at various temperatures, obtained from the Holstein model fit to absorption and circular dichroism spectra. The intra-molecular parameters were determined from our analyses of the absorption spectra of the M3 monomer DNA construct (see Table C.2). The parameters listed are the inter-chromophore twist angle ϕ_{AB}, the inter-chromophore tilt angle δ_{AB}, the inter-chromophore distance R_{AB}, and the standard deviation of the Gaussian inhomogeneous disorder function $\sigma_{I,dim}$. The error bars were calculated based on a 1% deviation from the range of degenerate conformation parameters.

T (°C)	ϕ_{AB} (°)	δ_{AB} (°)	R_{AB} (Å)	$\sigma_{I,dim}$ (cm^{-1})
10	82.3 -1.5 84.3 +0.5	0.1 -9.5 19.8 +3.8	5.6 -0.2 6.9 +0.2	304 +10/-23
20	78.4 -1.9 80.5 +0.8	0.4 -12.4 19.9 +5.0	6.7 -0.2 7.7 +0.3	316 +11/-20
30	73.8 -2.1 76.0 +1.2	0.0 -13.8 19.7 +5.7	7.7 -0.3 8.5 +0.3	326 +11/-15
40	73.8 -1.8 76.1 +1.2	1.1 -14.0 20.0 +5.1	7.8 -0.2 8.7 +0.3	333 +11/-11
50	61.9 -4.2 64.7 +3.7	0.0 -24.0 19.9 +13.1	10.3 -0.5 11.0 +0.7	372 +13/-13
60	56.3 -9.7 120.0 +8.2	0.1 -44.8 20.0 +19.7	12.9 -1.4 14.5 +3.3	401 +14/-13

Table C.10: Optimized values of the structural parameters of the D2 dimer DNA construct at various temperatures, obtained from the Holstein model fit to absorption and circular dichroism spectra. The intra-molecular parameters were determined from our analyses of the absorption spectra of the M2 monomer DNA construct (see Table C.3). The parameters listed are the inter-chromophore twist angle ϕ_{AB}, the inter-chromophore tilt angle δ_{AB}, the inter-chromophore distance R_{AB}, and the standard deviation of the Gaussian inhomogeneous disorder function $\sigma_{I,dim}$. The error bars were calculated based on a 1% deviation from the range of degenerate conformation parameters.

T (°C)	ϕ_{AB} (°)	δ_{AB} (°)	R_{AB} (Å)	$\sigma_{I,dim}$ (cm^{-1})
10	78.8 -2.0 80.9 +0.9	0.3 -12.5 20.0 +5.2	6.7 -0.3 7.8 +0.3	306 +11/-20
20	73.1 -2.4 75.3 +1.5	0.4 -15.4 19.7 +6.6	7.9 -0.3 8.8 +0.3	319 +12/-15
30	67.5 -2.8 70.0 +2.2	0.0 -17.8 19.8 +8.3	9.0 -0.3 9.7 +0.4	334 +12/-13
40	64.2 -3.4 66.8 +2.8	0.1 -20.5 19.5 +10.3	9.7 -0.4 10.3 +0.5	349 +13/-12
50	61.5 -4.4 64.4 +3.8	1.2 -25.7 19.9 +13.5	10.4 -0.5 11.1 +0.8	364 +13/-13
60	58.6 -7.5 118.6 +6.5	0.1 -37.0 20.0 +15.1	11.6 -1.0 13.1 +2.1	385 +14/-13

Table C.11: Optimized values of the structural parameters of the D1 dimer DNA construct at various temperatures, obtained from the Holstein model fit to absorption and circular dichroism spectra. The intra-molecular parameters were determined from our analyses of the absorption spectra of the M1 monomer DNA construct (see Table C.4). The parameters listed are the inter-chromophore twist angle ϕ_{AB}, the inter-chromophore tilt angle δ_{AB}, the inter-chromophore distance R_{AB}, and the standard deviation of the Gaussian inhomogeneous disorder function $\sigma_{I,dim}$. The error bars were calculated based on a 1% deviation from the range of degenerate conformation parameters.

T (°C)	ϕ_{AB} (°)	δ_{AB} (°)	R_{AB} (Å)	$\sigma_{I,dim}$ (cm^{-1})
10	49.0 -6.3 114.0 +2.3	0.8 -21.2 43.5 +7.8	6.0 -0.2 12.2 +0.6	325 +13/-12
20	40.0 -8.8 117.1 +3.0	0.1 -21.4 49.5 +7.6	6.0 -0.2 12.9 +0.6	331 +13/-12
30	41.5 -8.9 115.7 +3.0	0.1 -21.6 50.0 +7.9	6.0 -0.2 12.9 +0.6	337 +13/-13
40	45.9 -7.9 112.5 +2.6	1.6 -22.1 49.9 +7.9	6.0 -0.3 12.9 +0.7	341 +13/-12
50	48.6 -7.9 107.5 +0.8	0.2 -20.6 49.9 +8.3	6.0 -0.3 13.0 +0.8	347 +13/-12
60	58.7 -7.9 108.3 +3.3	0.1 -24.1 41.8 +12.0	6.0 -0.4 13.2 +1.4	365 +13/-12

Table C.12: Optimized values of the structural parameters of the D-1 dimer DNA construct at various temperatures, obtained from the Holstein model fit to absorption and circular dichroism spectra. The intra-molecular parameters were determined from our analyses of the absorption spectra of the M-1 monomer DNA construct (see Table C.5). The parameters listed are the inter-chromophore twist angle ϕ_{AB}, the inter-chromophore tilt angle δ_{AB}, the inter-chromophore distance R_{AB}, and the standard deviation of the Gaussian inhomogeneous disorder function $\sigma_{I,dim}$. The error bars were calculated based on a 1% deviation from the range of degenerate conformation parameters.

T (°C)	ϕ_{AB} (°)	δ_{AB} (°)	R_{AB} (Å)	$\sigma_{I,dim}$ (cm^{-1})
10	52.1 -6.6 108.7 +2.1	0.0 -17.3 50.0 +6.9	6.0 -0.2 12.7 +0.6	309 +12/-11
20	51.7 -6.7 109.3 +2.3	1.1 -16.6 50.0 +7.0	6.0 -0.2 12.6 +0.6	315 +12/-11
30	60.2 -4.8 108.8 +2.2	0.9 -18.5 39.8 +7.3	6.0 -0.2 11.7 +0.6	324 +12/-11
40	53.3 -6.9 106.8 +2.4	0.52 -19.3 48.4 +8.5	6.0 -0.3 12.9 +0.8	345 +12/-12
50	56.4 -7.1 106.8 +2.4	0.5 -19.3 48.4 +8.5	6.0 -0.3 12.9 +0.8	345 +12/-12
60	65.2 -7.0 104.1 +2.2	0.5 -23.3 37.2 +12.3	6.0 -0.4 12.7 +1.6	362 +13/-12

Table C.13: Optimized values of the structural parameters of the D-2 dimer DNA construct at various temperatures, obtained from the Holstein model fit to absorption and circular dichroism spectra. The intra-molecular parameters were determined from our analyses of the absorption spectra of the M-2 monomer DNA construct (see Table C.6). The parameters listed are the inter-chromophore twist angle ϕ_{AB}, the inter-chromophore tilt angle δ_{AB}, the inter-chromophore distance R_{AB}, and the standard deviation of the Gaussian inhomogeneous disorder function $\sigma_{I,dim}$. The error bars were calculated based on a 1% deviation from the range of degenerate conformation parameters.

T (°C)	ϕ_{AB} (°)	δ_{AB} (°)	R_{AB} (Å)	$\sigma_{I,dim}$ (cm^{-1})
10	43.9 -8.6 116.3 +3.3	0.1 -22.2 47.4 +8.4	6.0 -0.3 12.9 +0.7	325 +13/-12
20	41.4 -9.7 117.5 +3.7	0.2 -23.8 47.9 +9.0	6.0 -0.3 13.1 +0.8	336 +14/-13
30	50.6 -10.0 116.2 +3.5	1.1 -24.7 40.3 +0.1	6.0 -0.3 12.38 +0.6	343 +14/-14
40	47.1 -8.4 114.7 +3.5	0.6 -23.8 46.5 +9.5	6.0 -0.3 13.1 +0.8	349 +14/-13
50	52.0 -8.4 111.6 +3.5	0.2 -23.7 46.0 +10.4	6.0 -0.3 13.3 +1.1	359 +13/-12
60	63.9 -8.3 106.3 +4.1	0.6 -26.0 38.6 +14.2	6.0 -0.5 13.4 +2.2	371 +14/-13

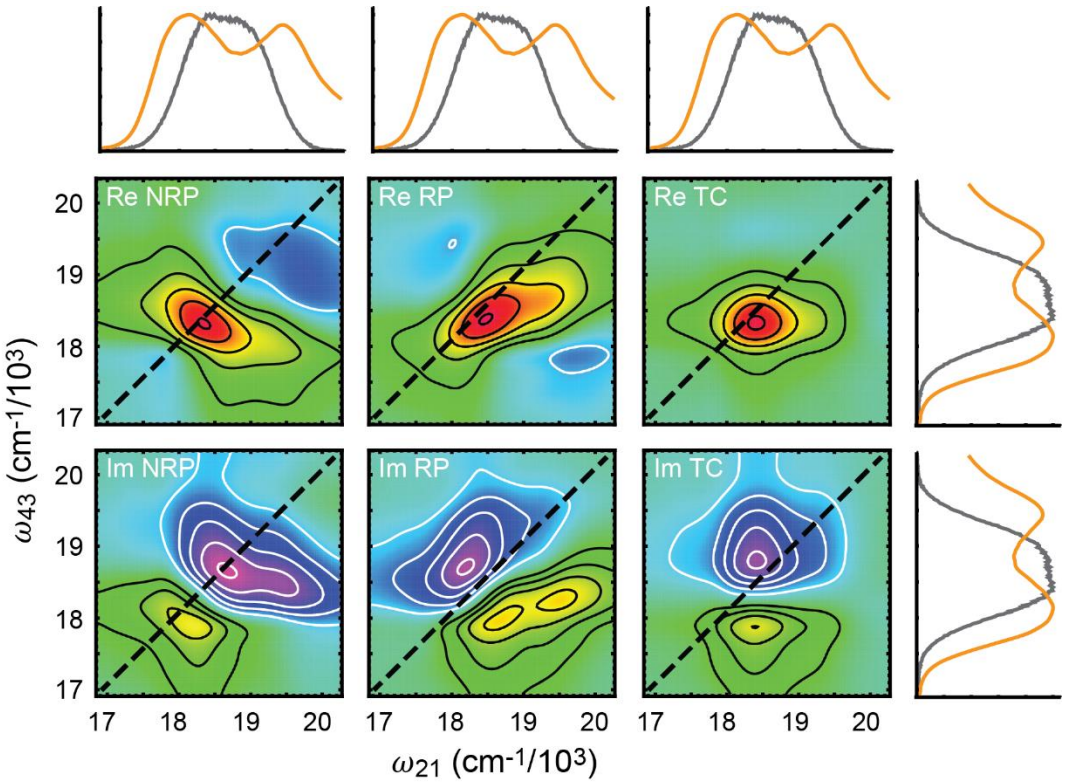

Figure C.2: Experimental two-dimensional fluorescence spectra of the Cy3 dimer labeled construct D2. The real and imaginary components of the non-rephasing (NRP), rephasing (RP) and total correlation spectra (TC) are shown with dashed lines indicating the diagonal. Above and to the right are the absorption (orange) and laser spectra (gray) over the spectral region investigated.

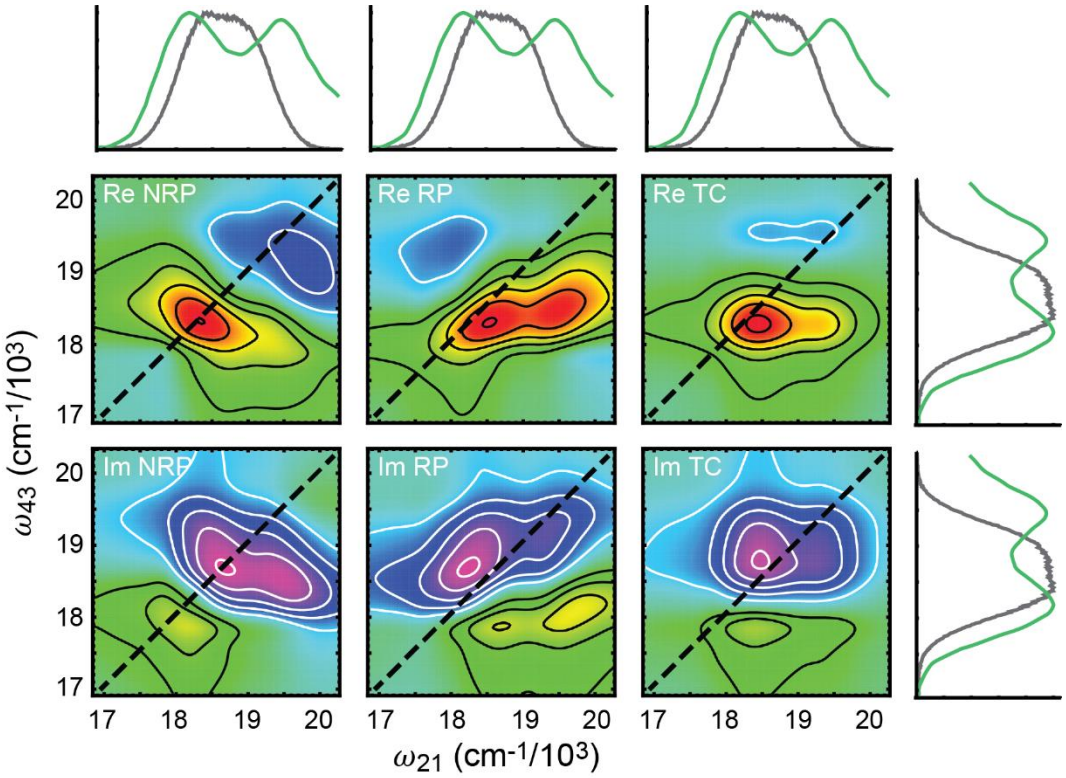

Figure C.3: Experimental two-dimensional fluorescence spectra of the Cy3 dimer labeled construct D1. The real and imaginary components of the non-rephasing (NRP), rephasing (RP) and total correlation spectra (TC) are shown with dashed lines indicating the diagonal. Above and to the right are the absorption (green) and laser spectra (gray) over the spectral region investigated.

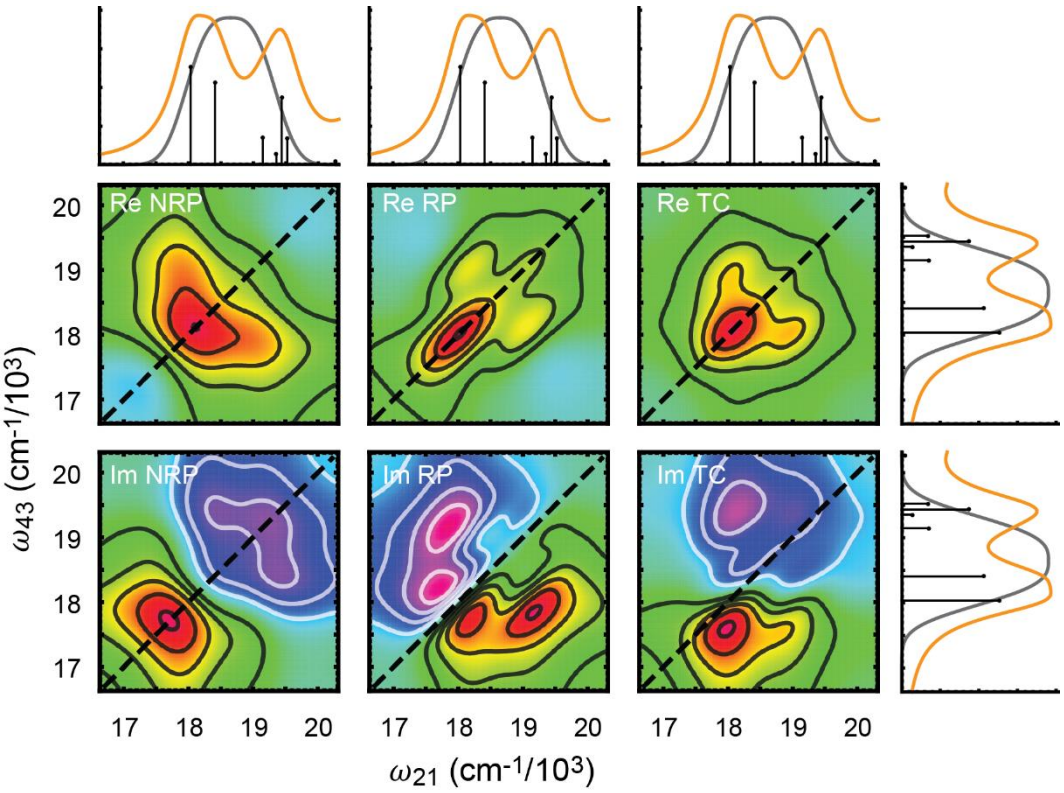

Figure C.4: Calculated two-dimensional fluorescence spectra of the Cy3 dimer labeled construct D2. The real and imaginary components of the non-rephasing (NRP), rephasing (RP) and total correlation spectra (TC) are shown with dashed lines indicating the diagonal. Above and to the right are the calculated absorption (orange), underlying stick transitions (black), and simulated laser spectra (gray) over the spectral region investigated. Structural parameters were inter-chromophore twist angle $\phi_{AB} = 79.6°$, inter-chromophore tilt angle $\delta_{AB} = 8.5°$, and inter-chromophore separation $R_{AB} = 7.7$ Å

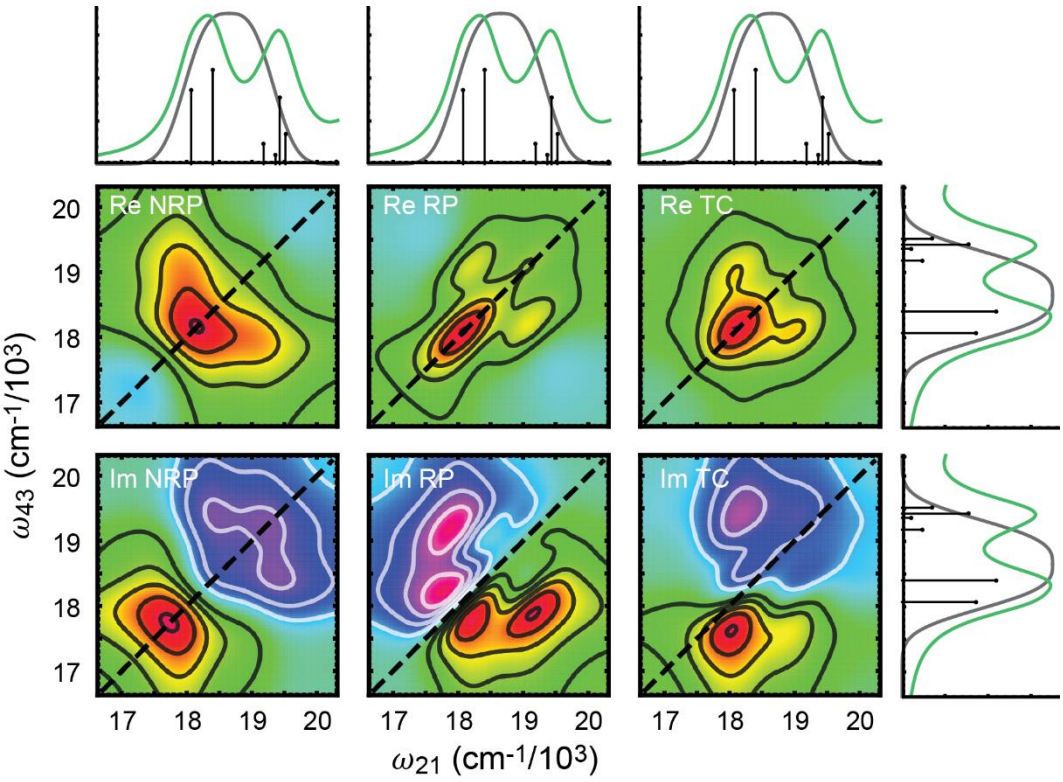

Figure C.5: Calculated two-dimensional fluorescence spectra of the Cy3 dimer labeled construct D1. The real and imaginary components of the non-rephasing (NRP), rephasing (RP) and total correlation spectra (TC) are shown with dashed lines indicating the diagonal. Above and to the right are the calculated absorption (green), underlying stick transitions (black), and simulated laser spectra (gray) over the spectral region investigated. Structural parameters were inter-chromophore twist angle $\phi_{AB} = 105.3°$, inter-chromophore tilt angle $\delta_{AB} = 34.4°$, and inter-chromophore separation $R_{AB} = 5.63$ Å

APPENDIX D

SUPPLEMENTARY INFORMATION: EXCITED STATE DYNAMICS OF CY3 DIMERS

The oscillatory features of the non-rephasing 2D spectra were fit using a sum of damped sine waves. This was done either by fitting the amplitude directly given the:

$$y = y_0 + A_{tot} \exp\left[{-t_{32}}/{\tau_{tot}}\right] + \sum_{i=1}^{2} A_i \exp\left[{-t_{32}}/{\tau_i}\right] \sin(\omega_i t_{32} + \varphi_i) \quad \text{(D.1)}$$

Or the non-oscillatory decay was first removed, and the resulting oscillatory features fit using equation D.3

$$y = y_0 + A_{tot} \exp\left[{-t_{32}}/{\tau_{tot}}\right] \quad \text{(D.2)}$$

$$y = \sum_{i=1}^{2} A_i \exp\left[{-t_{32}}/{\tau_i}\right] \sin(\omega_i t_{32} + \varphi_i) \quad \text{(D.3)}$$

where A_{tot} and A_i are the amplitudes, τ_{tot} is the dephasing time, τ_i is the damping time, ω_i is the frequency, and φ_i is the phase of the oscillation.

The fit parameters for both methods are presented in Table D.1, the color names correspond to the plot colors used in Chapter VII, and blue examines the negative feature while red examines the positive feature of the NRP spectrum.

Table D.1: Fit parameters for the time resolved point amplitudes taken from the real part of the non-rephasing spectrum

	Blue – (D.1)	Blue – (D.2 & D.3)	Red – (D.1)	Red – (D.2 & D.3)
y_0	0.24	0.24	-0.17	-0.18
A_{tot}	-0.23	0.23	0.17	0.17
τ_{tot}	185	192	158	181
A_1	0.023	0.022	0.023	-0.014
τ_1	200	200	100	200
ω_1	256	250	252	249
φ_1	-5.03	1.39	-1.76	1.52
A_2	0.028	-0.028	0.021	-0.020
τ_2	209	223	205	247
ω_2	488	489	487	483
φ_2	-1.88	-5.04	1.35	-1.70

REFERENCES CITED

CHAPTER I

[1] P.H. von Hippel, N.P. Johnson, and A.H. Marcus, "Fifty years of DNA 'Breathing': Reflections on old and new approaches," Biopolymers **99**, 923 (2013).

[2] D. Jose, K. Datta, N.P. Johnson, and P.H. von Hippel, "Spectroscopic studies of position-specific DNA 'breathing' fluctuations at replication forks and primer-template junctions.," Proc. Natl. Acad. Sci. U. S. A. **106**, 4231 (2009).

[3] D. Jose, S.E. Weitzel, and P.H. von Hippel, "Breathing fluctuations in position-specific DNA base pairs are involved in regulating helicase movement into the replication fork," Proc. Natl. Acad. Sci. **109**, 14428 (2012).

[4] C. Phelps, W. Lee, D. Jose, P.H. von Hippel, and A.H. Marcus, "Single-molecule FRET and linear dichroism studies of DNA breathing and helicase binding at replication fork junctions," Proc. Natl. Acad. Sci. **110**, 17320 (2013).

[5] K. Datta, N.P. Johnson, G. Villani, A.H. Marcus, and P.H. Von Hippel, "Characterization of the 6-methyl isoxanthopterin (6-MI) base analog dimer, a spectroscopic probe for monitoring guanine base conformations at specific sites in nucleic acids," Nucleic Acids Res. **40**, 1191 (2012).

[6] K. Datta, N.P. Johnson, and P.H. von Hippel, "DNA conformational changes at the primer-template junction regulate the fidelity of replication by DNA polymerase.," Proc. Natl. Acad. Sci. U. S. A. **107**, 17980 (2010).

[7] M. Levitus and S. Ranjit, "Cyanine dyes in biophysical research: the photophysics of polymethine fluorescent dyes in biomolecular environments.," Q. Rev. Biophys. **44**, 123 (2011).

[8] M.E. Sanborn, B.K. Connolly, K. Gurunathan, and M. Levitus, "Fluorescence properties and photophysics of the sulfoindocyanine Cy3 linked covalently to DNA," J. Phys. Chem. B **111**, 11064 (2007).

[9] A. Mishra, R.K. Behera, P.K. Behera, B.K. Mishra, and G.B. Behera, "Cyanines during the 1990s: a review," Chem. Rev. **100**, 1973 (2000).

[10] F. Würthner, T.E. Kaiser, and C.R. Saha-Möller, "J-aggregates: From serendipitous discovery to supramolecular engineering of functional dye materials," Angew. Chemie - Int. Ed. **50**, 3376 (2011).

[11] U. Resch-Genger, M. Grabolle, S. Cavaliere-Jaricot, R. Nitschke, and T. Nann, "Quantum dots versus organic dyes as fluorescent labels," Nat. Methods **5**, 763 (2008).

[12] W. Lee, D. Jose, C. Phelps, A.H. Marcus, and P.H. Von Hippel, "A single-molecule view of the assembly pathway, subunit stoichiometry, and unwinding activity of the bacteriophage T4 primosome (helicase-primase) complex," Biochemistry **52**, 3157 (2013).

[13] W. Lee, P.H. Von Hippel, and A.H. Marcus, "Internally labeled Cy3/Cy5 DNA constructs show greatly enhanced photo-stability in single-molecule FRET experiments," Nucleic Acids Res. **42**, 5967 (2014).

[14] E. Collini, C.Y. Wong, K.E. Wilk, P.M.G. Curmi, P. Brumer, and G.D. Scholes, "Coherently wired light-harvesting in photosynthetic marine algae at ambient temperature.," Nature **463**, 644 (2010).

[15] A. Chenu and G.D. Scholes, "Coherence in Energy Transfer and Photosynthesis," Annu. Rev. Phys. Chem. **66**, 69 (2014).

[16] F. Milota, V.I. Prokhorenko, T. Mancal, H. Berlepsch, H.F. Kauffmann, and J. Hauer, "Vibronic and Vibrational Coherences in Two- Dimensional Electronic Spectra of Supramolecular J-A ggregates," J. Phys. Chem. A 6007 (2013).

[17] S.M. Blau, D.I.G. Bennett, C. Kreisbeck, G.D. Scholes, and A. Aspuru-Guzik, "Local protein solvation drives direct down-conversion in phycobiliprotein PC645 via incoherent vibronic transport," ArXiv:1704.05449v1 (2017).

[18] G.S. Engel, T.R. Calhoun, E.L. Read, T.K. Ahn, T. Mančal, Y.C. Cheng, R.E. Blankenship, and G.R. Fleming, "Evidence for wavelike energy transfer through quantum coherence in photosynthetic systems," Nature **446**, 782 (2007).

[19] E. Romero, R. Augulis, V.I. Novoderezhkin, M. Ferretti, J. Thieme, D. Zigmantas, and R. van Grondelle, "Quantum coherence in photosynthesis for efficient solar-energy conversion," Nat. Phys. **10**, 676 (2014).

[20] F.D. Fuller, J. Pan, A. Gelzinis, V. Butkus, S.S. Senlik, D.E. Wilcox, C.F. Yocum, L. Valkunas, D. Abramavicius, and J.P. Ogilvie, "Vibronic coherence in oxygenic photosynthesis," Nat. Chem. **6**, 706 (2014).

[21] V. Tiwari, W.K. Peters, and D.M. Jonas, "Electronic resonance with anticorrelated pigment vibrations drives photosynthetic energy transfer outside the adiabatic framework.," Proc. Natl. Acad. Sci. U. S. A. **110**, 1203 (2013).

[22] A. Halpin, P.J.M. Johnson, R. Tempelaar, R.S. Murphy, J. Knoester, T.L.C. Jansen, and R.J.D. Miller, "Two-dimensional spectroscopy of a molecular dimer unveils the effects of vibronic coupling on exciton coherences.," Nat. Chem. **6**, 196 (2014).

[23] H.-G. Duan, P. Nalbach, V.I. Prokhorenko, S. Mukamel, and M. Thorwart, "On the origin of oscillations in two-dimensional spectra of excitonically-coupled molecular systems," New J. Phys. **17**, 072002 (2015).

[24] J. Lim, D. Paleček, F. Caycedo-Soler, C.N. Lincoln, J. Prior, H. von Berlepsch, S.F. Huelga, M.B. Plenio, D. Zigmantas, and J. Hauer, "Vibronic origin of long-lived coherence in an artificial molecular light harvester," Nat. Commun. **6**, 7755 (2015).

[25] L. Kringle, N.P.D. Sawaya, J. Widom, C. Adams, M.G. Raymer, A. Aspuru-Guzik, and A.H. Marcus, "Temperature-dependent conformations of exciton-coupled Cy3 dimers in double-stranded DNA," J. Chem. Phys. **148**, 085101 (2018).

CHAPTER II

[1] W. West and S. Pearce, "The dimeric state of cyanine dyes," J. Phys. Chem. **566**, 1894 (1965).

[2] W. West, S.P. Lovell, and W. Cooper, "Electronic Spectra of Cyanine Dyes at Low Temperature: Part I. Monomeric and Aggregate Absorption Spectra," Photogr. Sci. Eng. **14**, 52 (1970).

[3] A. Mishra, R.K. Behera, P.K. Behera, B.K. Mishra, and G.B. Behera, "Cyanines during the 1990s: a review," Chem. Rev. **100**, 1973 (2000).

[4] L.I. Markova, V.L. Malinovskii, L.D. Patsenker, and R. Häner, "J- vs. H-type assembly: pentamethine cyanine (Cy5) as a near-IR chiroptical reporter.," Chem. Commun. (Camb). **49**, 5298 (2013).

[5] F. Nicoli, M.K. Roos, E.A. Hemmig, M. Di Antonio, R. de Vivie-Riedle, and T. Liedl, "Proximity-Induced H-Aggregation of Cyanine Dyes on DNA-Duplexes," J. Phys. Chem. A **120**, 9941 (2016).

[6] B.L. Cannon, D.L. Kellis, L.K. Patten, P.H. Davis, J. Lee, E. Graugnard, B. Yurke, and W.B. Knowlton, "Coherent Exciton Delocalization in a Two-State DNA-Templated Dye Aggregate System," J. Phys. Chem. A **121**, 6905 (2017).

[7] B.L. Cannon, L.K. Patten, D.L. Kellis, P.H. Davis, J. Lee, E. Graugnard, B. Yurke, and W.B. Knowlton, "Large Davydov Splitting and Strong Fluorescence Suppression: An Investigation of Exciton Delocalization in DNA-Templated Holliday Junction Dye Aggregates," J. Phys. Chem. A **122**, 2086 (2018).

[8] T. Forster, *Delocalized Excitation and Excitation Transfer, Bulletin No. 18, Division of Biology and Medicine U.S. Atomic Energy Commission* (Florida State University, Talahassee, Florida, 1965).

[9] M. Kasha, H.R. Rawls, and M. Ashraf El-Bayoumi, "The exciton model in molecular spectroscopy," Pure Appl. Chem. **11**, 371 (1965).

[10] R.L. Fulton and M. Gouterman, "Vibronic Coupling . I . Mathematical Treatment for Two Electronic States," J. Chem. Phys. **35**, 1059 (1961).

[11] R.L. Fulton and M. Gouterman, "Vibronic Coupling. II. Spectra of Dimers," J. Chem. Phys. **41**, 2280 (1964).

[12] F. Würthner, T.E. Kaiser, and C.R. Saha-Möller, "J-aggregates: From serendipitous discovery to supramolecular engineering of functional dye materials," Angew. Chemie - Int. Ed. **50**, 3376 (2011).

[13] A. Halpin, P.J.M. Johnson, R. Tempelaar, R.S. Murphy, J. Knoester, T.L.C. Jansen, and R.J.D. Miller, "Two-dimensional spectroscopy of a molecular dimer unveils the effects of vibronic coupling on exciton coherences.," Nat. Chem. **6**, 196 (2014).

[14] H.-G. Duan, P. Nalbach, V.I. Prokhorenko, S. Mukamel, and M. Thorwart, "On the origin of oscillations in two-dimensional spectra of excitonically-coupled molecular systems," New J. Phys. **17**, 072002 (2015).

[15] M. Levitus and S. Ranjit, "Cyanine dyes in biophysical research: the photophysics of polymethine fluorescent dyes in biomolecular environments.," Q. Rev. Biophys. **44**, 123 (2011).

[16] M.E. Sanborn, B.K. Connolly, K. Gurunathan, and M. Levitus, "Fluorescence properties and photophysics of the sulfoindocyanine Cy3 linked covalently to DNA," J. Phys. Chem. B **111**, 11064 (2007).

[17] A. Eisfeld, L. Braun, W.T. Strunz, J.S. Briggs, J. Beck, and V. Engel, "Vibronic energies and spectra of molecular dimers," J. Chem. Phys. **122**, 134103 (2005).

[18] V. Tiwari, W.K. Peters, and D.M. Jonas, "Electronic resonance with anticorrelated pigment vibrations drives photosynthetic energy transfer outside the adiabatic framework.," Proc. Natl. Acad. Sci. U. S. A. **110**, 1203 (2013).

[19] S. Mukamel, *Principles of Nonlinear Optical Spectroscopy* (Oxford University Press, Oxford, 1995).

[20] L. Valkunas, D. Abramavicius, and T. Mancal, *Molecular Excitation Dynamics and Relaxation* (Wiley-VHC, Weinheim, 2013).

[21] H. Dong and G.R. Fleming, "Inhomogeneous broadening induced long-lived integrated two-color coherence photon echo signal," J. Phys. Chem. B **118**, 8956 (2014).

[22] H. van Amerongen, L. Valkunas, and R. van Grondelle, *Photosynthetic Excitons* (World Scientific, Singapore, 2000).

[23] A. Perdomo-Ortiz, J.R. Widom, G.A. Lott, A. Aspuru-Guzik, and A.H. Marcus, "Conformation and electronic population transfer in membrane-supported self-assembled porphyrin dimers by 2D fluorescence spectroscopy," J. Phys. Chem. B **116**, 10757 (2012).

[24] K.A. Kistler, C.M. Pochas, H. Yamagata, S. Matsika, and F.C. Spano, "Absorption, circular dichroism, and photoluminescence in perylene diimide bichromophores: Polarization-dependent H- and J-aggregate behavior," J. Phys. Chem. B **116**, 77 (2012).

[25] F. Sánchez-Bajo and F.L. Cumbrera, "The Use of the Pseudo-Voigt Function in the Variance Method of X-ray Line-Broadening Analysis," J. Appl. Crystallogr. **30**, 427 (1997).

[26] J.R. Widom, W. Lee, A. Perdomo-Ortiz, D. Rappoport, T.F. Molinski, A. Aspuru-Guzik, and A.H. Marcus, "Temperature-dependent conformations of a membrane supported zinc porphyrin tweezer by 2D fluorescence spectroscopy," J. Phys. Chem. A **117**, 6171 (2013).

[27] J.R. Widom, N.P. Johnson, P.H. Von Hippel, and A.H. Marcus, "Solution conformation of 2-aminopurine dinucleotide determined by ultraviolet two-dimensional fluorescence spectroscopy," New J. Phys. **15**, 025028 (2013).

[28] P.F. Tekavec, G.A. Lott, and A.H. Marcus, "Fluorescence-detected two-dimensional electronic coherence spectroscopy by acousto-optic phase modulation," J. Chem. Phys. **127**, 214307 (2007).

[29] G.A. Lott, A. Perdomo-Ortiz, J.K. Utterback, J.R. Widom, A. Aspuru-Guzik, and A.H. Marcus, "Conformation of self-assembled porphyrin dimers in liposome vesicles by phase-modulation 2D fluorescence spectroscopy," Proc. Natl. Acad. Sci. **108**, 16521 (2011).

[30] K.J. Karki, J.R. Widom, J. Seibt, I. Moody, M.C. Lonergan, T. Pullerits, and A.H. Marcus, "Coherent two-dimensional photocurrent spectroscopy in a PbS quantum dot photocell," Nat. Commun. **5**, 5869 (2014).

[31] M. Cho, *Two-Dimensional Optical Spectroscopy* (CRC Press, Boca Raton, 2009).

[32] O. Golonzka and A. Tokmakoff, "Polarization-selective third-order spectroscopy of coupled vibronic states," J. Chem. Phys. **115**, 297 (2001).

[33] P. Grégoire, A.R. Srimath Kandada, E. Vella, C. Tao, R. Leonelli, and C. Silva, "Incoherent population mixing contributions to phase-modulation two-dimensional coherent excitation spectra," J. Chem. Phys. **147**, 114201 (2017).

[34] G.B. Arfken, *Mathematical Methods for Physicists*, 3rd ed. (Academic Press, Orlando, 1985).

[35] R.N. Bracewell, *The Fourier Transform and Its Applications*, 3rd ed. (McGraw-Hill, New York, 1999).

CHAPTER III

[1] D. Jose, S.E. Weitzel, and P.H. von Hippel, "Breathing fluctuations in position-specific DNA base pairs are involved in regulating helicase movement into the replication fork," Proc. Natl. Acad. Sci. **109**, 14428 (2012).

[2] D. Jose, K. Datta, N.P. Johnson, and P.H. von Hippel, "Spectroscopic studies of position-specific DNA 'breathing' fluctuations at replication forks and primer-template junctions.," Proc. Natl. Acad. Sci. U. S. A. **106**, 4231 (2009).

[3] P.F. Tekavec, G.A. Lott, and A.H. Marcus, "Fluorescence-detected two-dimensional electronic coherence spectroscopy by acousto-optic phase modulation," J. Chem. Phys. **127**, 214307 (2007).

[4] G.A. Lott, A. Perdomo-Ortiz, J.K. Utterback, J.R. Widom, A. Aspuru-Guzik, and A.H. Marcus, "Conformation of self-assembled porphyrin dimers in liposome vesicles by phase-modulation 2D fluorescence spectroscopy," Proc. Natl. Acad. Sci. **108**, 16521 (2011).

[5] A. Perdomo-Ortiz, J.R. Widom, G.A. Lott, A. Aspuru-Guzik, and A.H. Marcus, "Conformation and electronic population transfer in membrane-supported self-assembled porphyrin dimers by 2D fluorescence spectroscopy," J. Phys. Chem. B **116**, 10757 (2012).

[6] J.R. Widom, W. Lee, A. Perdomo-Ortiz, D. Rappoport, T.F. Molinski, A. Aspuru-Guzik, and A.H. Marcus, "Temperature-dependent conformations of a membrane supported zinc porphyrin tweezer by 2D fluorescence spectroscopy," J. Phys. Chem. A **117**, 6171 (2013).

[7] J.R. Widom, N.P. Johnson, P.H. Von Hippel, and A.H. Marcus, "Solution conformation of 2-aminopurine dinucleotide determined by ultraviolet two-dimensional fluorescence spectroscopy," New J. Phys. **15**, 025028 (2013).

[8] K.J. Karki, J.R. Widom, J. Seibt, I. Moody, M.C. Lonergan, T. Pullerits, and A.H. Marcus, "Coherent two-dimensional photocurrent spectroscopy in a PbS quantum dot photocell," Nat. Commun. **5**, 5869 (2014).

[9] G. Cerullo and S. De Silvestri, "Ultrafast optical parametric amplifiers," Rev. Sci. Instrum. **74**, 1 (2003).

[10] C. Manzoni, D. Polli, and G. Cerullo, "Two-color pump-probe system broadly tunable over the visible and the near infrared with sub-30 fs temporal resolution," Rev. Sci. Instrum. **77**, 023103 (2006).

[11] M. Müller, J. Squier, R. Wolleschensky, U. Simon, and G.J. Brakenhoff, "Dispersion pre-compensation of 15 femtosecond optical pulses for high-numerical-aperture objectives," J. Microsc. **191**, 141 (1998).

[12] H. van Amerongen, L. Valkunas, and R. van Grondelle, *Photosynthetic Excitons* (World Scientific, Singapore, 2000).

[13] C. Phelps, B. Israels, D. Jose, M.C. Marsh, P.H. von Hippel, and A.H. Marcus, "Using microsecond single-molecule FRET to determine the assembly pathways of T4 ssDNA binding protein onto model DNA replication forks," Proc. Natl. Acad. Sci. **114**, E3612 (2017).

[14] R.H. Byrd, J. Nocedal, and R.A. Waltz, in *KNITRO: An Integrated Package for Nonlinear Optimization* (Springer-Verlag, Berlin, 2006), pp. 35–59.

CHAPTER IV

[1] R.E. Merrifield, "Vibronic states of dimers," Radiat. Res. **20**, 154 (1963).

[2] T. Forster, *Delocalized Excitation and Excitation Transfer, Bulletin No. 18, Division of Biology and Medicine U.S. Atomic Energy Commission* (Florida State University, Talahassee, Florida, 1965).

[3] E. Charney, *The Molecular Basis of Optical Activity: Optical Rotatory Dispersion and Circular Dichroism* (John Wiley & Sons, New York, 1979).

[4] W. Domcke, H. Koppel, and L.S. Cederbaum, "Spectroscopic effects of conical intersections of molecular potential energy surfaces," Mol. Phys. **43**, 851 (1981).

[5] A. Eisfeld, L. Braun, W.T. Strunz, J.S. Briggs, J. Beck, and V. Engel, "Vibronic energies and spectra of molecular dimers," J. Chem. Phys. **122**, 134103 (2005).

[6] A. Eisfeld, J. Seibt, and V. Engel, "On the inversion of geometric parameters from absorption and circular dichroism spectroscopy of molecular dimers," Chem. Phys. Lett. **467**, 186 (2008).

[7] F.C. Spano, "The spectral signatures of frenkel polarons in H-and J-aggregates," Acc. Chem. Res. **43**, 429 (2009).

[8] K.A. Kistler, C.M. Pochas, H. Yamagata, S. Matsika, and F.C. Spano, "Absorption, circular dichroism, and photoluminescence in perylene diimide bichromophores: Polarization-dependent H- and J-aggregate behavior," J. Phys. Chem. B **116**, 77 (2012).

[9] S. Polyutov, O. Kühn, and T. Pullerits, "Exciton-vibrational coupling in molecular aggregates: Electronic versus vibronic dimer," Chem. Phys. **394**, 21 (2012).

[10] V. Tiwari, W.K. Peters, and D.M. Jonas, "Electronic resonance with anticorrelated pigment vibrations drives photosynthetic energy transfer outside the adiabatic framework.," Proc. Natl. Acad. Sci. U. S. A. **110**, 1203 (2013).

[11] A. Halpin, P.J.M. Johnson, R. Tempelaar, R.S. Murphy, J. Knoester, T.L.C. Jansen, and R.J.D. Miller, "Two-dimensional spectroscopy of a molecular dimer unveils the effects of vibronic coupling on exciton coherences.," Nat. Chem. **6**, 196 (2014).

[12] H.-G. Duan, P. Nalbach, V.I. Prokhorenko, S. Mukamel, and M. Thorwart, "On the origin of oscillations in two-dimensional spectra of excitonically-coupled molecular systems," New J. Phys. **17**, 072002 (2015).

[13] J. Lim, D. Paleček, F. Caycedo-Soler, C.N. Lincoln, J. Prior, H. von Berlepsch, S.F. Huelga, M.B. Plenio, D. Zigmantas, and J. Hauer, "Vibronic origin of long-lived coherence in an artificial molecular light harvester," Nat. Commun. **6**, 7755 (2015).

[14] M. Kasha, H.R. Rawls, and M. Ashraf El-Bayoumi, "The exciton model in molecular spectroscopy," Pure Appl. Chem. **11**, 371 (1965).

[15] R.L. Fulton and M. Gouterman, "Vibronic Coupling. II. Spectra of Dimers," J. Chem. Phys. **41**, 2280 (1964).

[16] R.L. Fulton and M. Gouterman, "Vibronic Coupling . I . Mathematical Treatment for Two Electronic States," J. Chem. Phys. **35**, 1059 (1961).

[17] L. Valkunas, D. Abramavicius, and T. Mancal, *Molecular Excitation Dynamics and Relaxation* (Wiley-VHC, Weinheim, 2013).

[18] T. Azumi and K. Matsuzaki, "What does the term "vibronic coupling' mean?," Photochem. Photobiol. **25**, 315 (1977).

[19] G. Fischer, *Vibronic Coupling: The Interaction Between the Electronic and Nuclear Motions* (Academic Press, London, 1984).

[20] E. Collini, C.Y. Wong, K.E. Wilk, P.M.G. Curmi, P. Brumer, and G.D. Scholes, "Coherently wired light-harvesting in photosynthetic marine algae at ambient temperature.," Nature **463**, 644 (2010).

[21] A. Chenu and G.D. Scholes, "Coherence in Energy Transfer and Photosynthesis," Annu. Rev. Phys. Chem. **66**, 69 (2014).

[22] S.M. Blau, D.I.G. Bennett, C. Kreisbeck, G.D. Scholes, and A. Aspuru-Guzik, "Local protein solvation drives direct down-conversion in phycobiliprotein PC645 via incoherent vibronic transport," ArXiv:1704.05449v1 (2017).

[23] G.S. Engel, T.R. Calhoun, E.L. Read, T.K. Ahn, T. Mančal, Y.C. Cheng, R.E. Blankenship, and G.R. Fleming, "Evidence for wavelike energy transfer through quantum coherence in photosynthetic systems," Nature **446**, 782 (2007).

[24] E. Romero, R. Augulis, V.I. Novoderezhkin, M. Ferretti, J. Thieme, D. Zigmantas, and R. van Grondelle, "Quantum coherence in photosynthesis for efficient solar-energy conversion," Nat. Phys. **10**, 676 (2014).

[25] H.-G. Duan, V.I. Prokhorenko, R.J. Cogdell, K. Ashraf, A.L. Stevens, M. Thorwart, and R.J.D. Miller, "Nature does not rely on long-lived electronic quantum coherence for photosynthetic energy transfer," Proc. Natl. Acad. Sci. **114**, 8493 (2017).

[26] N. Killoran, S.F. Huelga, and M.B. Plenio, "Enhancing light-harvesting power with coherent vibrational interactions: A quantum heat engine picture," J. Chem. Phys. **143**, 155102 (2015).

[27] M. Mohseni, P. Rebentrost, S. Lloyd, and A. Aspuru-Guzik, "Environment-assisted quantum walks in photosynthetic energy transfer," J. Chem. Phys. **129**, 174106 (2008).

[28] M. Levitus and S. Ranjit, "Cyanine dyes in biophysical research: the photophysics of polymethine fluorescent dyes in biomolecular environments.," Q. Rev. Biophys. **44**, 123 (2011).

[29] A. Mishra, R.K. Behera, P.K. Behera, B.K. Mishra, and G.B. Behera, "Cyanines during the 1990s: a review," Chem. Rev. **100**, 1973 (2000).

[30] F. Würthner, T.E. Kaiser, and C.R. Saha-Möller, "J-aggregates: From serendipitous discovery to supramolecular engineering of functional dye materials," Angew. Chemie - Int. Ed. **50**, 3376 (2011).

[31] U. Resch-Genger, M. Grabolle, S. Cavaliere-Jaricot, R. Nitschke, and T. Nann, "Quantum dots versus organic dyes as fluorescent labels," Nat. Methods **5**, 763 (2008).

[32] M.E. Sanborn, B.K. Connolly, K. Gurunathan, and M. Levitus, "Fluorescence properties and photophysics of the sulfoindocyanine Cy3 linked covalently to DNA," J. Phys. Chem. B **111**, 11064 (2007).

[33] W. Lee, D. Jose, C. Phelps, A.H. Marcus, and P.H. Von Hippel, "A single-molecule view of the assembly pathway, subunit stoichiometry, and unwinding activity of the bacteriophage T4 primosome (helicase-primase) complex," Biochemistry **52**, 3157 (2013).

[34] W. Lee, P.H. Von Hippel, and A.H. Marcus, "Internally labeled Cy3/Cy5 DNA constructs show greatly enhanced photo-stability in single-molecule FRET experiments," Nucleic Acids Res. **42**, 5967 (2014).

[35] C. Phelps, W. Lee, D. Jose, P.H. von Hippel, and A.H. Marcus, "Single-molecule FRET and linear dichroism studies of DNA breathing and helicase binding at replication fork junctions," Proc. Natl. Acad. Sci. **110**, 17320 (2013).

[36] P.H. von Hippel, N.P. Johnson, and A.H. Marcus, "Fifty years of DNA 'Breathing': Reflections on old and new approaches," Biopolymers **99**, 923 (2013).

[37] T. Holstein, "Studies of Polaron Motion: Part I. The Molecular-Crystal Model," Ann. Phys. (N. Y). **8**, 325 (1959).

[38] J. Roden, A. Eisfeld, M. Dvořák, M. Dvok, O. Bnermann, and F. Stienkemeier, "Vibronic line shapes of PTCDA oligomers in helium nanodroplets," J. Chem. Phys. **134**, 054907 (2011).

[39] C.R. Cantor and P.R. Schimmel, *Biophysical Chemistry Part II: Techniques for the Study of Biological Structure and Function* (Freeman, New York, 1980).

[40] N. Berova and K. Nakanishi, *Circular Dichroism: Principles and Applications* (John Wiley & Sons, New York, 2000).

[41] S. Mukamel, *Principles of Nonlinear Optical Spectroscopy* (Oxford University Press, Oxford, 1995).

[42] H. Dong and G.R. Fleming, "Inhomogeneous broadening induced long-lived integrated two-color coherence photon echo signal," J. Phys. Chem. B **118**, 8956 (2014).

[43] J. Spiriti, J.K. Binder, M. Levitus, and A. Van Der Vaart, "Cy3-DNA stacking interactions strongly depend on the identity of the terminal basepair," Biophys. J. **100**, 1049 (2011).

[44] P.F. Aramendía, R. Martín Negri, and E. San Román, "Temperature dependence of fluorescence and photoisomerization in symmetric carbocyanines. Influence of medium viscosity and molecular structure," J. Phys. Chem. **98**, 3165 (1994).

[45] D.H. Waldeck and G.R. Fleming, "Influence of viscosity and temperature on rotational reorientation. Anisotropic absorption studies of 3,3′-diethyloxadicarbocyanine iodide," J. Phys. Chem. **85**, 2614 (1981).

[46] H. van Amerongen, L. Valkunas, and R. van Grondelle, *Photosynthetic Excitons* (World Scientific, Singapore, 2000).

[47] S. Volker, *Relaxation Processes in Molecular Excited States* (Kluwer Academic Publishers, Dordrecht, 1989).

[48] H. Bässler and B. Schweitzer, "Site-Selective Fluorescence Spectroscopy of Conjugated Polymers and Oligomers," Acc. Chem. Res. **32**, 173 (1999).

[49] M. Aydin, Ö. Dede, and D.L. Akins, "Density functional theory and Raman spectroscopy applied to structure and vibrational mode analysis of 1,1',3,3'-tetraethyl-5,5',6,6'-tetrachloro- benzimidazolocarbocyanine iodide and its aggregate.," J. Chem. Phys. **134**, 064325 (2011).

[50] L.I. Markova, V.L. Malinovskii, L.D. Patsenker, and R. Häner, "J- vs. H-type assembly: pentamethine cyanine (Cy5) as a near-IR chiroptical reporter.," Chem. Commun. (Camb). **49**, 5298 (2013).

[51] F. Nicoli, M.K. Roos, E.A. Hemmig, M. Di Antonio, R. de Vivie-Riedle, and T. Liedl, "Proximity-Induced H-Aggregation of Cyanine Dyes on DNA-Duplexes," J. Phys. Chem. A **120**, 9941 (2016).

CHAPTER V

[1] P.H. von Hippel, N.P. Johnson, and A.H. Marcus, "Fifty years of DNA 'Breathing': Reflections on old and new approaches," Biopolymers **99**, 923 (2013).

[2] D. Jose, S.E. Weitzel, and P.H. von Hippel, "Breathing fluctuations in position-specific DNA base pairs are involved in regulating helicase movement into the replication fork," Proc. Natl. Acad. Sci. **109**, 14428 (2012).

[3] D. Jose, K. Datta, N.P. Johnson, and P.H. von Hippel, "Spectroscopic studies of position-specific DNA 'breathing' fluctuations at replication forks and primer-template junctions.," Proc. Natl. Acad. Sci. U. S. A. **106**, 4231 (2009).

[4] P.H. von Hippel and E. Delagoutte, "A general model for nucleic acid helicases and their 'coupling' within macromolecular machines," Cell **104**, 177 (2001).

[5] M. Levitus and S. Ranjit, "Cyanine dyes in biophysical research: the photophysics of polymethine fluorescent dyes in biomolecular environments.," Q. Rev. Biophys. **44**, 123 (2011).

[6] A. Mishra, R.K. Behera, P.K. Behera, B.K. Mishra, and G.B. Behera, "Cyanines during the 1990s: a review," Chem. Rev. **100**, 1973 (2000).

[7] S. Ranjit, K. Gurunathan, and M. Levitus, "Photophysics of backbone fluorescent DNA modifications: reducing uncertainties in FRET.," J. Phys. Chem. B **113**, 7861 (2009).

[8] W. Lee, D. Jose, C. Phelps, A.H. Marcus, and P.H. Von Hippel, "A single-molecule view of the assembly pathway, subunit stoichiometry, and unwinding activity of the

bacteriophage T4 primosome (helicase-primase) complex," Biochemistry **52**, 3157 (2013).

[9] W. Lee, P.H. Von Hippel, and A.H. Marcus, "Internally labeled Cy3/Cy5 DNA constructs show greatly enhanced photo-stability in single-molecule FRET experiments," Nucleic Acids Res. **42**, 5967 (2014).

[10] C. Phelps, W. Lee, D. Jose, P.H. von Hippel, and A.H. Marcus, "Single-molecule FRET and linear dichroism studies of DNA breathing and helicase binding at replication fork junctions," Proc. Natl. Acad. Sci. **110**, 17320 (2013).

[11] L. Kringle, N.P.D. Sawaya, J. Widom, C. Adams, M.G. Raymer, A. Aspuru-Guzik, and A.H. Marcus, "Temperature-dependent conformations of exciton-coupled Cy3 dimers in double-stranded DNA," J. Chem. Phys. **148**, 085101 (2018).

[12] B.L. Cannon, D.L. Kellis, L.K. Patten, P.H. Davis, J. Lee, E. Graugnard, B. Yurke, and W.B. Knowlton, "Coherent Exciton Delocalization in a Two-State DNA-Templated Dye Aggregate System," J. Phys. Chem. A **121**, 6905 (2017).

[13] B.L. Cannon, L.K. Patten, D.L. Kellis, P.H. Davis, J. Lee, E. Graugnard, B. Yurke, and W.B. Knowlton, "Large Davydov Splitting and Strong Fluorescence Suppression: An Investigation of Exciton Delocalization in DNA-Templated Holliday Junction Dye Aggregates," J. Phys. Chem. A **122**, 2086 (2018).

[14] E.M.S. Stennett, N. Ma, A. Van Der Vaart, and M. Levitus, "Photophysical and dynamical properties of doubly linked Cy3-DNA constructs," J. Phys. Chem. B **118**, 152 (2014).

[15] S. Mukamel, *Principles of Nonlinear Optical Spectroscopy* (Oxford University Press, Oxford, 1995).

[16] H. Dong and G.R. Fleming, "Inhomogeneous broadening induced long-lived integrated two-color coherence photon echo signal," J. Phys. Chem. B **118**, 8956 (2014).

[17] H. van Amerongen, L. Valkunas, and R. van Grondelle, *Photosynthetic Excitons* (World Scientific, Singapore, 2000).

[18] J.-L. Mergny and L. Lacroix, "Analysis of Thermal Melting Curves," Oligonucleotides **13**, 515 (2003).

[19] G.A. Lott, A. Perdomo-Ortiz, J.K. Utterback, J.R. Widom, A. Aspuru-Guzik, and A.H. Marcus, "Conformation of self-assembled porphyrin dimers in liposome vesicles by phase-modulation 2D fluorescence spectroscopy," Proc. Natl. Acad. Sci. **108**, 16521 (2011).

[20] A. Perdomo-Ortiz, J.R. Widom, G.A. Lott, A. Aspuru-Guzik, and A.H. Marcus, "Conformation and electronic population transfer in membrane-supported self-assembled

porphyrin dimers by 2D fluorescence spectroscopy," J. Phys. Chem. B **116**, 10757 (2012).

[21] J.R. Widom, W. Lee, A. Perdomo-Ortiz, D. Rappoport, T.F. Molinski, A. Aspuru-Guzik, and A.H. Marcus, "Temperature-dependent conformations of a membrane supported zinc porphyrin tweezer by 2D fluorescence spectroscopy," J. Phys. Chem. A **117**, 6171 (2013).

[22] J.R. Widom, N.P. Johnson, P.H. Von Hippel, and A.H. Marcus, "Solution conformation of 2-aminopurine dinucleotide determined by ultraviolet two-dimensional fluorescence spectroscopy," New J. Phys. **15**, 025028 (2013).

CHAPTER VI

[1] E. Collini, C.Y. Wong, K.E. Wilk, P.M.G. Curmi, P. Brumer, and G.D. Scholes, "Coherently wired light-harvesting in photosynthetic marine algae at ambient temperature.," Nature **463**, 644 (2010).

[2] A. Chenu and G.D. Scholes, "Coherence in Energy Transfer and Photosynthesis," Annu. Rev. Phys. Chem. **66**, 141210140020002 (2014).

[3] S.M. Blau, D.I.G. Bennett, C. Kreisbeck, G.D. Scholes, and A. Aspuru-Guzik, "Local protein solvation drives direct down-conversion in phycobiliprotein PC645 via incoherent vibronic transport," arXiv:1704.05449v1 (2017).

[4] G.S. Engel, T.R. Calhoun, E.L. Read, T.K. Ahn, T. Mančal, Y.C. Cheng, R.E. Blankenship, and G.R. Fleming, "Evidence for wavelike energy transfer through quantum coherence in photosynthetic systems," Nature **446**, 782 (2007).

[5] E. Romero, R. Augulis, V.I. Novoderezhkin, M. Ferretti, J. Thieme, D. Zigmantas, and R. van Grondelle, "Quantum coherence in photosynthesis for efficient solar-energy conversion," Nat. Phys. **10**, 676 (2014).

[6] F.D. Fuller, J. Pan, A. Gelzinis, V. Butkus, S.S. Senlik, D.E. Wilcox, C.F. Yocum, L. Valkunas, D. Abramavicius, and J.P. Ogilvie, "Vibronic coherence in oxygenic photosynthesis," Nat. Chem. **6**, 706 (2014).

[7] V. Tiwari, W.K. Peters, and D.M. Jonas, "Electronic resonance with anticorrelated pigment vibrations drives photosynthetic energy transfer outside the adiabatic framework.," Proc. Natl. Acad. Sci. U. S. A. **110**, 1203 (2013).

[8] A. Halpin, P.J.M. Johnson, R. Tempelaar, R.S. Murphy, J. Knoester, T.L.C. Jansen, and R.J.D. Miller, "Two-dimensional spectroscopy of a molecular dimer unveils the effects of vibronic coupling on exciton coherences.," Nat. Chem. **6**, 196 (2014).

[9] H.-G. Duan, P. Nalbach, V.I. Prokhorenko, S. Mukamel, and M. Thorwart, "On the origin of oscillations in two-dimensional spectra of excitonically-coupled molecular systems," New J. Phys. **17**, 72002 (2015).

[10] J. Lim, D. Paleček, F. Caycedo-Soler, C.N. Lincoln, J. Prior, H. von Berlepsch, S.F. Huelga, M.B. Plenio, D. Zigmantas, and J. Hauer, "Vibronic origin of long-lived coherence in an artificial molecular light harvester," Nat. Commun. **6**, 7755 (2015).

[11] F. Milota, V.I. Prokhorenko, T. Mancal, H. Berlepsch, H.F. Kauffmann, and J. Hauer, "Vibronic and Vibrational Coherences in Two- Dimensional Electronic Spectra of Supramolecular J-A ggregates," J. Phys. Chem. A 6007 (2013).

[12] L. Kringle, N.P.D. Sawaya, J. Widom, C. Adams, M.G. Raymer, A. Aspuru-Guzik, and A.H. Marcus, "Temperature-dependent conformations of exciton-coupled Cy3 dimers in double-stranded DNA," J. Chem. Phys. **148**, (2018).

[13] M. Aydin, Ö. Dede, and D.L. Akins, "Density functional theory and Raman spectroscopy applied to structure and vibrational mode analysis of 1,1',3,3'-tetraethyl-5,5',6,6'-tetrachloro- benzimidazolocarbocyanine iodide and its aggregate.," J. Chem. Phys. **134**, 64325 (2011).

[14] C.C. Rich and J.L. McHale, "Resonance Raman spectra of individual excitonically coupled chromophore aggregates," J. Phys. Chem. C **117**, 10856 (2013).

[15] D.B. Turner, R. Dinshaw, K.-K. Lee, M.S. Belsley, K.E. Wilk, P.M.G. Curmi, and G.D. Scholes, "Quantitative investigations of quantum coherence for a light-harvesting protein at conditions simulating photosynthesis," Phys. Chem. Chem. Phys. **14**, 4857 (2012).

[16] G. Panitchayangkoon, D. V. Voronine, D. Abramavicius, J.R. Caram, N.H.C. Lewis, S. Mukamel, and G.S. Engel, "Direct evidence of quantum transport in photosynthetic light-harvesting complexes," Proc. Natl. Acad. Sci. **108**, 20908 (2011).

[17] P.H. von Hippel, N.P. Johnson, and A.H. Marcus, "Fifty years of DNA 'Breathing': Reflections on old and new approaches," Biopolymers **99**, 923 (2013).

CHAPTER VII

[1] M. Aydin, Ö. Dede, and D.L. Akins, "Density functional theory and Raman spectroscopy applied to structure and vibrational mode analysis of 1,1',3,3'-tetraethyl-5,5',6,6'-tetrachloro- benzimidazolocarbocyanine iodide and its aggregate.," J. Chem. Phys. **134**, 64325 (2011).

[2] J. Roden, A. Eisfeld, M. Dvořák, M. Dvok, O. Bnermann, and F. Stienkemeier, "Vibronic line shapes of PTCDA oligomers in helium nanodroplets," J. Chem. Phys. **134**, 54907 (2011).

[3] L. Valkunas, D. Abramavicius, and T. Mancal, *Molecular Excitation Dynamics and Relaxation* (Wiley-VHC, Weinheim, 2013).

[4] K.A. Kistler, F.C. Spano, and S. Matsika, "A benchmark of excitonic couplings derived from atomic transition charges," J. Phys. Chem. B **117**, 2032 (2013).

[5] D. Jose, K. Datta, N.P. Johnson, and P.H. von Hippel, "Spectroscopic studies of position-specific DNA 'breathing' fluctuations at replication forks and primer-template junctions.," Proc. Natl. Acad. Sci. U. S. A. **106**, 4231 (2009).

[6] D. Jose, S.E. Weitzel, and P.H. von Hippel, "Breathing fluctuations in position-specific DNA base pairs are involved in regulating helicase movement into the replication fork," Proc. Natl. Acad. Sci. **109**, 14428 (2012).

[7] E.M.S. Stennett, N. Ma, A. Van Der Vaart, and M. Levitus, "Photophysical and dynamical properties of doubly linked Cy3-DNA constructs," J. Phys. Chem. B **118**, 152 (2014).

[8] A. Halpin, P.J.M. Johnson, R. Tempelaar, R.S. Murphy, J. Knoester, T.L.C. Jansen, and R.J.D. Miller, "Two-dimensional spectroscopy of a molecular dimer unveils the effects of vibronic coupling on exciton coherences.," Nat. Chem. **6**, 196 (2014).

[9] H.-G. Duan, P. Nalbach, V.I. Prokhorenko, S. Mukamel, and M. Thorwart, "On the origin of oscillations in two-dimensional spectra of excitonically-coupled molecular systems," New J. Phys. **17**, 72002 (2015).

[10] J. Lim, D. Paleček, F. Caycedo-Soler, C.N. Lincoln, J. Prior, H. von Berlepsch, S.F. Huelga, M.B. Plenio, D. Zigmantas, and J. Hauer, "Vibronic origin of long-lived coherence in an artificial molecular light harvester," Nat. Commun. **6**, 7755 (2015).

[11] C.C. Rich and J.L. McHale, "Resonance Raman spectra of individual excitonically coupled chromophore aggregates," J. Phys. Chem. C **117**, 10856 (2013).

APPENDIX B

[1] A. Perdomo-Ortiz, J.R. Widom, G.A. Lott, A. Aspuru-Guzik, and A.H. Marcus, "Conformation and electronic population transfer in membrane-supported self-assembled porphyrin dimers by 2D fluorescence spectroscopy," J. Phys. Chem. B **116**, 10757 (2012).